Kobe University Repository : Kernel

PDF issue: 2026-11-25

Structure and Mechanical Properties of Bio-based Polymers and Their Composites

何, 晨玥

(Degree)
博士（工学）

(Date of Degree)
2025-03-25

(Date of Publication)
2026-03-01

(Resource Type)
doctoral thesis

(Report Number)
甲第9210号

(URL)
https://hdl.handle.net/20.500.14094/0100496491

※ 当コンテンツは神戸大学の学術成果です。無断複製・不正使用等を禁じます。著作権法で認められている範囲内で、適切にご利用ください。

Doctoral Dissertation

博士論文

Structure and Mechanical Properties of Bio-based Polymers and Their Composites

（バイオベースポリマーとその複合材料の構造と力学物性）

January, 2025

令和 7 年 1 月

Graduate School of Engineering, Kobe University

神戸大学大学院　工学研究科

He Chenyue

何　晨玥

Doctoral Dissertation

博士論文

Structure and Mechanical Properties of Bio-based Polymers and Their Composites

（バイオベースポリマーとその複合材料の構造と力学物性）

January, 2025

令和 7 年 1 月

Graduate School of Engineering, Kobe University

神戸大学大学院　工学研究科

He Chenyue

何　晨玥

Table of Contents

page

General Introduction 1

Chapter I Microstructure and Crystal Modulus of Polyamide 4 α-form in the Direction Parallel to the Chain Axis

1.1. Introduction 23
1.2. Experimental 25
1.3. Results and discussion 34
1.4. Conclusions 49
1.5. References 50

Chapter II Stress Transfer Analysis of Poly(*L*-lactic acid) / Hydroxyapatite Composites by Synchrotron Radiation

2.1. Introduction 59
2.2. Experimental 62
2.3. Results and discussion 68
2.4. Conclusions 84
2.5. References 85

Chapter Ⅲ Preparation of Isotactic Polypropylene/Coffee Silverskin Composites

3.1. Introduction 94
3.2. Experimental 97
3.3. Results and discussion 103
3.4. Conclusions 124

3.5. References 125

Conclusions 135

List of Achievements

Publications 140
Presentations 141

Acknowledgement 144

GENERAL

INTRODUCTION

Since Staudinger introduced the concept of "macromolecules" in 1920, polymers with diverse properties have been investigated and widely used across various fields, including food packaging, automotive, electronics, and aerospace industries.[1–6] Petroleum-based polymers have been widely utilized for years owing to their lightweight, inexpensiveness, processibility, and tunable properties.[7–9] They can be customized for varying applications, making them suitable for packaging, construction, healthcare, electronics, and aerospace. However, the extensive use of petroleum-based polymers has led to severe environmental problems and significant consumption of petroleum resources. Bio-based polymers have emerged as promising alternatives to conventional petroleum-based polymers to address these issues.[9–13] These materials are designed to meet diverse application requirements through extrusion, injection, molding, blow molding, calendering, dry spinning, and additive manufacturing (3D printing). Fabrication of the composite by combining bio-based polymer with organic or inorganic materials is also a practical approach to meet the growing demand. The further development of bio-based polymers requires a more sophisticated understanding of them and their composites.

As a new bio-based polymer, polyamide 4 (PA4) has recently received significant attention for its unique properties. Owing to the high concentration of amide groups in its structure and a dense intermolecular hydrogen bonding network, PA4 demonstrates high mechanical and thermal properties, excellent moisture absorption, and strong barrier properties. Figure 1 shows the schematic of the fabrication of bio-based PA4. Firstly, bio-based γ-glutamic acid was obtained through fermentation of *L*-glutamic acid using the microorganism *Escherichia coli*. The cyclization reaction of γ-glutamic acid leads to the 2-pyrrolidone, the cyclic monomer of PA4, and this bio-based polymer is synthesized

through ring-opening polymerization.[14] Besides, PA4 is known to be degradable in natural environments, such as seawater and soil, making it a sustainable bio-based biodegradable polymer.[15–17] Although PA4 is not yet commercially available, its sustainability and outstanding features suggest it will likely be widely produced and utilized shortly. However, the decomposition temperature of PA4 is close to its melting temperature, and the PA4 is decomposed under thermal processing, making the thermal processing of this polymer a challenge. Several efforts have been devoted to investigating the processing and the properties of PA4. Lenka *et al.* prepared PA4 nanofiber using electrospinning and investigated the effects of the molecular weight and the kind of solvent on the properties and morphology of the nanofibers. [18] Yamane *et al.* demonstrated that the melt-spinning of PA4 could be achieved by blending it with the ionic liquid 1-butyl-3-methylimidazolium chloride, which reduced PA4's melting point by 40°C, reducing the temperature of the thermal processing.[19] Wang *et al.* blend PA4 with PA6 to investigate the effect of PA6 contents on the crystallization behaviors and thermal properties of PA4.[20] For the further application of PA4, a more comprehensive understanding of this polymer's mechanical properties is required.

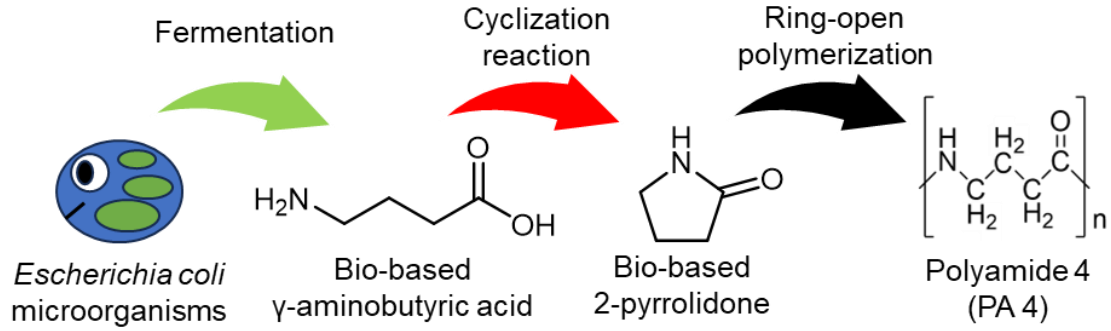

Fig.1 Schematic of the fabrication of PA4.

The elastic modulus of the crystalline regions (crystal modulus) is one of the significant mechanical properties of polymers. The crystal modulus (E_l) in the direction parallel to

the chain axis provides information about the polymer's chain conformation in the crystal lattice and the maximum attainable Young's modulus of polymers. In previous works of the Nishino laboratory, it has been reported that polyethylene and poly(vinyl alcohol) with fully extended zig-zag conformation show high E_l values (235 GPa and 250 GPa), indicating the molecular deformation in these polymers. Molecular deformation generally involves three mechanisms: bond stretching, bond angle bending, and internal rotation around a single bond, with force contribution ratios of 100:10:1, respectively. For planar zigzag skeletons, bond stretching and bond angle bending primarily drive chain extension, explaining the high E_l values observed in PE and PVA. The E_l values can be measured

from the meridional reflection of highly oriented samples with X-ray diffraction.

For polyamides, there were curious phenomena that the different meridional reflections provided different E_l values. In the case of polyamide 66 (PA66), the E_l values for 015 and 1314 reflections were 60 GPa and 172 GPa.[21] For polyamide 9-T (PA9-T), the meridional reflections at 28.3°, 42.7°, and 78.2°(CuKα) provided E_l values of 24, 30 and 40 GPa, respectively.[22] In polyamide 6 (PA6) α-form, the values of E_l for 004 and 0014 reflections were 53 GPa and 183 GPa at 300K.[23] According to the research of Kaji *et al.*, the apparent difference in PA6's E_l values was attributed to the change in the crystallite size induced by applied stress. This conclusion was confirmed by the calculations of the

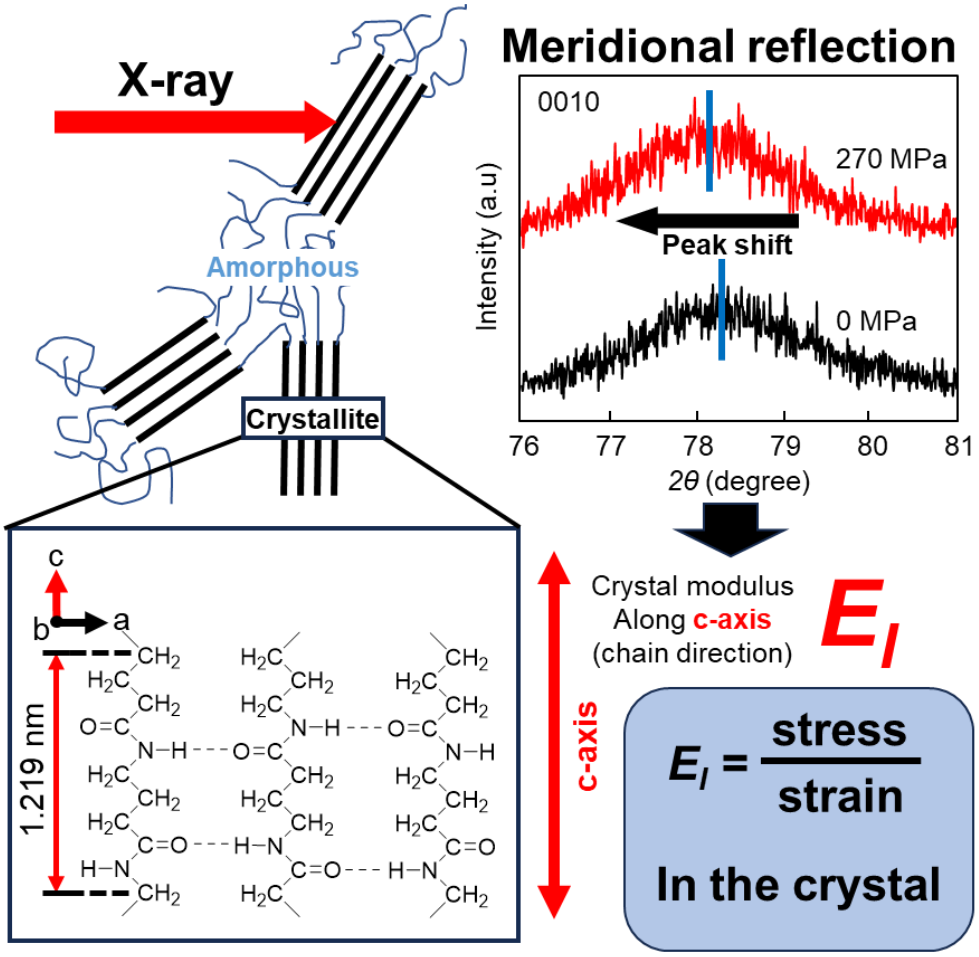

Fig.2 Measurement of crystal modulus in chain direction E_l of PA4 α-form with X-ray diffraction.

structure factor, Laue factor, and the measurement of Hosemann's method.[23–25]

In this thesis, the highly oriented PA4 fibers were prepared by dry spinning followed by thermal drawing. The E_l values of the PA4 α-form were measured from the 004 and 0010 meridional reflections under the applied stress using X-ray diffraction, as shown in Figure 2. The relation of crystal modulus with its microstructure and mechanical properties was also discussed.

Among varying bio-based polymers, poly-*L*-lactic acid (PLLA) has been the most extensively studied bio-based polymer with biodegradability, attracting significant interest in healthcare, food packaging, and agriculture over the past decades. However, challenges remain, such as PLLA's relatively low mechanical strength, which limits its broader application, particularly in high-performance bone scaffold development. To overcome this limitation, researchers have investigated incorporating organic and inorganic fillers such as cellulose nanocrystals, magnesium hydroxide, graphene, and graphene oxide into PLLA matrices to enhance mechanical performance and meet specific needs.

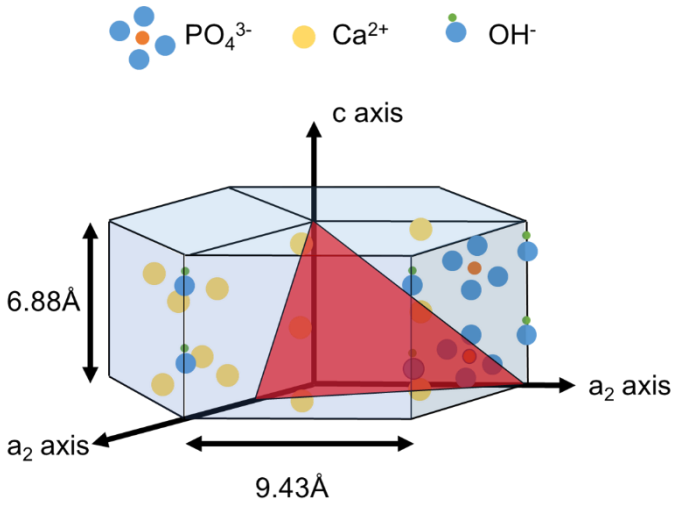

Fig.3 Hexagonal crystal structure of HAp.

Hydroxyapatite (HAp), with the chemical formula $Ca_{10}(PO_4)_6(OH)_2$ and a hexagonal crystal structure, is a bioactive and non-toxic ceramic with a hexagonal crystal structure, closely resembling the inorganic part of the bone with exceptional mechanical properties. The crystal structure of HAp is shown in Figure 3, which was proposed by M. I. Kay *et al.* in 1964.[26] Its bioactive and osteoconductive nature enables it to form chemical bonds with living tissues, making HAp highly applicable in medical fields, particularly in dentistry and orthopedic surgery. To maximize each benefit of the material, PLLA/HAp composite biomaterials were developed and employed for reconstructing and repairing bone defects. Various advanced methods, including electrospinning and additive manufacturing, have been utilized to prepare PLLA/HAp composites.[13,27–33] In PLLA/HAp composites, the intrinsic properties of the filler and matrix, along with interaction at the filler/matrix interface, significantly affect the mechanical performance of the whole composite. Thus, a thorough understanding of interfacial stress transfer in PLLA/HAp composites is crucial for their further applications.

X-ray diffraction has been used to investigate the interfacial stress transfer mechanism in various composite systems, such as epoxy/silica [34], epoxy/carbon-fiber [35], PLLA/kenaf [36], Poly(vinyl alcohol)/montmorillonite [37] and cellulose-nanofiber/montmorillonite. [38] The stress transferred to the filler along the stretching direction was quantitatively evaluated from the shift of the X-ray diffraction peak when the whole composite was under applied stress, as shown in Figure 4.

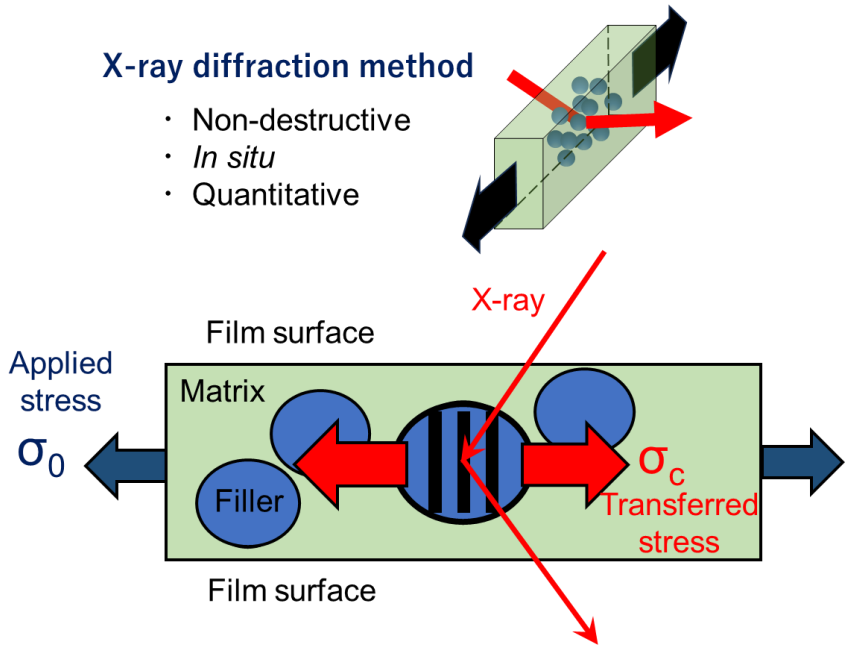

Fig.4 Schematic of stress transfer measurement by X-ray diffraction.

Synchrotron radiation with high brilliance makes it possible to obtain clear diffraction pattern of the crystalline fillers in the composites with low filler loading (<5wt %). Recent advancements in synchrotron X-ray diffraction and high-resolution X-ray detectors have enhanced the ability to assess lattice strain within composites at the microscale, achieving unprecedented resolution. [39–41]

In this thesis, stress transfer phenomena in PLLA/HAp composites filled with nano-sized HAp or micro-sized HAp under tensile deformation were investigated by *in situ* synchrotron wide-angle X-ray diffraction (WAXD). The stress transfer analyses used the diffraction peak of the (211) plane of HAp. The mechanical reinforcement effects of HAp fillers in composites on HAp particle sizes and fraction ratios were evaluated by stress transfer analyses. The interfacial states of the composites under the tensile deformation were assessed by comparing stress σ_c transferred to the HAp fillers with the stress σ_0 applied to the whole composites.

Cellulose is the most abundant bio-based polymer on earth and the fundamental structural component of plant cell walls. As a natural polymer composed of glucose units connected by β-1,4-glycosidic bonds, cellulose imparts rigidity and strength to plants, establishing its significance as a key material in the field of renewable resources. Most cellulose exists in nature as lignocellulose, which is composed of microfibrils embedded within plant cell walls. These lignocellulose are composed of cellulose encased by the less crystalline bio-based polymers hemicellulose and lignin. As a lignocellulosic biomass, coffee silverskin (CS) is the only byproduct of the coffee roasting process. It is typically considered a waste in the coffee industry, consisting of 70wt% bio-based polymer (24 wt% cellulose, 17 wt% hemicellulose, and 29 wt% lignin).

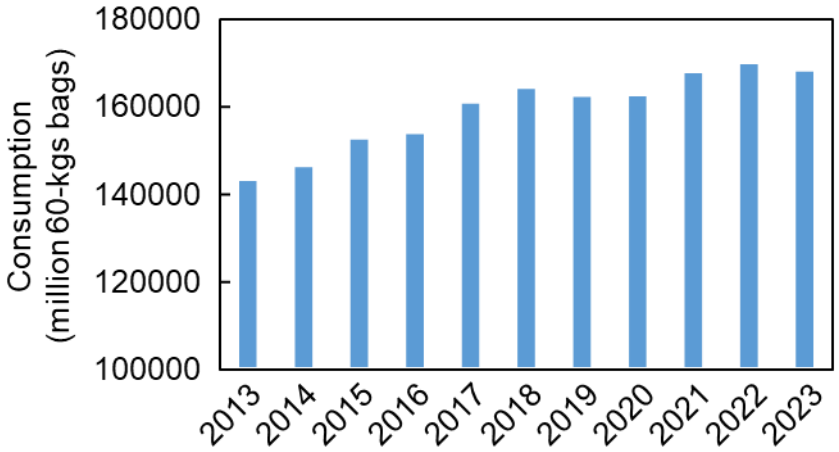

Fig.5 The worldwide dimestic consumption of coffee beans in last decade.

Coffee is one of the most popular and widely consumed beverages worldwide. Figure 5 shows the worldwide domestic consumption of coffee beans in the last decade according to research of the United States Department of Agriculture (USDA). The global consumption of coffee beans reached approximately 10 million tons of green coffee beans in 2023. The drinkable coffee is obtained from the raw coffee cherry through sorting, cleaning, pulping, fermentation, washing, drying, and roasting process. The roasting process produces roasted coffee beans and the only by-product known as coffee silverskin (CS), constituting approximately 0.75wt% of a coffee cherry or 4.2wt% of a green coffee bean. After the roasting process of coffee, CS is always discarded and treated as waste which has potential for engineering applications. Its low moisture and oil content and non-perishable characteristics differentiate it from other by-products of the coffee industry, such as coffee pulp or spent coffee grounds, making it a ready-to-use material. As a lignocellulosic biomass, CS could be exploited as a filler for composite production.

Considerable efforts have been devoted to the fabrication of CS composites. Ghazvini *et al.* investigated the effect of CS loading on the properties of CS/poly (*L*-lactic

acid)/poly(butylene succinate) three-phase composites. They reported that Young's modulus and hydrophilicity were increased significantly with the addition of CS fillers.[42] Sarashi et al. used CS to reinforce poly(butylene adipate-co-terephthalate)/poly(3-hydroxybutyrate-co-3-hydroxyvalerate) blend with twin-screw extrusion and injection molding, improving stiffness and tensile strength.[43] *Hejna et al.* fabricated the CS/high-density polyethylene composites with twin-screw extrusion and hot-pressing. The thermo-oxidative resistance of the composites was enhanced notably with the corporation of CS.[44] Zarrinbakhsh *et al*. prepared the CS/isotactic polypropylene (PP) composites filled with 25wt% CS. An increase in the tensile and flexural modulus, as well as that in the impact-absorbed energy, were observed.[45] Besides, these studies consistently reported that CS enhanced the crystallization of polymer matrices by acting as a nuclear agent. However, for all these composites, the maximum filling ratio of CS was 30wt% to achieve balanced mechanical properties. Their works highlighted the necessity for modifying CS and the addition of the compatibilizer to improve the interfacial adhesion between the CS and polymer matrix, enabling the CS to function as an efficient filler.

As a natural filler, CS is primarily cellulose and hemicellulose, which exhibits extremely high hydrophilicity. This characteristic leads to inferior adhesion with the hydrophobic polymer. Additionally, the hydrophilic nature of these fillers also leads to inadequate particle dispersion, resulting in a decrease in mechanical properties. Several approaches have been employed to enhance adhesion between the natural filler and polymer matrix, including the surface modification of the fillers, hydrophilization of the matrix, and the use of compatibilizers. In all kinds of compatibilizers, amphiphilic maleic anhydride-modified polypropylene (m-PP) with the hydrophilic maleic anhydride

group grafted on the hydrophobic PP backbone is the most commercially significant functionalized polymer. With the addition of m-PP, the affinity between the CS and hydrophobic polymer matrix is expected to be improved, leading to the increase of mechanical properties.

In this thesis, the application of CS as a bio-based filler was investigated, and isotactic polypropylene was chosen as a matrix. The PP/CS and m-PP/CS composites were prepared through melt-kneading and hot-pressing. The aim was to investigate the effects of m-PP and the CS filling ratios on the mechanical and thermal properties of PP/CS composites and the morphology of composites was also discussed.

Concerning these contents, this thesis was divided into three chapters and explained in detail as follows:

Chapter I is concerned with the crystal modulus E_l in the direction parallel to the chain direction of PA4 α-form measured by X-ray diffraction. The highly oriented α-form PA4 fibers were fabricated by dry spinning and thermal drawing. E_l was evaluated from the X-ray diffraction peak shift owing to the tensile stress. The phenomenon that diffrent meridianal reflections provided different E_l values was discussed from the perspective of microstructure of PA4.

Chapter II is concerned with the stress transfer analyses of the PLLA/HAp composites under tensile tests using *in situ* synchrotron X-ray diffraction. The dependence of the stress transfers on the fraction ratios of HAp fillers and the filler sizes was discussed. Furthermore, the correlation between macroscopic mechanical properties and stress transfer behaviors of the composites during tensile deformation and fracture was revealed through *in situ* X-ray diffraction measurement with synchrotron radiation.

Chapter III is concerned with the fabrication of PP/CS composites. The PP/CS composites were prepared through melt-blending and hot-press. The effect of the addition of m-PP on the properties of the composites was also investigated. Moreover, the correlation between the structure and mechanical properties of CS/PP composites was clarified.

References

[1] H. Staudinger, Über Polymerisation, Berichte Der Deutschen Chemischen Gesellschaft (A and B Series) 53 (1920) 1073–1085. https://doi.org/10.1002/cber.19200530627.

[2] R. Hsissou, R. Seghiri, Z. Benzekri, M. Hilali, M. Rafik, A. Elharfi, Polymer composite materials: A comprehensive review, Compos Struct 262 (2021) 113640. https://doi.org/10.1016/j.compstruct.2021.113640.

[3] S. Cichosz, A. Masek, M. Zaborski, Polymer-based sensors: A review, Polym Test 67 (2018) 342–348. https://doi.org/10.1016/j.polymertesting.2018.03.024.

[4] T. Ma, Y. Zhang, K. Ruan, H. Guo, M. He, X. Shi, Y. Guo, J. Kong, J. Gu, Advances in 3D printing for polymer composites: A review, InfoMat 6 (2024). https://doi.org/10.1002/inf2.12568.

[5] R. Hsissou, R. Seghiri, Z. Benzekri, M. Hilali, M. Rafik, A. Elharfi, Polymer composite materials: A comprehensive review, Compos Struct 262 (2021) 113640. https://doi.org/10.1016/j.compstruct.2021.113640.

[6] K.S. Ngai, S. Ramesh, K. Ramesh, J.C. Juan, A review of polymer electrolytes: fundamental, approaches and applications, Ionics (Kiel) 22 (2016) 1259–1279. https://doi.org/10.1007/s11581-016-1756-4.

[7] C. Sánchez, Fungal potential for the degradation of petroleum-based polymers: An overview of macro- and microplastics biodegradation, Biotechnol Adv 40 (2020) 107501. https://doi.org/10.1016/j.biotechadv.2019.107501.

[8] A.Z. Naser, I. Deiab, B.M. Darras, Poly(lactic acid) (PLA) and

polyhydroxyalkanoates (PHAs), green alternatives to petroleum-based plastics: a review, RSC Adv 11 (2021) 17151–17196. https://doi.org/10.1039/D1RA02390J.

[9] G. Atiwesh, A. Mikhael, C.C. Parrish, J. Banoub, T.-A.T. Le, Environmental impact of bioplastic use: A review, Heliyon 7 (2021) e07918. https://doi.org/10.1016/j.heliyon.2021.e07918.

[10] E. Sina, ed., Handbook of Biopolymers and Biodegradable Plastics, Elsevier, 2013. https://doi.org/10.1016/C2011-0-07342-8.

[11] P. Bordes, E. Pollet, L. Averous, Nano-biocomposites: Biodegradable polyester/nanoclay systems, Prog Polym Sci 34 (2009) 125–155. https://doi.org/10.1016/j.progpolymsci.2008.10.002.

[12] D. Garcia-Garcia, A. Carbonell-Verdu, A. Jordá-Vilaplana, R. Balart, D. Garcia-Sanoguera, Development and characterization of green composites from bio-based polyethylene and peanut shell, J Appl Polym Sci 133 (2016). https://doi.org/10.1002/app.43940.

[13] E. Capuana, F. Lopresti, M. Ceraulo, V. La Carrubba, Poly-l-Lactic Acid (PLLA)-Based Biomaterials for Regenerative Medicine: A Review on Processing and Applications, Polymers (Basel) 14 (2022) 1153. https://doi.org/10.3390/polym14061153.

[14] N. Yamano, N. Kawasaki, S. Takeda, A. Nakayama, Production of 2-Pyrrolidone from Biobased Glutamate by Using Escherichia coli, J Polym Environ 21 (2013) 528–533. https://doi.org/10.1007/s10924-012-0466-x.

[15] K. Hashimoto, T. Hamano, M. Okada, Degradation of several polyamides in soils,

J Appl Polym Sci 54 (1994) 1579–1583. https://doi.org/10.1002/app.1994.070541023.

[16] N. Yamano, A. Nakayama, N. Kawasaki, N. Yamamoto, S. Aiba, Mechanism and Characterization of Polyamide 4 Degradation by Pseudomonas sp., J Polym Environ 16 (2008) 141–146. https://doi.org/10.1007/s10924-008-0090-y.

[17] K. Tachibana, K. Hashimoto, M. Yoshikawa, H. Okawa, Isolation and characterization of microorganisms degrading nylon 4 in the composted soil, Polym Degrad Stab 95 (2010) 912–917. https://doi.org/10.1016/j.polymdegradstab.2010.03.031.

[18] L. Blažková, L. Malinová, V. Benešová, J. Roda, J. Brožek, Nanofibers prepared by electrospinning from solutions of biobased polyamide 4, J Polym Sci A Polym Chem 55 (2017) 2203–2210. https://doi.org/10.1002/pola.28605.

[19] T. Nagahama, S. Yagi, H. Yamane, H. Xu, Melt spinning of polyamide 4, Polym Adv Technol 33 (2022) 3658–3665. https://doi.org/10.1002/pat.5818.

[20] M. Wang, Y. Zhang, F. Zhan, Y. Qiu, T. Chen, L. Zhao, Crystallization behaviour of polyamide 4 and its effect on melting point, Polymer (Guildf) 291 (2024) 126613. https://doi.org/10.1016/j.polymer.2023.126613.

[21] I. Sakurada, K. Kaji, relation between the polymer conformation and the elastic modulus of the crystalline region of polymer, Journal of Polymer Science Part C: Polymer Symposia 31 (1970) 57–76. https://doi.org/10.1002/polc.5070310108.

[22] A.J. Uddin, Y. Gotoh, Y. Ohkoshi, T. Nishino, R. Endo, Crystal modulus of a new semiaromatic polyamide 9-T, Polym Eng Sci 52 (2012) 331–337.

https://doi.org/10.1002/pen.22086.

[23] K. Kaji, I. Sakurada, Determination of the elastic modulus of polyamide crystals along the chain axis by x-ray diffraction, 1. The α-form of nylon-6, Die Makromolekulare Chemie 179 (1978) 209–217. https://doi.org/10.1002/macp.1978.021790121.

[24] K. Kaji, I. Sakurada, Crystallite size determination of nylon 6 by wallner's method, Journal of Polymer Science: Polymer Physics Edition 12 (1974) 1491–1497. https://doi.org/10.1002/pol.1974.180120721.

[25] K. Kaji, Increase of the Crystallite Size by Application of Tensile Stress for Highly Oriented Polymer, Die Makromolekulare Chemie 175 (1974) 311–325. https://doi.org/10.1002/macp.1974.021750131.

[26] M.I. KAY, R.A. YOUNG, A.S. POSNER, Crystal Structure of Hydroxyapatite, Nature 204 (1964) 1050–1052. https://doi.org/10.1038/2041050a0.

[27] M.L. Zhao, G. Sui, X.L. Deng, J.G. Lu, S.K. Ryu, X.P. Yang, PLLA/HA Electrospin Hybrid Nanofiber Scaffolds: Morphology, In Vitro Degradation and Cell Culture Potential, Adv Mat Res 11–12 (2006) 243–246. https://doi.org/10.4028/www.scientific.net/AMR.11-12.243.

[28] B. Kryszak, M. Biernat, P. Tymowicz-Grzyb, A. Junka, M. Brożyna, M. Worek, P. Dzienny, A. Antończak, K. Szustakiewicz, The effect of extrusion and injection molding on physical, chemical, and biological properties of PLLA/HAp whiskers composites, Polymer (Guildf) 287 (2023) 126428. https://doi.org/10.1016/j.polymer.2023.126428.

[29] S. Gay, S. Arostegui, J. Lemaitre, Preparation and characterization of dense nanohydroxyapatite/PLLA composites, Mater Sci Eng C 29 (2009) 172–177. https://doi.org/10.1016/j.msec.2008.06.005.

[30] L.F. Charles, E.R. Kramer, M.T. Shaw, J.R. Olson, M. Wei, Self-reinforced composites of hydroxyapatite-coated PLLA fibers: Fabrication and mechanical characterization, J Mech Behav Biomed Mater 17 (2013) 269–277. https://doi.org/10.1016/j.jmbbm.2012.09.007.

[31] B.D. Stepak, A.J. Antończak, K. Szustakiewicz, Optimization of femtosecond laser micromachining of polylactide and PLLA/HAp composite, in: U. Klotzbach, K. Washio, R. Kling (Eds.), Laser-Based Micro- and Nanoprocessing XII, SPIE, 2018: p. 70. https://doi.org/10.1117/12.2296433.

[32] M.A. Khan, Z. Hussain, U. Liaqat, M.A. Liaqat, M. Zahoor, Preparation of PBS/PLLA/HAP Composites by the Solution Casting Method: Mechanical Properties and Biocompatibility, Nanomaterials 10 (2020) 1778. https://doi.org/10.3390/nano10091778.

[33] W. Peng, W. Zheng, K. Shi, W. Wang, Y. Shao, D. Zhang, An *in vivo* evaluation of PLLA/PLLA-gHA nano-composite for internal fixation of mandibular bone fractures, Biomed. Mater. 10 (2015) 065007. https://doi.org/10.1088/1748-6041/10/6/065007.

[34] A.-R. Xu, T. Nishino, K. Nakamae, Stress transmission in silica particulate epoxy composite by X-ray diffraction, Polymer (Guildf) 33 (1992) 5167–5172. https://doi.org/10.1016/0032-3861(92)90796-Y.

[35] T. Nishino, H. Naito, K. Nakamura, K. Nakamae, X-ray diffraction studies on the stress transfer of transversely loaded carbon fibre reinforced composite, Compos Part A Appl Sci Manuf 31 (2000) 1225–1230. https://doi.org/10.1016/S1359-835X(00)00084-1.

[36] T. Nishino, K. Hirao, M. Kotera, X-ray diffraction studies on stress transfer of kenaf reinforced poly(l-lactic acid) composite, Compos Part A Appl Sci Manuf 37 (2006) 2269–2273. https://doi.org/10.1016/j.compositesa.2006.01.026.

[37] S. Morimune, M. Kotera, T. Nishino, Stress Transfer of Poly (VinylAlcohol) / Montmorillonite Nano composite Using X-ray Diffraction, Journal of The Adhesion Society of Japan 46 (2010) 320–324. https://doi.org/10.11618/adhesion.46.320.

[38] T. Matsumoto, S. Mori, T. Ohashi, C. He, T. Nishino, Stress-transfer analyses in cellulose nanofiber/montmorillonite nanocomposites with X-ray diffraction and chemical interaction between cellulose nanofiber and montmorillonite, Cellulose 29 (2022) 2949–2960. https://doi.org/10.1007/s10570-022-04423-x.

[39] T. Hatsui, H. Graafsma, X-ray imaging detectors for synchrotron and XFEL sources, IUCrJ 2 (2015) 371–383. https://doi.org/10.1107/S205225251500010X.

[40] R. Hashimoto, N. Igarashi, R. Kumai, H. Takagi, S. Kishimoto, T. Kudo, T. Hatsui, Application of the SOPHIAS Detector to Synchrotron Radiation X-Ray Experiments, in: 2018: pp. 263–266. https://doi.org/10.1007/978-981-13-1316-5_49.

[41] T. Hatsui, Developments of X-ray Imaging Detectors at SACLA/SPring-8: Current

Status and Future Outlook, Synchrotron Radiat News 27 (2014) 20–23. https://doi.org/10.1080/08940886.2014.930805.

[42] A.K.A. Ghazvini, G. Ormondroyd, S. Curling, A. Saccani, L. Sisti, An investigation on the possible use of coffee silverskin in <scp>PLA</scp> / <scp>PBS</scp> composites, J Appl Polym Sci 139 (2022). https://doi.org/10.1002/app.52264.

[43] F. Sarasini, J. Tirillò, A. Zuorro, G. Maffei, R. Lavecchia, D. Puglia, F. Dominici, F. Luzi, T. Valente, L. Torre, Recycling coffee silverskin in sustainable composites based on a poly(butylene adipate-co-terephthalate)/poly(3-hydroxybutyrate-co-3-hydroxyvalerate) matrix, Ind Crops Prod 118 (2018) 311–320. https://doi.org/10.1016/j.indcrop.2018.03.070.

[44] A. Hejna, M. Barczewski, P. Kosmela, O. Mysiukiewicz, A. Kuzmin, Coffee Silverskin as a Multifunctional Waste Filler for High-Density Polyethylene Green Composites, Journal of Composites Science 5 (2021) 44. https://doi.org/10.3390/jcs5020044.

[45] N. Zarrinbakhsh, T. Wang, A. Rodriguez-Uribe, M. Misra, A.K. Mohanty, Characterization of Wastes and Coproducts from the Coffee Industry for Composite Material Production, Bioresources 11 (2016). https://doi.org/10.15376/biores.11.3.7637-7653.

CHAPTER I

Microstructure and Crystal Modulus of Polyamide 4 α-form in the Direction Parallel to the Chain Axis

1.1 Introduction

As a new bio-based polymer, polyamide 4 (PA4) has also received a great attention recently for its promising mechanical and thermal properties based on its high melting point of 268°C. PA4 is fabricated by the ring-opening polymerization of 2-pyrrolidone, which is prepared by fermentation of biobased γ-glutamic acid. PA4 can be degraded under natural environments such as marine environments, activated sludge, and composted soil in a relatively short term.[1–4]

The elastic modulus of the crystalline regions (crystal modulus) is one of the significant parameters for evaluating the mechanical properties of polymers.[5–20] The crystal modulus (E_l) in the direction parallel to the chain axis provides information about the polymer's chain conformation in the crystal lattice and the maximum attainable Young's modulus of polymers. The E_l values can be measured from the meridional reflection of highly oriented samples with X-ray diffraction. In previous works, it has been reported that polyethylene with fully extended zig-zag conformation shows a high E_l value (235 GPa), which is higher than the Young's modulus (206 GPa) of steel.[6] Conversely, isotactic polypropylene (*it*.PP) shows the E_l value of 33 GPa. This low E_l value of *it*.PP is attributed to its flexible helical skeleton (3/1 helix), which is very easy to elongate along the chain axis by the stress through internal rotation around the single bonds.[7] With regard to other polymers, for biopolymer, the E_l values of PLLA, poly(*D*-lactic acid) are 14 GPa and that of their stereocomplex was 20 GPa, respectively.[9] The E_l values of natural polymers are determined to be 138 GPa, 88 GPa, 41 GPa, and 65 GPa for cellulose I-form, II-form[16], α-chitin and chitosan.[10] The difference of these E_l values intrinsically depends on the degree of the chain contraction in the crystal lattice.[10,20]

In 1966, PA4's three types of polymorphism, α, β, and δ, were observed and studied by Fredericks *et.al*..[21,22] They have reported that the crystal structure of PA4 α-form was proposed and its atomic coordinates were determined. The unit cell of PA4 α-form belongs to a monoclinic system with a=0.929 nm, b=0.797 nm, c (fiber axis) =1.219 nm and γ=114.5°, in which four zig-zag chains are packed. Several research groups have performed theoretical estimation of E_l of PA4 α-form with the zig-zag conformation. Dasgupta *et.al.* has reported that the E_l value was 243 GPa at 0 K[23], Peeters *et.al*. has reported one as 389 GPa at 0 K with *ab initio* quantum calculations[24], and Fukuda has reported as 334 GPa at 0 K with both ab initio molecular orbital calculations and nuclear magnetic resonance[25]. However, it has been a challenge to evaluate the E_l value of PA4 experimentally. The reason is that the decomposition temperature of PA4 is close to its melting temperature, and the PA4 fibers are decomposed under melt-spinning fiber fabrication process, resulting that highly oriented PA4 fibers were hampered to prepare through melting-spinning process. Recently, the fabrication of PA4 fibers has been achieved, and the further investigation of physical properties of PA4 is able to be performed. Yamane and Xu demonstrated that the melt-spinning of PA4 could be achieved by blending it with the ionic liquid 1-butyl-3-methylimidazolium chloride, which reduced PA4's melting point by 40°C.[26]

In this study, the highly oriented PA4 fibers were prepared by dry spinning followed by thermal drawing. We focus on the determination of the crystal modulus E_l of PA4 α-form parallel to the chain axis from the meridional reflection, and interpretation of their dependence on diffraction planes was performed from the perspective of Laue factor by the change of crystallite size precisely.

1.2. Experimental

1.2.1. Materials

2-pyrrolidone monomer, potassium hydroxide (KOH), sulfuric acid were purchased fromKanto Chemical Co., Inc.. Carbon dioxide gas was purchased from Yokohama Oxygen Co.,Ltd..

1.2.2. Synthesis of PA4

High molecular weight PA4 was synthesized by anionic ring-opening bulk polymerization of 2-pyrrolidone using CO_2 as initiator and KOH as catalyst. (Japanese Patent No.301299) The weight average molecular weight M_w was 1.9×10^6, which was measured by SEC (Tosoh HLC-8320GP EcoSEC, Japan) using hexafluoroisopropanol as solvent and PMMA as molecular weight standard.

1.2.3. Preparation of drawn PA4 fibers

20wt% PA4 solution was prepared by dissolving in formic acid using a sealing mixer (Nakamura Kagaku UZU flask agitator UZ-SM1, Japan) at 50 °C for 18 h. PA4 filament was prepared via dry-spinning using a solution spinning machine (AIKI Riotech Corp., Japan) as follows: the PA4 solution was extruded through a nozzle (diameter: 0.26 mm, length: 13 mm) at discharge rate of 0.18 mL/min at 60 °C. Subsequently, the extruded solution was passed through a tube heater (70 °C) with the length of 13 cm and a windshield tube of ca. 60 cm to form filament by vaporizing formic acid. The winding rate of the filament was 0.94 m/min. The spun fibers were stored in a conditioned room

(20 °C, 65%RH) for 24 h to remove formic acid. The fibers were continuously fed at 0.31 m/min into a tube furnace (Asahi-rika Co., Ltd., ARF1-200-30KC, Japan) set at 260 °C and were drawn to draw ratio of 5.

1.2.4. X-ray fiber photograph

X-ray fiber photograph was recorded on an imaging plate with a camera length of 90 mm. The X-ray beam was irradiated to the fibers in the direction perpendicular to the fiber axis. The X-ray beam with CuKα was generated at 40 kV and 20 mA using a RINT2000 (Rigaku Co.).

The degree of the crystallite orientation π was defined by eq 1.1

$$\pi = \frac{180° - H°}{180°} \tag{1.1}$$

where $H°$ is a half-width of the intensity distribution curve for equatorial 020 reflection of PA4 along the Debye-Scherrer ring.

1.2.5. Tensile test

The tensile test of drawn PA4 single fiber was conducted using a tensile tester (AG–X plus, Shimadzu Co., Japan) at room temperature. The original length was 20 mm, and the strain rate was 0.33 mm/min. From the obtained stress-strain curves, the averaged values of 4 specimens and their standard deviations of Young's modulus E, tensile strength σ_{max}, elongation at break ε_{max} were evaluated. The cross-sectional area of the specimens was calculated using the density, weight and length. Density (1.252 g/cm^3) of the specimen

was measured by a floating method using carbon tetrachloride and toluene.

1.2.6. Thermogravimetric analyses (TGA)

Thermal degradation behavior of the PA4 fibers was measured with a Thermo plus EVO2 TG8121 instrument (Rigaku) under nitrogen gas flow. The sample weight was 5 mg, the flow rate of nitrogen gas was 200 mL/min, the heating rate was 10 °C/min, and the temperature was varied from 100 to 500 °C. The temperature at which 5wt% of the sample weight was lost compared to that at 100 °C was defined as thermal decomposition temperature (T_{d5}).

1.2.7. Differential Scanning Calorimetry (DSC)

The melting point (T_m) and enthalpy of fusion (ΔH) of drawn PA4 fibers were measured using a differential scanning calorimeter (Rigaku Co., DSC 8230) with a sample weight of 5 mg, a heating rate of 10 °C/min and the temperature up to 280 °C. T_m and ΔH were determined as the peak temperature and area of the melting endotherm, respectively.

1.2.8. Elastic Modulus of the Crystalline Regions

X-ray diffraction measurements in the meridional direction for the evaluation of E_l were performed in the symmetric transmittance method using CuKα radiation (wavelength of 1.5418Å, generated at 40 kV and 20 mA) with a RINT2100 (Rigaku.Co.). The scanning rate was 0.1°/min, the step was 0.01°, and the scanning ranges of 2θ were

28° to 31° for 004 reflection, and from 76° to 81° for 0010 reflection, respectively. The cross-sectional area of the specimens was evaluated using the density, weight and length.

The lattice extension under a constant tensile stress was measured with a X-ray diffractometer equipped with a stretching device and a load cell LUB-B (Kyowa Electronic Instruments). The strain ε_l of the crystalline regions along the chain direction was calculated using eq 1.2

$$\varepsilon_l = \Delta d/d_0 \tag{1.2}$$

where d_0 is an initial lattice spacing without tensile stress and Δd is a difference of lattice spacing before and after loading tensile stress. The experimental error in the measurement of the peak shift was within ±0.01° at a 2θ angle.

The stress σ_l in the crystalline regions was assumed to be equal to the stress applied to the sample. This assumption of the homogeneous stress distribution has been proven experimentally for highly oriented PE, cellulose etc..[27,28]

The crystal modulus E_l was calculated by eq 1.3.

$$E_l = \sigma_l/\varepsilon_l \tag{1.3}$$

More details on the measurements for various polymers were reported elsewhere.[12,13,15,17,28,29]

1.2.9 Evaluation of ideal diffraction peak position

The diffraction peaks are generally determined by the structure factor $|\mathrm{F}(\xi,\eta,\zeta)|^2$ and the Laue factor $|\mathrm{G}(\xi,\eta,\zeta)|^2$. In calculation of X-ray diffraction intensity, various

factors, such as polarization, Lorentz factors, and temperature factors, are assumed to be neglected. Therefore, the reflection intensity can be calculated using eq 1.4-1.6.

$$I \propto |\mathrm{F}(\xi,\eta,\zeta)|^2 \cdot |\mathrm{G}(\xi,\eta,\zeta)|^2 \tag{1.4}$$

$$|\mathrm{F}(\xi,\eta,\zeta)|^2 = \left|\sum_j f_j \cos 2\pi\left(\xi x_j + \eta y_j + \zeta z_j\right)\right|^2 + \left|\sum_j f_j \sin 2\pi\left(\xi x_j + \eta y_j + \zeta z_j\right)\right|^2 \tag{1.5}$$

$$|\mathrm{G}(\xi,\eta,\zeta)|^2 = \frac{sin^2\pi L\xi}{sin^2\pi\xi} \cdot \frac{sin^2\pi M\eta}{sin^2\pi\eta} \cdot \frac{sin^2\pi N\zeta}{sin^2\pi\zeta} \tag{1.6}$$

Where, ξ, η and ζ are reciprocal space coordinates in three reciprocal unit vectors $\vec{a}, \vec{b}\ and\ \vec{c}$, f_j stand for atomic scattering factor of jth atom, x_j, y_j and z_j are the atomic coordinates of jth atom in unit cell, and L, M, and N are the numbers of unit cells along the three-crystal axis, corresponding to crystallites size, respectively.

The atomic scattering factor f_j was calculated by eq 1.7 and the value of a_i b_i, and c are shown in Table 1.1

$$f(|\vec{q}|) = \sum_{i=1}^{4} a_i exp\left(-b_i\left(\frac{q}{4\pi}\right)^2\right) + c \tag{1.7}$$

The atomic coordinates of PA4 α-form, x_j, y_j and z_j are shown in the Table 1.2from the works of Fredericks and co-workers.[21]

For the meridional reflections 00ζ, eq 1.4-1.6 can be presented using eq 1.8-1.10

$$I \propto |\mathrm{F}(0,0,\zeta)|^2 \cdot |\mathrm{G}(0,0,\zeta)|^2 \tag{1.8}$$

$$|\mathrm{F}(0,0,\zeta)|^2 = \left|\sum_j f_j \cos 2\pi\left(\zeta z_j\right)\right|^2 + \left|\sum_j f_j \sin 2\pi\left(\zeta z_j\right)\right|^2 \tag{1.9}$$

$$|\mathrm{G}(0,0,\zeta)|^2 = L^2 \cdot M^2 \cdot \frac{sin^2\pi N\zeta}{sin^2\pi\zeta} \tag{1.10}$$

Table. 1.1 Values of a_i, b_i and c_i for C, N, and O elements.

Element	a_1	a_2	a_3	a_4
C	2.31	1.02	1.5886	0.865
N	12.2126	3.1322	2.0125	1.1663
O	3.0485	2.2868	1.5463	0.867

Element	b_1	b_2	b_3	b_4
C	20.8439	10.2075	0.5687	51.6512
N	0.0057	9.8933	28.998	0.5826
O	13.2771	5.7011	0.3239	32.9089

Element	c
C	0.2156
N	-11.529
O	0.2508

Table. 1.2 Atomic coordinates for PA4 α-form.

Atom	x	y	z	Atom	x	y	z
CH_2	0.044	0.007	0.000	CH_2	0.460	0.007	0.000
CH_2	0.040	0.007	0.102	CH_2	0.544	0.007	0.102
CH_2	0.044	0.007	0.204	CH_2	0.460	0.007	0.204
C	0.040	0.007	0.307	N	0.537	0.006	0.307
O	0.160	0.027	0.307	C	0.460	0.007	0.399
N	0.037	0.006	0.399	O	0.340	0.027	0.399
CH_2	0.044	0.007	0.500	CH_2	0.460	0.007	0.500
CH_2	0.040	0.007	0.602	CH_2	0.544	0.007	0.602
CH_2	0.044	0.007	0.704	CH_2	0.460	0.007	0.704
C	0.040	0.007	0.807	N	0.537	0.006	0.807
O	0.160	0.027	0.807	C	0.460	0.007	0.899
N	0.037	0.006	0.899	O	0.340	0.027	0.899
CH_2	0.044	0.507	0.300	CH_2	0.460	0.507	0.300
CH_2	0.040	0.493	0.402	CH_2	0.544	0.493	0.402
CH_2	0.044	0.507	0.504	CH_2	0.460	0.507	0.504
C	0.040	0.493	0.607	N	0.537	0.494	0.607
O	0.160	0.473	0.607	C	0.460	0.507	0.699
N	0.037	0.506	0.699	O	0.340	0.527	0.699
CH_2	0.044	0.507	0.800	CH_2	0.460	0.507	0.800
CH_2	0.040	0.493	0.902	CH_2	0.544	0.493	0.902
CH_2	0.044	0.507	0.004	CH_2	0.460	0.507	0.004
C	0.040	0.493	0.107	N	0.537	0.494	0.107
O	0.160	0.473	0.107	C	0.460	0.507	0.199
N	0.037	0.506	0.199	O	0.340	0.527	0.199

1.2.10 Evaluation of crystallite size

The observed integral width *B* was corrected with the instrumental width *b* of standard sample, silicon (Si), using eq 1.11.

$$\beta^2 = B^2 - b^2 \tag{1.11}$$

where β is the corrected integral width of each reflection.

The integral width (δs) in the reciprocal lattice space was given as eq 1.12

$$\delta_s = \beta \cdot \cos\theta \,/\lambda \tag{1.12}$$

δs is consisted of three components, $(\delta s)_{cs}$ from crystallite size $\overline{D}_{hkl}$, $(\delta s)_{ms}$ from microstrain distortion and $(\delta s)_{pc}$ from paracrystalline distortion as shown in eq 1.13

$$\delta_s = (\delta s)_{cs} + (\delta s)_{ms} + (\delta s)_{pc} \tag{1.13}$$

The broadening $(\delta s)_{cs}$ results from the crystallite size is independent of the order of reflection n as shown in eq 1.14.

$$(\delta s)_{cs} = \frac{1}{\overline{D}_{hkl}} \tag{1.14}$$

where $\overline{D}_{hkl}$ is the crystallite size perpendicular to the (hkl) plane.

On the contrary, the component of broadening by paracrystalline distortion $(\delta s)_{pc}$ is proportional to n^2 in eq 1.15.

$$(\delta s)_{pc} = \frac{1}{\bar{d}_{hkl}} (\pi g_{hkl} n)^2 \tag{1.15}$$

where $\bar{d}_{hkl}$ is lattice spacing of (hkl) plane, n is the order of reflection, and g_{hkl} is paracrystalline distortion and defined by eq 1.16.

$$g_{hkl} = \sqrt{\bar{d}_{hkl}^2 - \bar{d}_{hkl}^2/\bar{d}_{hkl}} \tag{1.16}$$

According to the works of the work of Kaji, the effect of microstrain on the broadening is negligibly small.[30] Therefore, the total integral width is the sum of eq 1.14 and eq 1.15 as eq 1.17.

$$\delta_s = \frac{1}{\bar{D}_{hkl}} + \frac{1}{\bar{d}_{hkl}}(\pi g_{hkl} n)^2 \tag{1.17}$$

As meridional reflections 00l are considered, eq 1.17 is transformed to eq 1.18.

$$\delta_s = \frac{1}{\bar{D}_{001}} + \frac{1}{\bar{d}_{001}}(\pi g_{001} n)^2 \tag{1.18}$$

Thus, the plots of δ_s versus n^2 were approximated by a straight line, and the average crystalline size $\bar{D}_{001}$ is conducted from the intercept. In the case of PA4, the plots of meridional 004 and 0010 reflections provide the change of the crystallite size by loading various tensile stress for n=4 and n=10, respectively.

1.3. Results and Discussion

1.3.1. Properties of drawn PA4 fibers

Table 1.3 summarizes characteristics (crystallite orientation, crystallinity X_c, melting point T_m, enthalpy of fusion ΔH, thermal decomposition temperature T_{d5}, Young's modulus E, tensile strength σ_{max} and elongation at the break ε_{max}) of drawn PA4 fibers. The stress-strain curve, TG curve, DSC curve and equatorial X-ray diffraction profile of drawn PA4 fibers are shown in Figure 1.1. The TG curve shows a single-stage decomposition, with a T_{d5} of 277 °C. The DSC curve shows a melting point T_m of 267 °C. After the melting endotherm, the trace bends downward, indicating a rapid degradation of the PA4 as corresponding to the result of TG. The T_{d5} of PA4 was close to the T_m, which suggests melt-processing of this polymer is a challenge.

Table.1.3 Crystallite orientation, crystallinity X_c, melting point T_m, enthalpy of fusion ΔH, thermal decomposition temperature T_{d5}, Young's modulus E, tensile strength σ_{max} and elongation at the break ε_{max} of drawn PA4 fibers.

Crystallite orientation	0.92
X_c (%)	66
T_m (°C)	269
ΔH (J/g)	106
T_{d5} (°C)	277
E (GPa)	4.6±0.5
σ_{max} (MPa)	920±30
ε_{max} (%)	16.3±1.1

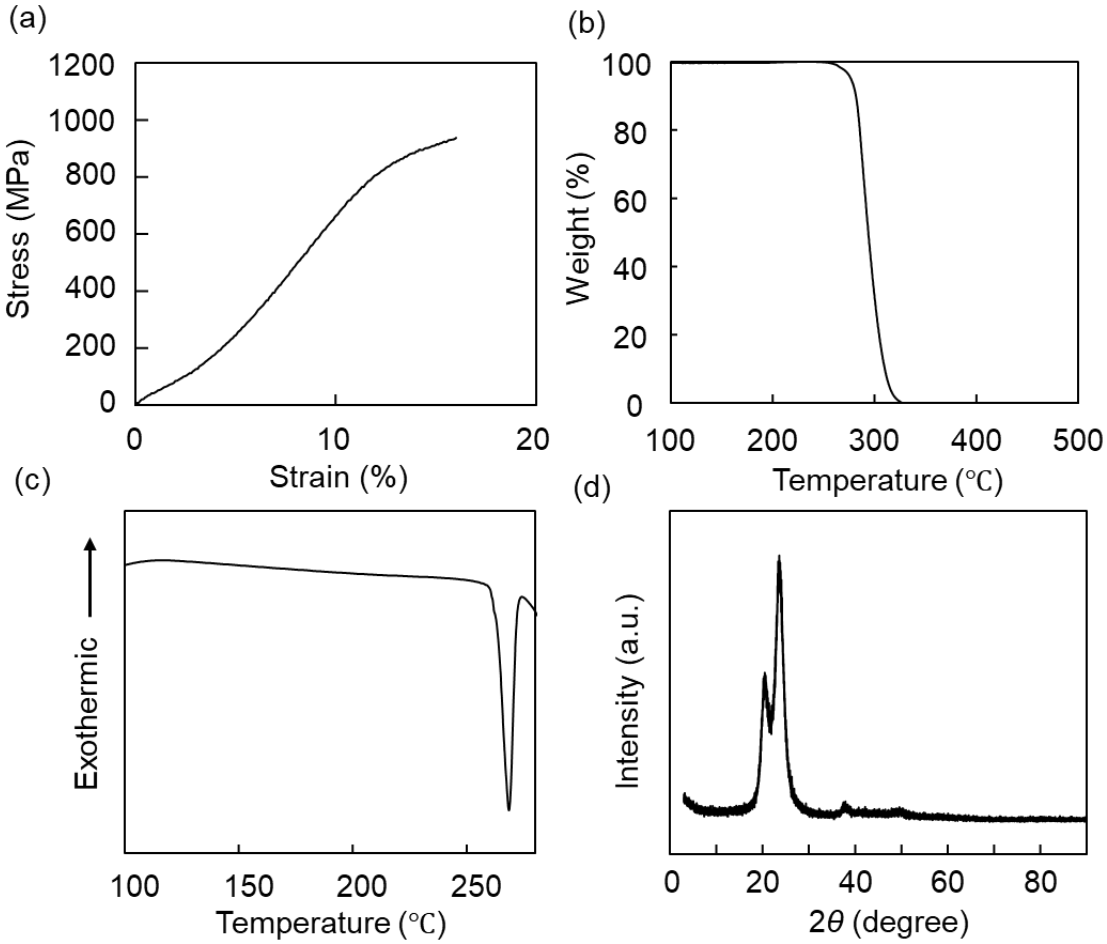

Fig.1.1 (a) Stress-strain curve, (b) TG curve, (c) DSC curve (d) Equatorial X-ray diffraction profile of drawn PA4 fibers.

1.3.2. X-ray fiber photograph

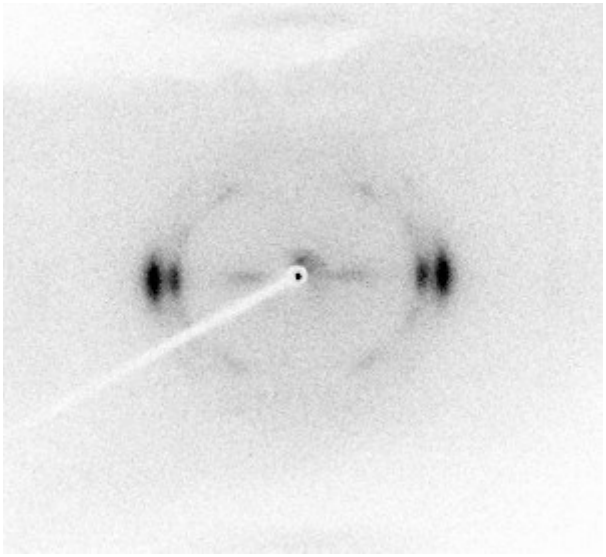

Fig.1.2 X-ray fiber photograph of drawn PA4 fibers.

Figure 1.2 shows the X-ray fiber photograph of dry spun and drawn PA4 fibers. The fiber pattern reveals the fiber possesses high crystallinity and high crystallite orientation. The diffraction patterns could be intrinsically indexed with the reported crystal structure of PA4 α-form with anti-parallel planar zigzag skeleton.[21]

1.3.3. Meridional X-ray diffraction profile

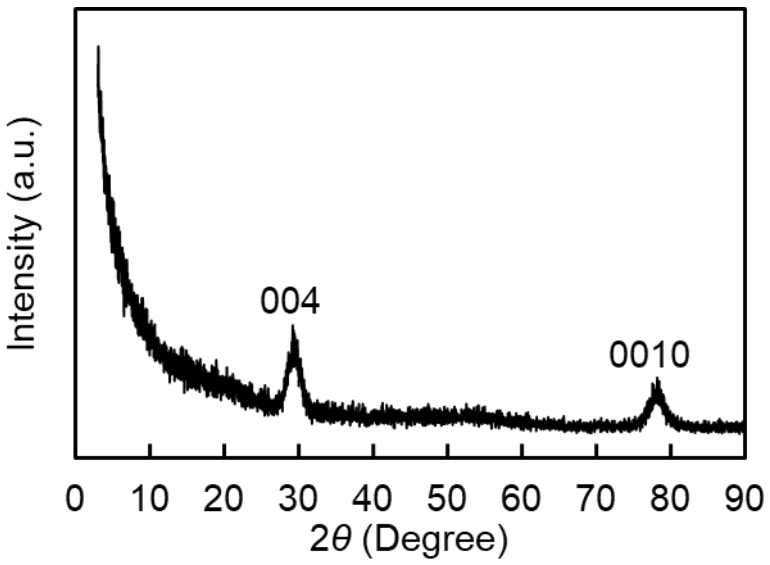

Fig.1.3 Meridional diffraction profile of PA4 drawn fibers.

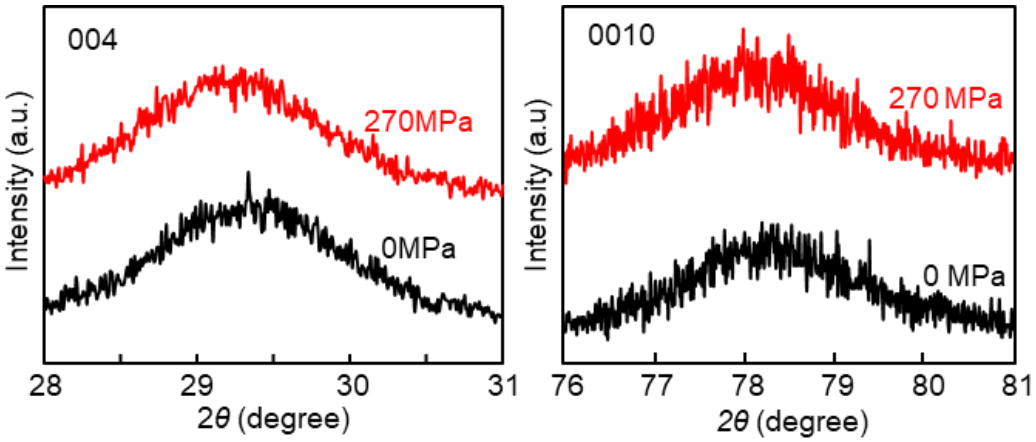

Fig.1.4 X-ray diffraction profiles of 004 and 0010 reflection under and without stress loading.

Figure1.3 shows the meridional diffraction profile of drawn PA4 fibers. Two diffraction peaks were observed at 2θ=29.3° and 78.3°. These diffraction peaks were assigned to (004) and (0010) planes, respectively[21]. Crystal modulus E_l was evaluated from the shifts of these two peaks under loading tensile stress. The X-ray diffraction profiles of

004 and 0010 reflections before and under the stress loading were shown in Figure 1.4. Crystallite size $\overline{D}_{00l}$ along the chain direction of the PA4 was 9.11 nm using eq.1.18 and the number *N* of unit cells along the chain direction was 7.47.

1.3.4 Apparent crystal modulus E_l

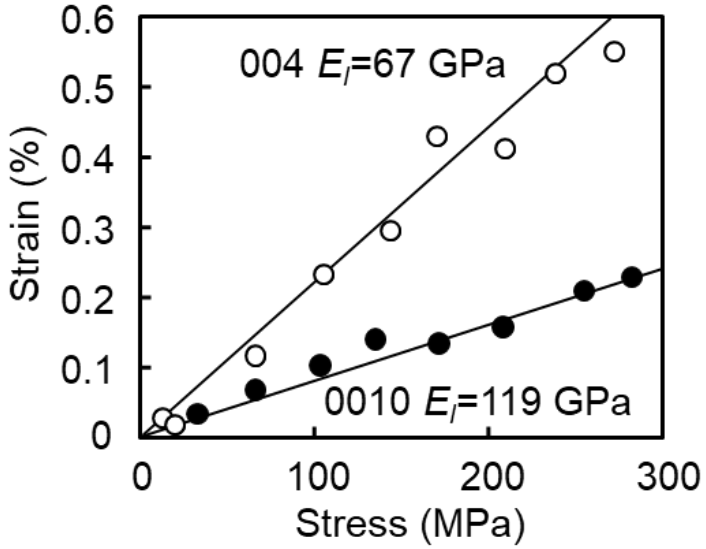

Fig.1.5 Strain−stress curves for (○) the 004 reflection, (●) the 0010 reflection of PA4 at 300 K.

Figure 1.5 shows the strain−stress curves of PA4 fiber at 300K. Plots of 004 and 0010 reflection could be approximated by two different straight lines, respectively. The inclination of these two lines led to different crystal modulus E_l values of PA4 α-form as 67 GPa for 004 reflection and 119 GPa for 0010 reflection apparently. In the X-ray diffraction measurement under loading stress, no other diffraction peaks or shoulders appeared, indicating that no crystal transition occurred in the α-form of PA4. It is curious that the clear difference of E_l value for 004 and 0010 reflections was observed. Because the E_l value of a polymer should be inherently independent of the order of reflection as

reported for most of the polymers.[7,9,31,32] Wallner reported that when the crystallite size along chain direction is small enough such as less than 10 cell units, Laue factor has large impact on the position of the diffraction peak.[33] In particular, the meridional reflection 00l with smaller l value is more sensitive to the change in the crystallite size.[30] For PA6 α-form, when tensile stress increased from 0 to 294 MPa, the number of unit cells along the chain direction N increased from 3.55 to 4.53. This change of N under tensile stress resulted in the extra shift of 004 reflection to lower angle, which brought overestimation of lattice strain, then lower E_l value was obtained. On the contrary, the change of N hardly brings any shift for 0014 reflection. Therefore, the E_l for 0014 reflection can be considered as the most reliable E_l value of PA6 α-form.

1.3.5 Intrinsic crystal modulus E_l

To explain the difference in the E_l measured from 004 and 0010 reflection, the theoretical X-ray diffraction profile of PA4 α-form was calculated with eq. 1.9 and 1.10 using structure factor and Laue factor, and the effect of the crystallite size on the E_l of PA4 was discussed.

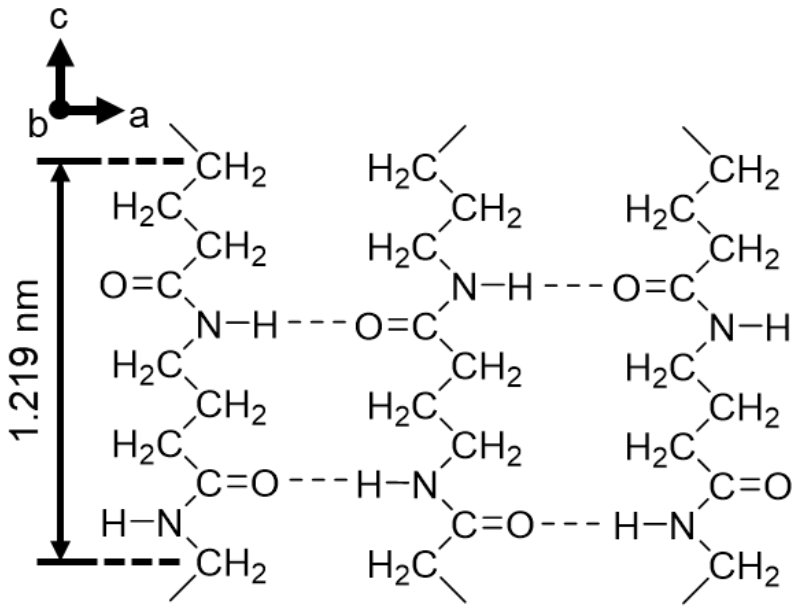

Fig.1.6 Crystal structure of PA4 α-form.

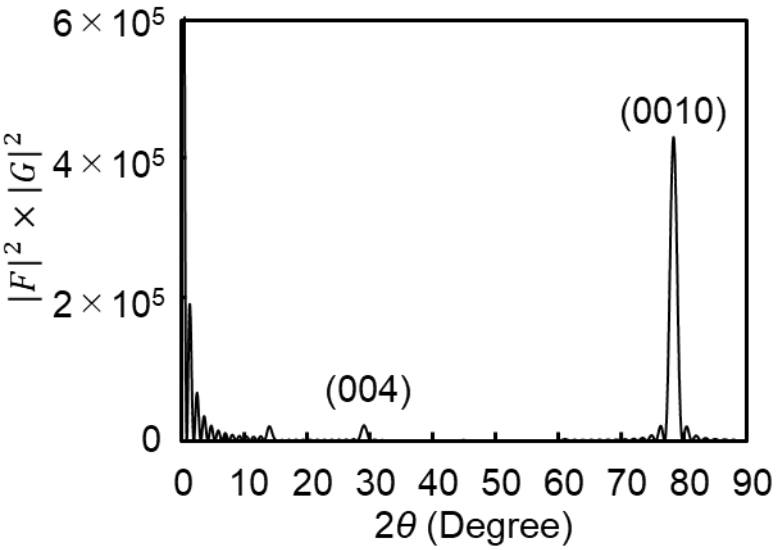

Fig.1.7 Calculated meridional profile of PA4 α-form based on the crystal structure shown in Fig. 1.6. When the *N* was set as 7.5.

Figure 1.6 shows the crystal structure of PA4 with fully extended planar zigzag structure proposed by Fredericks etc.[21]

Figure 1.7 (a) shows a calculated meridional diffraction profile of PA4 α-form. The number *N* of unit cells along the chain direction was set as 7.5. In this case, the value of *L* and *M*, number of unit cells along the x axis and y axis both set as 1. The calculated diffraction peak angles approximately corresponded to those measured for PA4 in Figure 1.3.

Next, we investigated the effect of stress on the crystallite size D along the chain direction of PA4 α-form by the method of Hosemann and Wilke.[34]

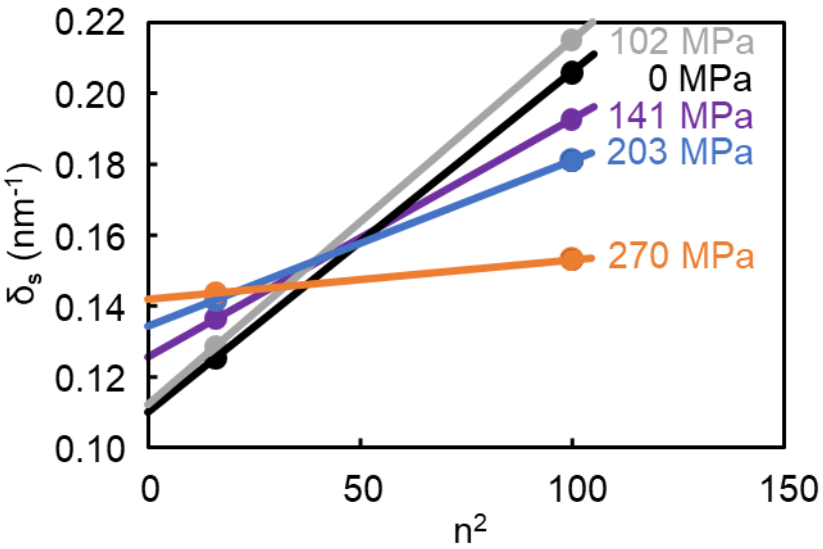

Fig.1.8 The relationship between δ_s and n^2 for the meridional reflections of α-form of PA4 under various stress.

Figure 1.8 shows the relationship between δ_s and square n^2 of the order of reflection with or without loading various tensile stress. The δ_s of 004 reflection increased with loading stress, while the δ_s of 0010 reflection decreased. The intercept values increased as the loading stress increased. This result means the decrease of inherent crystallite sizes

with tensile stress. The crystallite sizes D and paracrystalline distortion $g_{(004)}$ were calculated from the intercepts and inclinations, respectively. The values of D and $g_{(004)}$ are shown in Table 1.4. As the applied stress increased from 0 MPa to 270 MPa, the average crystallite size decreased from 9.11 nm to 7.06 nm, and the values of *N* was declined from 7.47 to 5.79. In addition, the decrease of inclination indicates the paracrystalline distortion also decreased with the increase of loading stress.

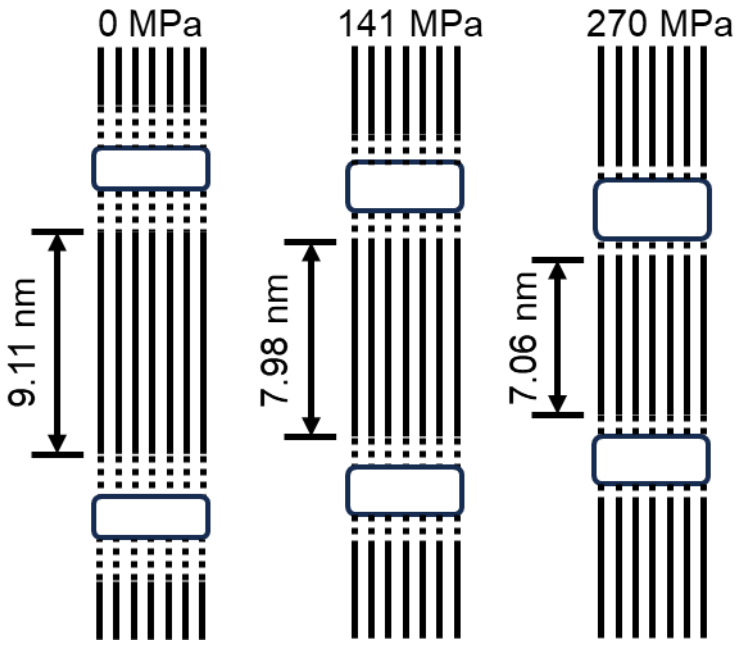

Fig.1.9 The schematic of the decreases of the crystallite size under various stress. The straight-lines represent the crystallite, broken-lines represent the paracrystalline region and the blank blocks represent the amorphous region.

Figure 1.9 shows schematics of the microstructure of PA4 fiber under tensile stress. The straight-lines represent the crystalline regions, broken-lines represent the paracrystalline region and the blank blocks represent the amorphous region. These decreases of the D and $g_{(00l)}$ suggest partial transformation of the crystallites into more

disordered state.

Table.1.4 Development of crystallite size, and paracrystalline distortions $g_{(00l)}$ under various applied tensile stress for PA4 α-form.

Stress	D	*N*	$g_{(00l)}$
MPa	nm		%
0	9.11	7.47	2.83
102	8.95	7.34	2.93
141	7.98	6.54	2.36
203	7.47	6.13	1.98
270	7.06	5.79	0.98

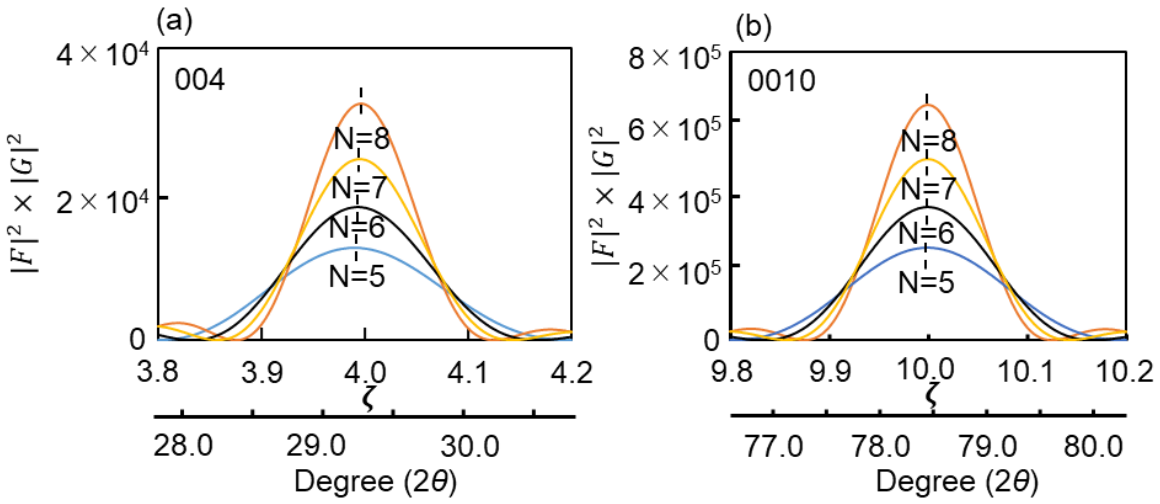

Fig.1.10 Calculated diffraction intensity of (a) 004 and (b) 0010 reflection when *N* set as 8 to 5.

Figure 1.10 (a) and (b) show the calculated diffraction profiles of 004 and 0010 reflection calculated by the eq. 1.8 when the *N* values changed from 5 to 8 according to the Wallner's method.[33] For 004 reflection, the diffraction peak shifted to lower angle

side when *N* decrease from 8 to 5. This indicates that the Laue factor influence on the peak position. On the other hand, the peak position remains constant for 0010 reflection regardless of the *N* value, indicating that there is no influence of the Laue factor for this reflection.

Table. 1.5 Observed lattice strains ε_l of the 004 reflection under various stress and their corrected values ε_{corr} for PA4 α-form.

Stress	Observed lattice strain ε_l	Crystallite size D	Strain resulting from the change of crystallite size ε_{cs}	Corrected lattice strain ε_{corr}
MPa	%	nm	%	%
0	0.000	9.11	0.000	0.000
14	0.053	9.09	0.001	0.053
20	0.023	9.08	0.001	0.022
67	0.143	9.01	0.004	0.139
102	0.153	8.95	0.007	0.147
141	0.21	8.52	0.046	0.164
167	0.291	7.98	0.055	0.236
203	0.271	7.65	0.06	0.211
237	0.351	7.25	0.077	0.275
270	0.361	7.06	0.084	0.277

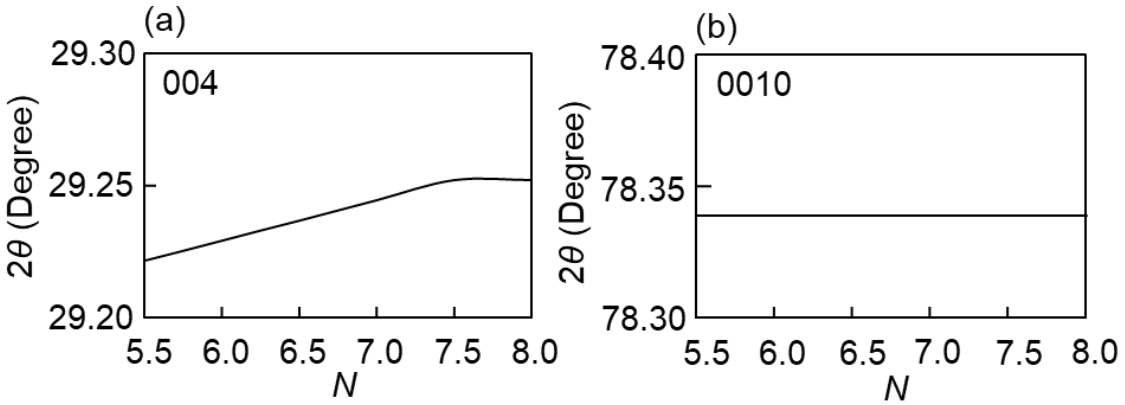

Fig.1.11 Calculated dependence of diffraction angles for (a) 004, (b) 0010 reflection on *N* for PA4 α-form.

Figure 1.11 shows the relationship between the calculated diffraction angles and the number *N* of unit cells for (a) 004 and (b) 0010 reflections. The calculated peak position of the 004 reflection remained unchanged as far as the values of *N* were between 8 and 7.5. Further decreasing the values of *N* from 7.5 to 5.5 leads to a shift of the peak position for the 004 reflection toward the lower angle side from 29.251° to 29.221°. For the 004 reflection, it is necessary to correct the reflection shift due to the decrease of the crystallite size. First, the crystallite sizes under various stress were obtained from Table 1.4, and then the peak position of the 004 reflection corresponding to its crystallite size was obtained from Figure 1.11 (a). The strain ε_{cs} resulting from the decrease of the crystallite size was subtracted from the observed lattice strain ε_l to obtain the corrected lattice strain ε_{corr}. These corrected values are shown in Table 1.5, and the corrected strain-stress curve is shown in Figure 1.12. All the points are almost on a straight line which passes through the origin. The initial slope of the corrected curve provides the E_l value of about 83 GPa. This value is still low, but close to the E_l value of 119 GPa obtained from the 0010 reflection. In contrast from the results for the 004 reflection, calculated peak position for

the 0010 reflection remains constant at 78.340° even with the increase of values of N as shown in Figure1.11 (b). When a stress of 270 MPa was applied to the fibers, N decreased from 7.5 to 5.8. In this range, the calculated diffraction angle of the 004 reflection shifts from 29.276° to 29.245° with the decrease of crystallite size, while that of 0010 reflection remains constant. Therefore, the E_l of 0010 reflection remain unchanged as 119 GPa. Accordingly, it can be concluded that the reliable and accurate E_l value of PA4 α-form is 119 GPa.

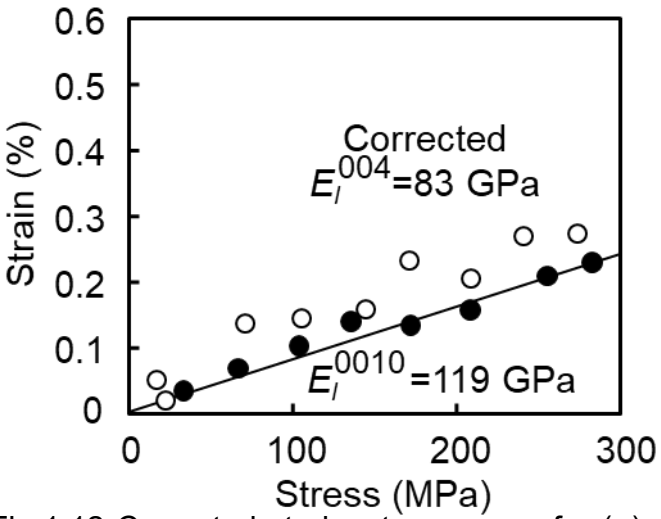

Fig.1.12 Corrected strain−stress curve for (○) the 004 reflection of PA4 at 300 K, strain−stress curve for (●) the 0010 reflection of PA4 at 300 K was expressed by filled

The E_l values of various polyamides have been evaluated.[7,19,35] Their E_l values strongly depend on the contraction of polymer chain axis from their fully extended planar zigzag conformation.

Figure 1.13 shows the relationship between the observed E_l and the percentage of

contraction from fully extended planar zigzag conformation of various polyamides. The E_l values decreases drastically with the contraction of the skeleton for the series of polyamides. Natta *et al.* proposed the contraction of the skeleton of PA6 through thermal vibration around amide linkages. Based on this idea of the skeleton contraction, Tashiro *et al.* calculated the E_l value of PA6 α-form, as shown with the solid line in Figure 1.13 [35] Because calculated trend of the relationship between the E_l values and the contraction is affected by the uncertainness of the calculated fiber period due to bond lengths and angles uncertainties. Thus the absolute value of the calculated E_l does not coincide the experimental E_l value, but the both trends resemble each other. Accordingly, the E_l values of polyamides, including that for PA4, are considered to be highly influenced by the chain contraction. The E_l value of PA 4 was at an intermediate level among various polyamides, which is higher than those of PA12 and PA46, but smaller than those of PA6, PA66, and PA610. The experimental E_l value of 119 GPa for PA4 is much lower than the calculated values of 243 GPa, 389 GPa and 334 GPa mentioned above.[23–25] The measured fiber period of 1.219 nm is shorter by about 1.9% than the calculated value of 1.243 nm for a fully extended planar zigzag conformation. The reason for the chain contraction of 1.9% is considered to be arose from the existence of torsional conformations at the amino group as proposed for PA6 α-form.

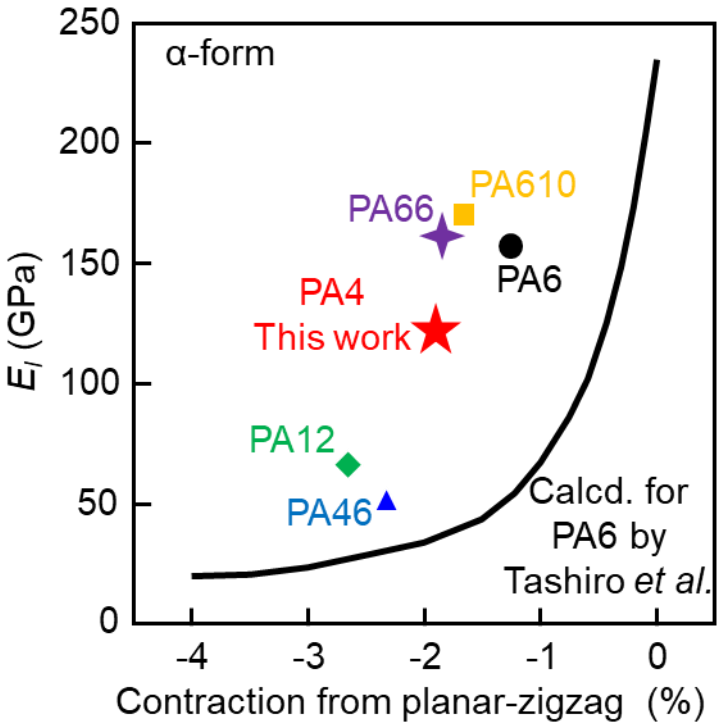

Fig.1.13 Relationship between the E_l and the contraction of the fiber period from the planar zigzag conformation of various polyamides α-form.

1.4 Conclusions

Highly oriented PA4 fibers were prepared by dry-spinning and drawing. The crystal modulus E_l was measured by X-ray diffraction under loading tensile stress. The of E_l values as 67 GPa are obtained from 004 and 119 GPa from 0010 reflection, respectively. This difference was attributed to the decrease of crystallite size when the stress was applied to the fibers proved through Hosemann's method and Wallner's method with calculation of structure factor and Laue factor. When the applied stress increased from 0 to 270 MPa, the number of unit cells along the chain direction in a crystallite were declined from 7.5 to 5.8. It was revealed that lower E_l value of 004 reflection resulted from the apparently higher peak shifts with load than actual influenced by the Laue factor. When corrected this fact, the E_l of 0010 reflection was considered as the most reliable value of α-form PA4, 119 GPa. This value is lower than the E_l of PA610, PA66 and PA6 but higher than that of PA46 and PA12. The E_l of PA4 is significantly lower than the calculated values, which will be attributed to a 1.9% contraction of the PA4 chains from the fully extended planar zigzag conformation.

1.5. References

[1] K. Hashimoto, T. Hamano, M. Okada, Degradation of several polyamides in soils, J Appl Polym Sci 54 (1994) 1579–1583. https://doi.org/10.1002/app.1994.070541023.

[2] K. Tachibana, Y. Urano, K. Numata, Biodegradability of nylon 4 film in a marine environment, Polym Degrad Stab 98 (2013) 1847–1851. https://doi.org/10.1016/j.polymdegradstab.2013.05.007.

[3] K. Tachibana, K. Hashimoto, M. Yoshikawa, H. Okawa, Isolation and characterization of microorganisms degrading nylon 4 in the composted soil, Polym Degrad Stab 95 (2010) 912–917. https://doi.org/10.1016/j.polymdegradstab.2010.03.031.

[4] N. Yamano, A. Nakayama, N. Kawasaki, N. Yamamoto, S. Aiba, Mechanism and Characterization of Polyamide 4 Degradation by Pseudomonas sp., J Polym Environ 16 (2008) 141–146. https://doi.org/10.1007/s10924-008-0090-y.

[5] K. Nakamae, T. Nishino, H. Ohkubo, Elastic modulus of crystalline regions of polyethylene with different microstructures: Experimental proof of homogeneous stress distribution, Journal of Macromolecular Science, Part B 30 (1991) 1–23. https://doi.org/10.1080/00222349108245780.

[6] K. Nakamae, T. Nishino, Crystal Moduli of High Polymers and Their Temperature Dependence, in: Integration of Fundamental Polymer Science and Technology—5, Springer Netherlands, Dordrecht, 1991: pp. 121–130. https://doi.org/10.1007/978-94-011-3890-1_16.

[7] I. Sakurada, K. Kaji, relation between the polymer conformation and the elastic modulus of the crystalline region of polymer, Journal of Polymer Science Part C: Polymer Symposia 31 (1970) 57–76. https://doi.org/10.1002/polc.5070310108.

[8] S. Lee, C. Hongo, T. Nishino, Crystal Modulus of Poly(glycolic acid) and Its Temperature Dependence, Macromolecules 50 (2017) 5074–5079. https://doi.org/10.1021/acs.macromol.7b00753.

[9] S. Lee, M. Kimoto, M. Tanaka, H. Tsuji, T. Nishino, Crystal modulus of poly (lactic acid)s, and their stereocomplex, Polymer (Guildf) 138 (2018) 124–131. https://doi.org/10.1016/j.polymer.2018.01.051.

[10] T. Nishino, R. Matsui, K. Nakamae, Elastic modulus of the crystalline regions of chitin and chitosan, J Polym Sci B Polym Phys 37 (1999) 1191–1196. https://doi.org/10.1002/(SICI)1099-0488(19990601)37:11<1191::AID-POLB13>3.0.CO;2-H.

[11] A.J. Uddin, Y. Gotoh, Y. Ohkoshi, T. Nishino, R. Endo, Crystal modulus of a new semiaromatic polyamide 9-T, Polym Eng Sci 52 (2012) 331–337. https://doi.org/10.1002/pen.22086.

[12] K. Nakamae, T. Nishino, H. Ohkubo, S. Matsuzawa, K. Yamaura, Studies on the temperature dependence of the elastic modulus of crystalline regions of polymers: 14. Poly(vinyl alcohol) with different tacticities, Polymer (Guildf) 33 (1992) 2581–2586. https://doi.org/10.1016/0032-3861(92)91141-N.

[13] T. Nishino, N. Miki, Y. Mitsuoka, K. Nakamae, T. Saito, T. Kikuchi, Elastic modulus of the crystalline regions of polyimide derived from poly(amic acid)-

biphtalic dianhydride andp-phenylene diamine, J Polym Sci B Polym Phys 37 (1999) 3294–3301. https://doi.org/10.1002/(SICI)1099-0488(19991201)37:23<3294::AID-POLB4>3.0.CO;2-J.

[14] K. Nakamae, T. Nishino, Y. Shimizu, T. Matsumoto, Experimental Determination of the Elastic Modulus of Crystalline Regions of Some Aromatic Polyamides, Aromatic Polyesters, and Aromatic Polyether Ketone, Polym J 19 (1987) 451–459. https://doi.org/10.1295/polymj.19.451.

[15] K. Nakamae, T. Nishino, K. Hata, T. Matsumoto, Studies on the temperature dependence of the elastic moduli of crystalline regions of polymers. VII. Temperature dependence of the elastic modulus of crystalline regions of Nylon 6., Kobunshi Ronbunshu 44 (1987) 421–428. https://doi.org/10.1295/koron.44.421.

[16] T. Nishino, K. Takano, K. Nakamae, Elastic modulus of the crystalline regions of cellulose polymorphs, J Polym Sci B Polym Phys 33 (1995) 1647–1651. https://doi.org/10.1002/polb.1995.090331110.

[17] K. Nakamae, T. Nishino, Y. Shimizu, T. Matsumoto, Experimental Determination of the Elastic Modulus of Crystalline Regions of Some Aromatic Polyamides, Aromatic Polyesters, and Aromatic Polyether Ketone, Polym J 19 (1987) 451–459. https://doi.org/10.1295/polymj.19.451.

[18] I. Sakurada, T. Ito, K. Nakamae, Elastic moduli of polymer crystals for the chain axial direction, Die Makromolekulare Chemie 75 (1964) 1–10. https://doi.org/10.1002/macp.1964.020750101.

[19] K. Kaji, I. Sakurada, Determination of the elastic modulus of polyamide crystals

along the chain axis by x-ray diffraction, 1. The α-form of nylon-6, Die Makromolekulare Chemie 179 (1978) 209–217. https://doi.org/10.1002/macp.1978.021790121.

[20] Y. Ogawa, R. Hori, U.-J. Kim, M. Wada, Elastic modulus in the crystalline region and the thermal expansion coefficients of α-chitin determined using synchrotron radiated X-ray diffraction, Carbohydr Polym 83 (2011) 1213–1217. https://doi.org/10.1016/j.carbpol.2010.09.025.

[21] R.J. Fredericks, R.S. Sprague, Crystallographic Studies of Nylon 4. I. Determination of the Crystal Structure of the α Polymorph of Nylon 4, J Polym Sci A 4 (1966) 899–911. https://doi.org/https://doi.org/10.1002/pol.1966.160040606.

[22] R.J. Fredericks, T.H. Doyne, R.S. Sprague, Crystallographic studies of nylon 4. II. On the β and δ polymorphs of nylon 4, J Polym Sci A 4 (1966) 913–922. https://doi.org/10.1002/pol.1966.160040607.

[23] S. Dasgupta, W.B. Hammond, W.A. Goddard, Crystal Structures and Properties of Nylon Polymers from Theory, J Am Chem Soc 118 (1996) 12291–12301. https://doi.org/10.1021/ja944125d.

[24] A. Peeters, C. Van Alsenoy, F. Bartha, F. Bogár, M.-L. Zhang, V.E. Van Doren, *Ab initio* calculation of the Young's modulus of α-polyamides, Int J Quantum Chem 87 (2002) 303–310. https://doi.org/10.1002/qua.10121.

[25] Y. Fukuda, Y. Sasanuma, Computational Characterization of Nylon 4, a Biobased and Biodegradable Polyamide Superior to Nylon 6, ACS Omega 3 (2018) 9544–9555. https://doi.org/10.1021/acsomega.8b00915.

[26] T. Nagahama, S. Yagi, H. Yamane, H. Xu, Melt spinning of polyamide 4, Polym Adv Technol 33 (2022) 3658–3665. https://doi.org/10.1002/pat.5818.

[27] K. Nakamae, T. Nishino, H. Ohkubo, Elastic modulus of crystalline regions of polyethylene with different microstructures: Experimental proof of homogeneous stress distribution, Journal of Macromolecular Science, Part B 30 (1991) 1–23. https://doi.org/10.1080/00222349108245780.

[28] I. Sakurada, T. Ito, K. Nakamae, Elastic Moduli of Polymer Crystals for the Chain Axial Direction, Die Makromolekulare Chemie 75 (1964) 1–10. https://doi.org/10.1002/macp.1964.020750101.

[29] T. Nishino, K. Tada, K. Nakamae, Elastic modulus of crystalline regions of poly(ether ether ketone), poly(ether ketone) and poly(p-phenylene sulphide), Polymer (Guildf) 33 (1992) 736–743. https://doi.org/10.1016/0032-3861(92)90330-Y.

[30] K. Kaji, Increase of the Crystallite Size by Application of Tensile Stress for Highly Oriented Polymer, Die Makromolekulare Chemie 175 (1974) 311–325. https://doi.org/10.1002/macp.1974.021750131.

[31] I. Sakurada, Y. Nukushina, T. Ito, Experimental determination of the elastic modulus of crystalline regions in oriented polymers, Journal of Polymer Science 57 (1962) 651–660. https://doi.org/10.1002/pol.1962.1205716551.

[32] K. Nakamae, T. Nishino, H. Ohkubo, Elastic modulus of crystalline regions of polyethylene with different microstructures: Experimental proof of homogeneous stress distribution, Journal of Macromolecular Science, Part B 30 (1991) 1–23.

https://doi.org/10.1080/00222349108245780.

[33] L.G. Wallner, Über den Einfluß der Kristallitlänge auf die Röntgen-Interferenzen der Polyamide, Monatshefte Für Chemie Und Verwandte Teile Anderer Wissenschaften 79 (1948) 279–295. https://doi.org/10.1007/BF00899404.

[34] R. Hosemann, Röntgeninterferenzen an Strichgittern mit Flüssigkeitsunordnung, Zeitschrift Für Physik 127 (1950) 16–40. https://doi.org/10.1007/BF01338981.

[35] K. Tashiro, H. Tadokoro, Calculation of three-dimensional elastic constants of polymer crystals. 3. α and γ Forms of nylon 6, Macromolecules 14 (1981) 781–785. https://doi.org/10.1021/ma50004a060.

CHAPTER II

Stress Transfer Analysis of Poly(*L*-lactic acid) / Hydroxyapatite Composites by Synchrotron Radiation

2.1 Introduction

Owing to increasing concerns about global warming and the depletion of petroleum resources, bio-based polymers have emerged as promising alternatives to conventional petroleum-derived polymers. [1] Among the diverse biobased polymers, poly(*L*-lactic acid) (PLLA) has garnered significant attention because of its notable biodegradability, biocompatibility, and processability. [2] These properties have facilitated wide adoption across various industrial fields, including biomedical, agricultural, packaging, and textile applications. However, the relatively low mechanical strength of PLLA has limited its broader utilization, particularly in the development of high-performance bone scaffolds. To overcome this limitation, researchers have investigated the incorporation of organic and inorganic fillers, such as cellulose nanocrystals, magnesium hydroxide, graphene, and graphene oxide, into PLLA matrices to increase their mechanical performance. [3–8]

Hydroxyapatite (HAp), with the chemical formula $Ca_{10}(PO_4)_6(OH)_2$, is a bioactive and nontoxic ceramic, that structurally resembles the inorganic components of bone and has excellent mechanical properties. [9] Due to its bioactive and osteoconductive nature, HAp can establish chemical bonds with living tissues. Consequently, HAp has been widely utilized in many medical applications, particularly in dentistry and orthopedic surgery. [10,11]

To integrate and combine the advantages of each component, a PLLA/HAp composite was fabricated as a biomaterials and employed for the reconstruction and repair of bone defects. Various methods, such as electron spinning and additive manufacturing, have been used to prepare PLLA/HAp composites. [12–19] In the case of PLLA/HAp composites, the intrinsic properties of the filler and the matrix and the interaction at the

filler/matrix interface affect the mechanical performance of the entire composite. [20–23] Therefore, a comprehensive understanding of the interfacial stress transfer in PLLA/HAp composites is crucial for their application.

X-ray diffraction has been used to investigate the interfacial stress transfer mechanism in various composite systems, such as epoxy/silica [24], epoxy/carbon fiber [25], PLLA/kenaf [26], poly(vinyl alcohol)/montmorillonite [27] and cellulose-nanofiber/montmorillonite. [28] The stress transferred to the filler along the stretching direction was quantitatively evaluated from the shift in the X-ray diffraction peak when the entire composite was under applied stress. Due to its high brilliance, synchrotron radiation can be used to obtain a clear diffraction pattern of the crystalline fillers in the composites with low filler loading (<5 wt %). Recent advancements in synchrotron X-ray diffraction and high-resolution X-ray detectors have enhanced the ability to assess lattice strain within the composites at the microscale, achieving unprecedented resolution. [29–31]

In this study, the stress transfer phenomena in PLLA/HAp composites filled with nanosized HAp or micro-sized HAp under tensile deformation were investigated by *in situ* synchrotron wide-angle X-ray diffraction (WAXD). The diffraction peak of the (211) plane of HAp was used in the stress transfer analysis. The mechanical reinforcement effects of HAp fillers in composites on HAp particle sizes and fraction ratios were evaluated by stress transfer analyses. The interfacial states of the composites under tensile deformation were assessed by comparing the stress σ_c transferred to the HAp fillers with the stress σ_0 applied to the entire composite. Moreover, in this research, we investigated the interfacial failure modes and the effects of the particle size of HAp in PLLA/HAp

composites to gain insight into the mechanical behavior of the composites under tensile deformation.

2.2. Experimental

2.2.1. Materials

PLLA pellets (M_w=1.8×10^5) were kindly supplied from Unitika Trading Co., Ltd. (4032DK). PLLA pellets were dried in a vacuum at 40 °C for 24 hours before used. The micro-HAp (m-HAp, grain size Φ=1 μm) and nano-HAp (n-HAp, Φ=200 nm) were purchased from ECCERA Ltd. and Sigma-Aldrich, respectively. Both m-HAp and n-HAp were dried in a vacuum at 100 °C for 24 h to remove absorbed moisture before being used in the experiment. Chloroform and methanol were purchased from Nacalai Tesque, Inc. without any further purification.

2.2.2. Preparation of PLLA/HAp composites

PLLA/m-HAp and PLLA/n-HAp composites with various ratios of HAp were fabricated through reprecipitation and hot-pressing techniques. At first, PLLA pellets and HAp powder were added to 20 mL of chloroform and stirred at room temperature for 24 h, resulting in chloroform dispersion with PLLA and HAp. The total weights of PLLA pellets and HAp powder were 1.00 g. Subsequently, the dispersion was reprecipitated into 350 mL of methanol to obtain the solid mixture of PLLA and HAp. The mixtures of PLLA/HAp were then dried under a vacuum at 40 °C for 24 h to remove solvents. The weight fractions of HAp in the solid mixture were 5, 10, 20, 30, and 40wt%. The PLLA/HAp mixtures were pressed using a hot-pressing machine (Gonno Hydraulic Machinery Mfg. Co., Ltd.) at 200 °C, 5 MPa for 1 min, followed by quenching into ice water, with the purpose of the fabrication of PLLA/m-HAp and PLLA/n-HAp composites

with various HAp contents (5-40wt%). The thickness of the composites was 200 μm. The constitution of the PLLA/m-(n-)HAp (5, 10, 20, 30, 40) composites are shown in Table 2.1.

Table. 2.1 Constitution of neat PLLA, PLLA/n-HAp and PLLA/m-HAp with various HAp contents.

Sample	PLLA	HAp	Mass fraction of HAp	Volume fraction of HAp
	g	g	%	%
PLLA	1.00	0	0	0
PLLA/m-HAp 5	0.95	0.05	5	2
PLLA/m-HAp 10	0.90	0.10	10	4
PLLA/m-HAp 20	0.80	0.20	20	9
PLLA/m-HAp 30	0.70	0.30	30	15
PLLA/m-HAp 40	0.60	0.40	40	21
PLLA/n-HAp 5	0.95	0.05	5	2
PLLA/n-HAp 10	0.90	0.10	10	4
PLLA/n-HAp 20	0.80	0.20	20	9
PLLA/n-HAp 30	0.70	0.30	30	15
PLLA/n-HAp 40	0.60	0.40	40	21

2.2.3. Tensile tests

The tensile tests of samples were performed using a tensile tester (AG–X plus, Shimadzu Co., Japan) at room temperature. The samples were trimmed into rectangles (length 30 mm × width 5 mm). The initial length in the tensile tests was 10 mm, and the strain rate was 1 mm/min. From the obtained stress-strain curves of 5 specimens, the averaged values and standard deviations of Young's modulus, tensile strength, and elongation at break were calculated.

2.2.4. Observation with field emission-scanning electron microscope (FE-SEM)

For the observation of the morphology of n-HAp and m-HAp fillers and cross-sections of neat PLLA film, PLLA/m-HAp composites, and PLLA/n-HAp composites, an FE-SEM instrument (Japan Electron Co., Ltd., JSM-7100F) was utilized with an acceleration voltage of 5 kV and an irradiation current of 8 nA. Before observation, the samples were deposited with an osmium coater (Neoc-Pro/P, Meiwafosis Co., Ltd.). The cross-sections were formed by breaking the samples through freeze-fracturing in liquid nitrogen.

2.2.5. WAXD measurement

WAXD profiles of n-HAp, m-HAp, neat PLLA, PLLA/m-HAp 5, and PLLA/n-HAp 5 were measured using an X-ray diffractometer (SmartLab 3kW, Rigaku Corporation). The X-ray beam of the CuKα tube with 1.5418Å of wavelength was generated at a tube voltage of 40 KV and a tube current of 30 mA. The scanning speed was 50°/min, the sampling step was 0.004°, and the scanning range of 2θ was from 5 to 60°.

2.2.6. Thermogravimetric analyses (TGA)

Thermal degradation behaviors of neat PLLA, PLLA/m-HAp composites, and PLLA/n-HAp composites, m-HAp, n-HAp fillers were evaluated using a thermogravimetry (Thermo plus EVO II TG8121, Rigaku Co., Japan) with each sample weight of 5 mg using Al pans. The thermograms of samples were obtained under a nitrogen atmosphere at a heating rate of 10 °C/min. The scanned temperatures ranged from 30 °C to 400 °C. The samples' thermal decomposition temperature (T_{d5}) was

measured from the thermograms. T_{d5} was defined as a temperature where 5% of sample thermal weight lost thermally.

2.2.7 *In situ* stress transfer analyses

The stress transfer behaviors of PLLA/HAp composites were evaluated using *in situ* tensile tests while recording wide-angle X-ray diffraction (WAXD) patterns with synchrotron radiation on the FSBL BL03XU beamline at SPring-8, Japan, as shown in Figure 2.1 (a). Figure 2.1 (b) shows the geometries of X-ray beam, samples, and detector in the measurement. The synchrotron radiation's vertical and horizontal beam size was 50 μm×150 μm, and the X-ray wavelength was 0.1 nm with 12.4 KeV of the photon energy. The diffraction patterns were recorded by a high-resolution silicon-on-insulator photon imaging array sensor (SOPHIAS) with a pixel size of 30 μm×30 μm and a detection area of 26.7 mm×64.8 mm. [29–31]

PLLA/HAp composites were trimmed into rectangles with a length of 25 mm × width of 5 mm for *in situ* stress transfer measurement. The samples were set on a Linkam tensile tester (TST-350 Tensile Testing System, LINKAM SCIENTIFIC), and the silicon powder was used as a calibration standard. The tilt angle of the Linkam stage was 10.3°. The diffraction patterns were measured every 0.5 sec during the tensile tests, and the exposure time was 0.4 sec in each diffraction measurement. The irradiation time provided sufficient intensity to facilitate the reliable fitting of the diffraction peaks. The distance between the sample and the detector was 114 mm. The initial length of the sample was 15 mm, and the strain rate was 0.015 mm/s.

Figure 2.1 (c) shows the example of the X-ray diffraction pattern of the PLLA/n-HAp 5 composite. The obtained two-dimensional diffraction patterns were converted to one-dimensional X-ray diffraction 2θ profiles via MDIP software. The horizontal direction in Figure 2.1 (c) corresponded to the meridional and stretching direction, which was set as $\psi = 0°$. The 2θ profiles were obtained through the integration within the range of ψ = -5~5°. Gaussian fitting of the diffraction peaks in obtained profiles provided the individual peak position. From the shift of diffraction peaks from the (211) plane of HAp crystal at $2\theta = 20.6°$, the strain ε_c of the HAp crystallite was calculated using the eq 2.1. From eq 2.2, the stress σ_c transferred to the HAp fillers during tensile tests was calculated using obtained strains ε_c and crystal modulus of (211) plane of HAp. Interfacial states of the composites during the *in situ* measurement can be monitored from the stress transferred to HAp fillers in the composites. Additionally, the stress transfer coefficient $\chi = \sigma_c/\sigma_0$ was estimated.

$$\varepsilon_c = (d - d_0)/d_0 \tag{2.1}$$

$$\sigma_c = \varepsilon_c \times E_{(211)} \tag{2.2}$$

where d_0 is the lattice spacing of the (211) plane before stress is applied, and d is the lattice spacing under stress loading. $E_{(211)}$ is the elastic modulus of HAp crystal for the (211) plane. The $E_{(211)}$ is 86 GPa, which was calculated from the crystal elastic stiffness of HAp crystal. [32] The interfacial states in the composites during the tensile deformation were estimated by comparing stress σ_c transferred to the HAp fillers with the stress σ_0 applied to the whole composites.

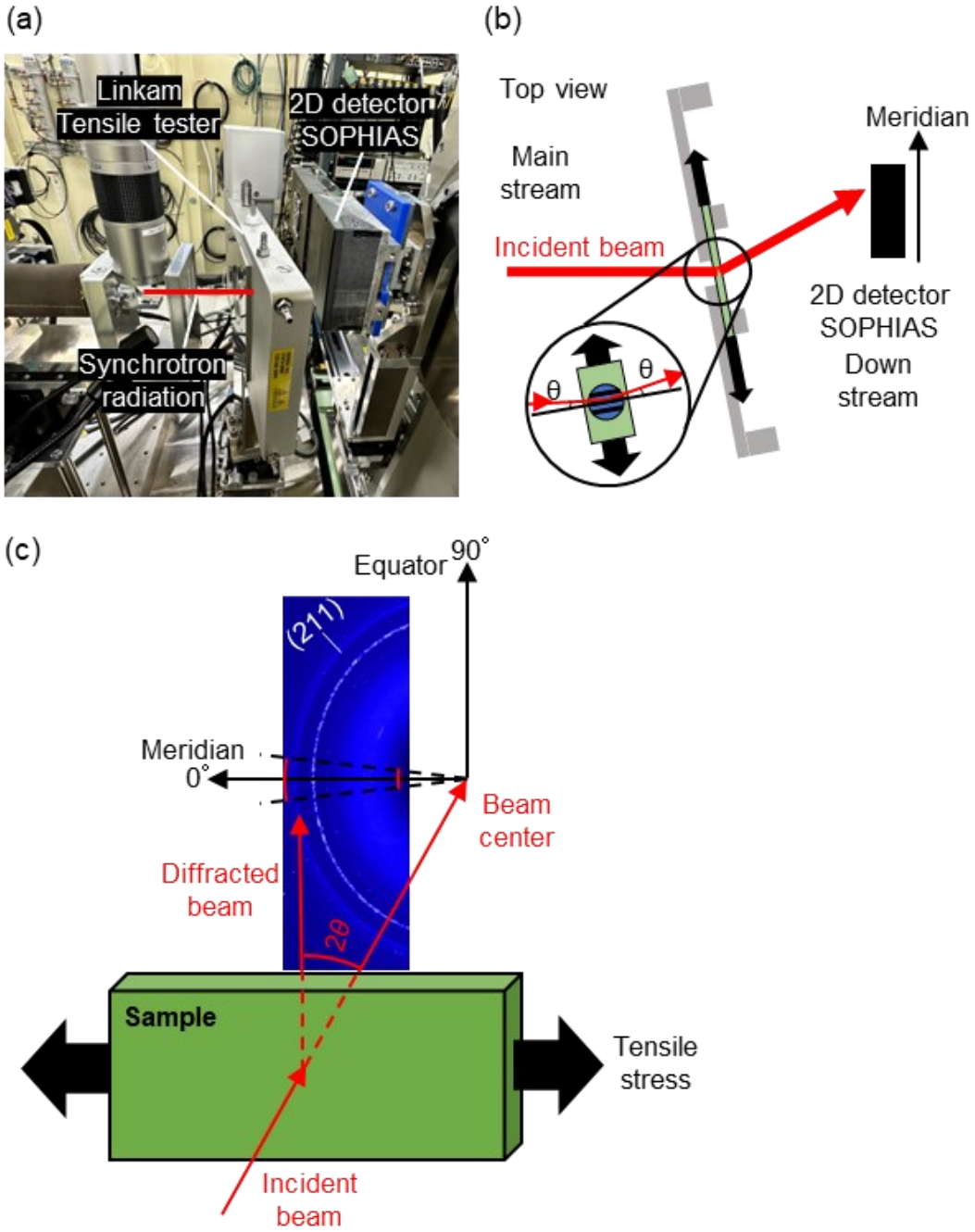

Fig. 2.1 (a) Layout and (b) conceptual scheme for *in situ* stress transfer measurement with synchrotron radiation. (c) Example of the X-ray diffraction patterns. The red arcs and dashed lines show the boundary of the processing region.

2.3. Results and discussion

2.3.1. Morphology of the composites

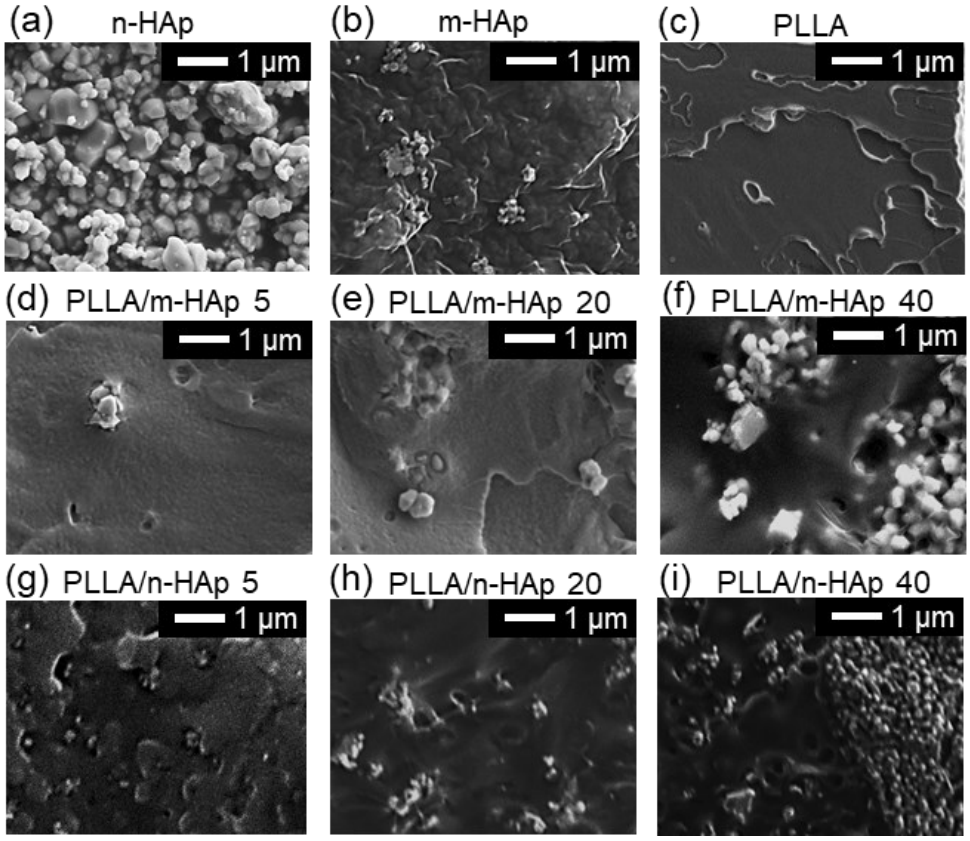

Fig. 2.2 FE-SEM images of (a) m-HAp, (b) n-HAp fillers and cross-section of (c) neat PLLA, PLLA/m-HAp (d) 5 (e) 20 and (f) 40, and PLLA/n-HAp (g) 5 (h) 20 and (i) 40 composites.

Figure 2.2 shows FE-SEM images of (a) m-HAp and (b) n-HAp fillers, cross sections of (c) neat PLLA, PLLA/m-HAp (d) 5 (e) 20 and (f) 40 and PLLA/n-HAp (g) 5 (h) 20 and (i) 40 composites. In Figures 2 (a) and (b), m-HAp and n-HAp exhibited spherical shapes. The cross-section of neat PLLA film possessed a smooth surface without fillers observed, as shown in Figure 2.2 (c). In Figure 2.2 (d) m-HAp fillers and the voids in the cross-section of PLLA/m-HAp 5 were observed. These voids would be caused by the

interfacial debonding. As the HAp contents were increased in Figures 2 (e) and (f), m-HAp fillers were aggregated and acted as defects, reducing the mechanical properties of the composites. In the cross-section of PLLA/n-HAp 5 in Figure 2.2 (g), the n-HAp fillers were highly dispersed into the PLLA matrix. In Figures 2 (h) and (i), PLLA/n-HAp 20 and 40 composites possessed the aggregation of n-HAp.

2.3.2. Structure of the composites

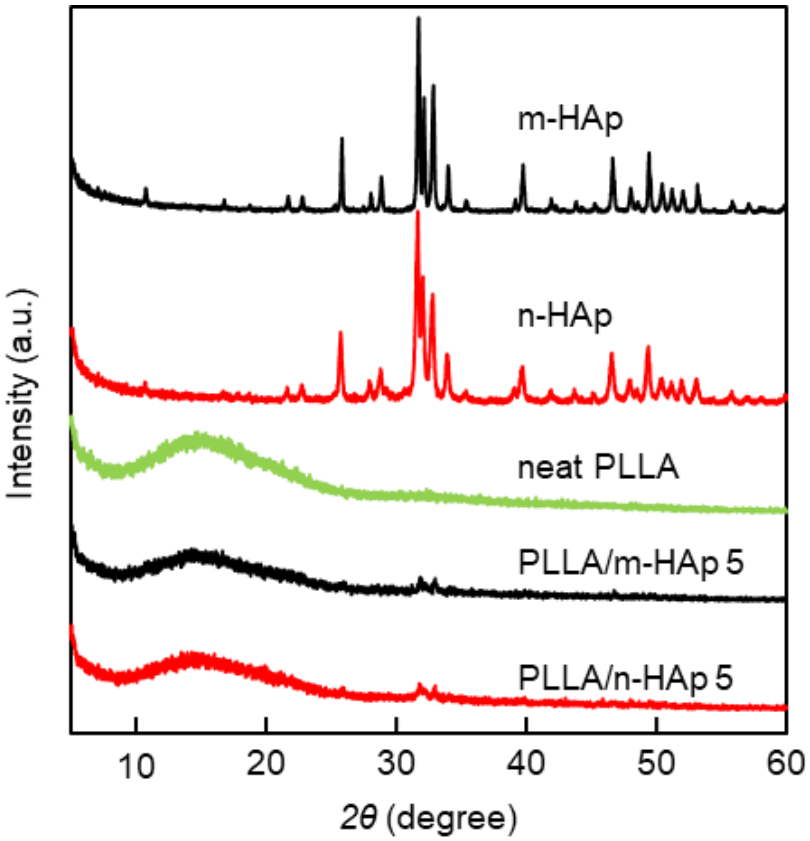

Fig. 2.3 X-ray diffraction profiles of m-HAp filler, n-HAp filler, neat PLLA film, PLLA/m-HAp 5 and PLLA/n-HAp 5 composites.

Figure 2.3 shows the X-ray diffraction profiles of m-HAp, n-HAp, neat PLLA,

PLLA/m-HAp 5, and PLLA/n-HAp 5 composites measured using an X-ray beam with CuKα. In the profiles of neat PLLA, PLLA/n-HAp, and PLLA/m-HAp composites, the amorphous halo of PLLA was observed around 15.0°. In the profiles of m-HAp and n-HAp fillers, the sharp crystalline peaks were identified at 31.9°, 32.2°, 32.8°, and 34.0°, which were assigned to (211), (112), (300) and (202) planes of HAp crystal, respectively.[11,33,34] These peaks were also observed in the profiles of the PLLA/m-HAp 5 and PLLA/n-HAp 5. The peak of the (211) plane at 31.9° with the largest intensity was employed for the stress transfer analyses in the composites using the synchrotron radiation.

2.3.3. Mechanical properties

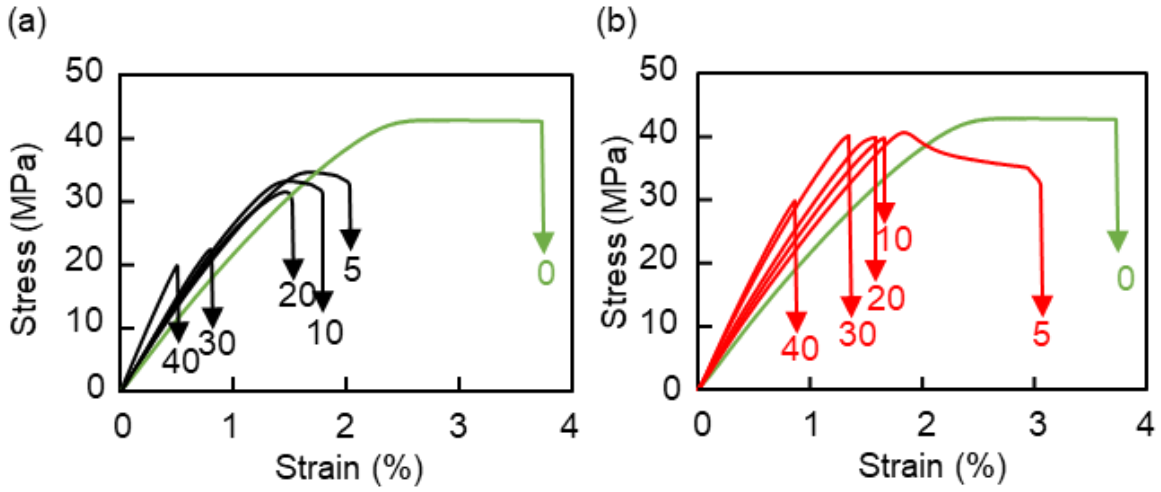

Fig. 2.4 Stress-strain curves of (a) neat PLLA and PLLA/m-HAp composites, (b) neat PLLA and PLLA/n-HAp composites with various HAp contents.

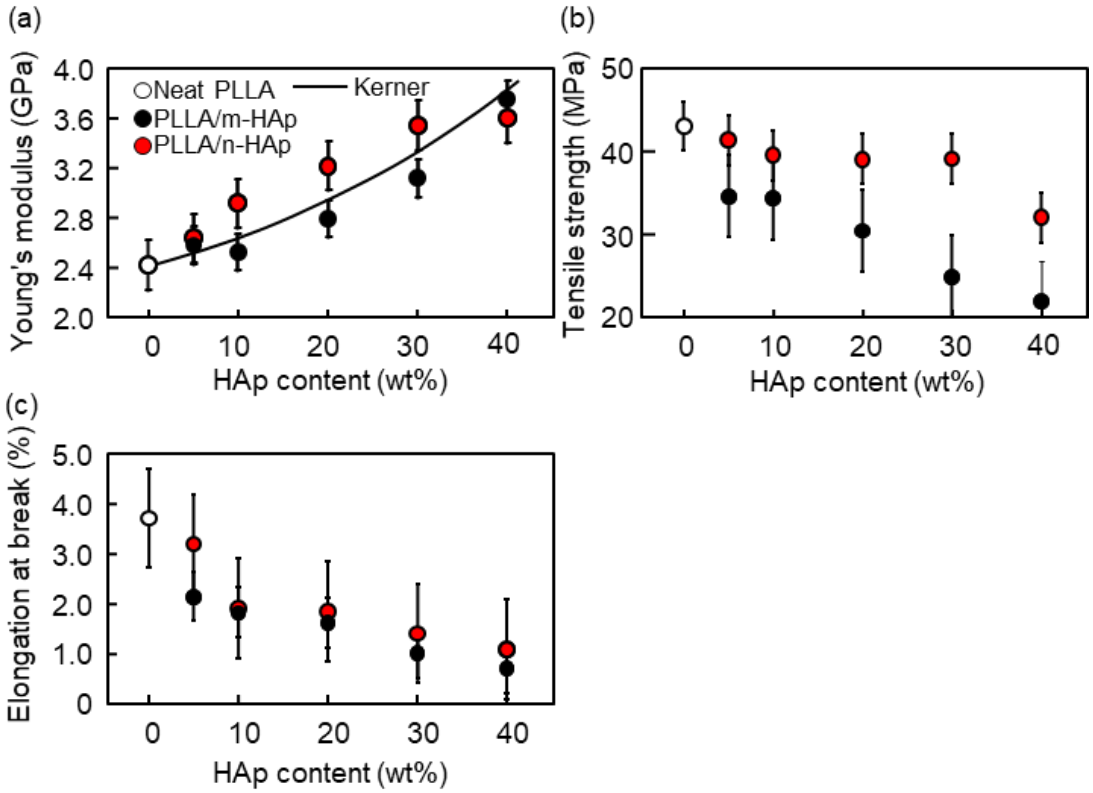

Fig. 2.5 Relationship between the fraction ratios of HAp and (a) Young's modulus, (b) tensile strength, (c) elongation at break of (○) neat PLLA, (●) PLLA/m-HAp and (●) PLLA/n-HAp composites with various HAp contents. The solid line in (a) represents the theoretical fit using Kerner's equation.

Figures 2.4 (a) and (b) show the stress-strain curves of neat PLLA, PLLA/m-HAp, and PLLA/n-HAp composites. Figure 2.5 shows the dependence of Young's modulus (E), tensile strength (σ_{max}), and elongation at break (ε_{max}) on HAp contents (see also in Table 2.2). For the PLLA/m-HAp 30 composites, the σ_{max} was significantly decreased to 25.0 MPa, whereas, for the PLLA/n-HAp composites with 30wt% of n-HAp, the σ_{max} of 39.2 MPa was close to that of the neat PLLA film at 43.1 MPa. In both PLLA/m-HAp and PLLA/n-HAp composites, the E increased with larger amounts of HAp loading. In particular, the Young's modulus E of 3.54 GPa was 46% higher than that of the neat PLLA of 2.42 GPa. In contrast, ε_{max} value decreased sharply with increasing HAp contents. This

result was attributed to the agglomeration of HAp as defects in the composites. Since the agglomeration of HAp enhanced fractures at the interface between the PLLA matrix and HAp fillers, the σ_{max} and ε_{max} values in the composites decreased with larger amounts of HAp loading. For the prediction of Young's modulus of the composites, Young's modulus of the filler and matrix were used with various mechanical models.[33,35–37] Herein, Kerner's equation was employed to estimate the reinforcement effect of particles in composites. The equations (3)-(5) are provided as follows.[38]

$$E = \left[\frac{1+AB\phi_f}{1-B\phi_f}\right] \quad (3)$$

$$A = \frac{7-5\nu_m}{8-10\nu_m} \quad (4)$$

$$B = \frac{\left(\frac{E_f}{E_m}\right)-1}{\left(\frac{E_f}{E_m}\right)+A} \quad (5)$$

where E, E_m, and E_f are the modulus of composites, matrix, and filler, respectively, Φ_f is the volume fraction of the filler, and ν_m is the Poisson's ratio of the matrix. The theoretical E values of the PLLA/HAp composites are calculated using Kerner's equation and are shown as a solid line in Figure 2.5 (a). Relative to values calculated from Kerner's equation, the modulus of PLLA/m-HAp were lower, while those of PLLA/n-HAp were beyond them. In addition, the Young's modulus of the PLLA/n-HAp significantly increased with larger n-HAp content. This enhancement in mechanical properties would arise from the efficient stress transfer between the PLLA matrix and the HAp filler, which improves Young's modulus of the composites.

Table. 2.2 Mechanical properties of neat PLLA, PLLA/m-HAp and PLLA/n-HAp with various HAp contents.

Sample	Mass fraction	Young's modulus	Tensile strength	Elongation at break
	%	GPa	MPa	%
PLLA	0	2.42±0.18	43.1±1.09	3.72±0.60
PLLA/m-HAp 5	5	2.58±0.18	34.7±3.60	2.15±0.04
PLLA/m-HAp 10	10	2.54±0.30	34.4±3.03	1.82±0.07
PLLA/m-HAp 20	20	2.80±0.11	30.5±5.01	1.63±0.18
PLLA/m-HAp 30	30	3.12±0.18	25.0±4.46	1.02±0.12
PLLA/m-HAp 40	40	3.76±0.40	21.9±1.44	0.72±0.08
PLLA/n-HAp 5	5	2.64±0.34	41.5±2.12	3.20±0.68
PLLA/n-HAp 10	10	2.92±0.28	39.6±2.35	1.92±0.07
PLLA/n-HAp 20	20	3.22±0.36	39.1±1.78	1.85±0.11
PLLA/n-HAp 30	30	3.54±0.22	39.2±3.25	1.41±0.11
PLLA/n-HAp 40	40	3.60±0.60	32.1±3.22	1.08±0.02

2.3.4. Thermal properties

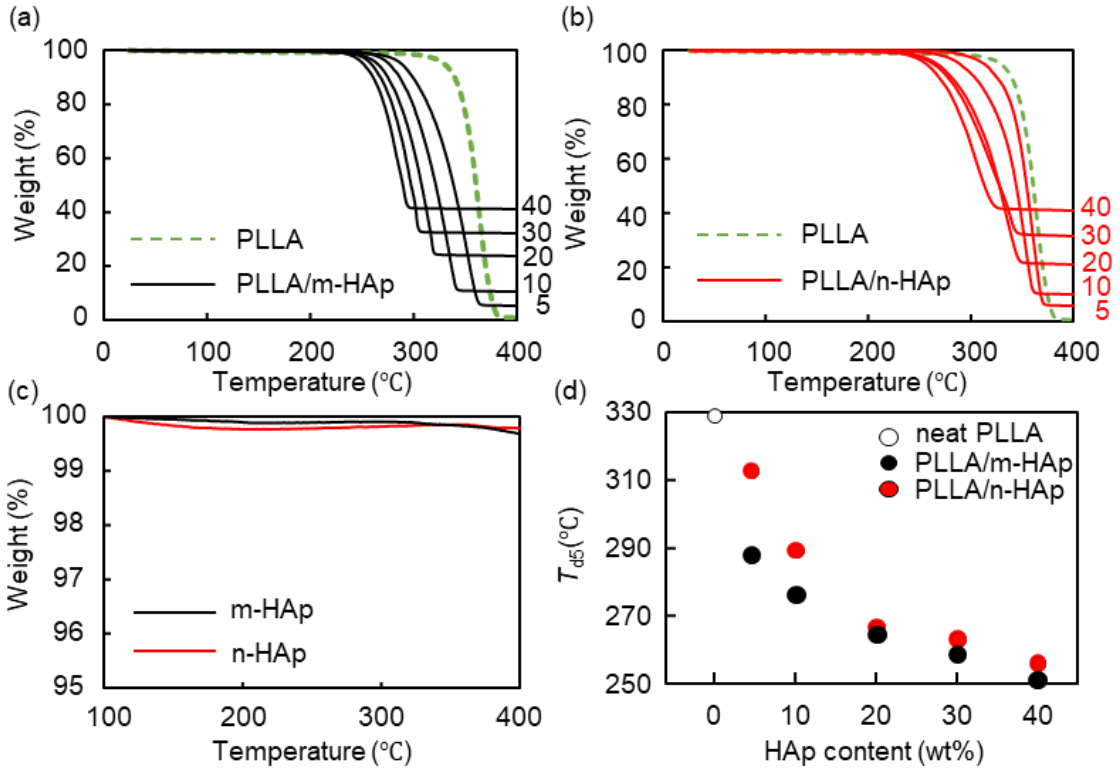

Fig. 2.6 (a) Thermogravimetric curves of PLLA and PLLA/m-HAp composites, (b) PLLA and PLLA/n-HAp composites with various HAp contents, (c) m-HAp and n-HAp fillers. (d) Relationship between thermal decomposition temperature (T_{d5}) and the amount of HAp loading for neat PLLA, PLLA/m-HAp composites, and PLLA/n-HAp composites.

Figure 2.6 shows the thermalgravimetric (TG) curves of (a) neat PLLA and PLLA/m-HAp composites, (b) neat PLLA and PLLA/n-HAp composites, (c) m-HAp and n-HAp fillers, and (d) the relationship between thermal decomposition temperature (T_{d5}) and HAp contents in PLLA/m-HAp, and PLLA/n-HAp composites. From the residual weights at 400 °C under N_2 atmosphere, the weight fractions of the HAp in the composites were measured. Their residual weight coincided with the mixture ratios of HAp fillers in the preparation procedure, as shown in Table 1.1. The slight decreases of the weights of m-HAp and n-HAp fillers above 100°C were observed in both TG curves, which would be

based on absorbed moisture on the HAp fillers. Figure 2.6 (d) shows the relationship between the decomposition temperature (T_{d5}) and the HAp contents in the composites. In the TG curves of the composites, with increasing amounts of loading HAp, T_{d5} of the PLLA/m-HAp and PLLA/n-HAp composites were decreased. Other researchers have also reported on the lower T_{d5} with the increase of loading ratios of filler in other PLLA-based composites. [39–43] These behaviors would be attributed to moisture absorption onto the hydrophilic fillers. The absorbed moisture could impact PLLA's thermal decomposition because this polyester structure was susceptible to hydrolysis. The hydrolysis of PLLA would form oligomers, which exhibited lower thermal stability than neat PLLA.

2.3.5. Stress transfer efficiency

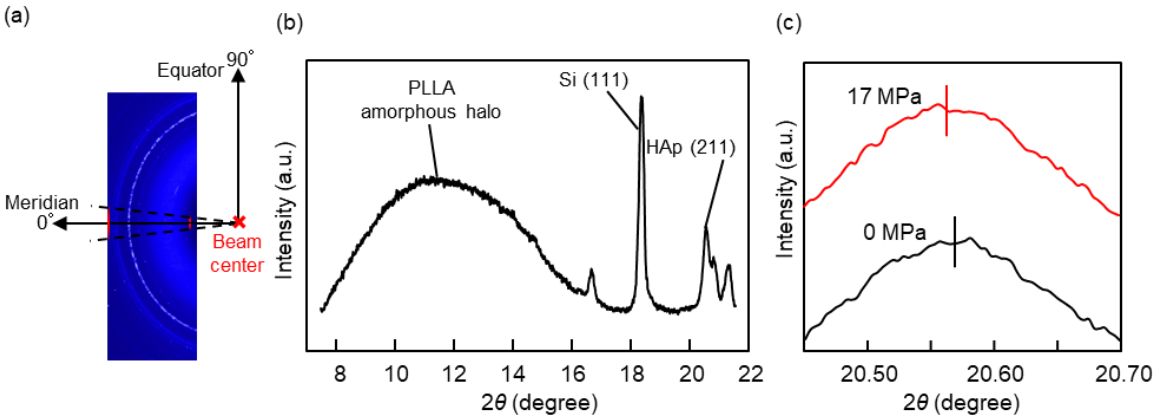

Fig. 2.7 (a) 2D WAXD image of PLLA/n-HAp 5 composite before the stress applied. (b) Its 1D profile obtained from integration within the range from -5° to 5°, and (c) expanded view of 1D WAXD profile of PLLA/n-HAp 5 before and under the applied stress of 17 MPa.

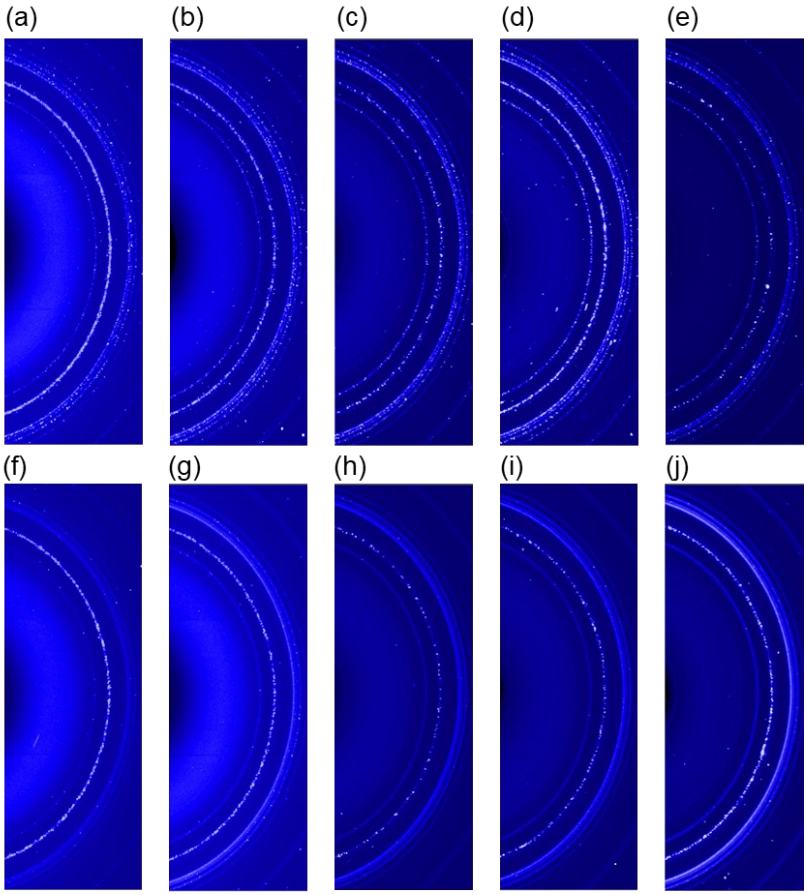

Fig. 2.8 X-ray diffraction images of PLLA/m-HAp (a) 5 (b) 10 (c) 20 (d) 30 and (e) 40, and PLLA/n-HAp (f) 5 (g) 10 (h) 20 (i) 30 and (j) 40 without tensile stress.

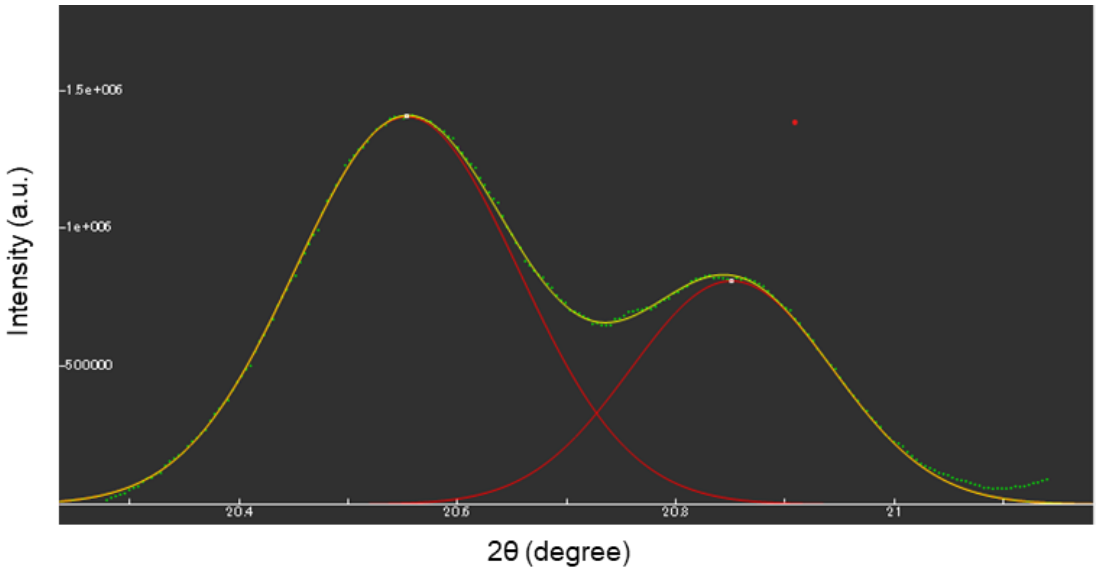

Fig. 2.9 X-ray diffraction profile of PLLA/n-HAp 5 before the stress applied and the red lines represent the Gaussian fitting.

Figure 2.7 (a) shows 2D WAXD image of the PLLA/n-HAp 5 composite without tensile stress using synchrotron radiation. In the 2D WAXD image, the amorphous halo of PLLA and diffraction rings of Si powder and n-HAp fillers were observed. The 2D WAXD images of the PLLA/m-HAp and PLLA/n-HAp composites with various HAp contents before the stress applied were shown in Figure. 2.8. Figure 2.7 (b) shows the meridional 1D WAXD profile obtained from 2D WAXD image in Figure 2.7 (a). In the profiles of PLLA/n-HAp, partial overlap was observed between the diffraction peaks of the (211) and (112) planes of n-HAp at $2\theta = 20.6°$ and 20.8°. For the precise transferred stress analyses, these two peaks were separated to accurately assess the lattice spacing of the (211) plane, as shown in Figure 2.9. By monitoring the lattice spacing of the (211) plane, the strain ε_c of the n-HAp fillers and the transferred stress σ_c were evaluated in the *in situ* X-ray diffraction measurement during tensile tests. Figure 2.7 (c) shows the expended 1D profiles before and under applying 17 MPa stress. Under loading tensile stress, the shift toward the low angle side in the diffraction peak of the (211) plane of n-HAp, which initially observed at $2\theta = 20.6°$, was detected. This shift was ascribed to the expansion of the lattice spacing of the (211) plane of n-HAp filler.

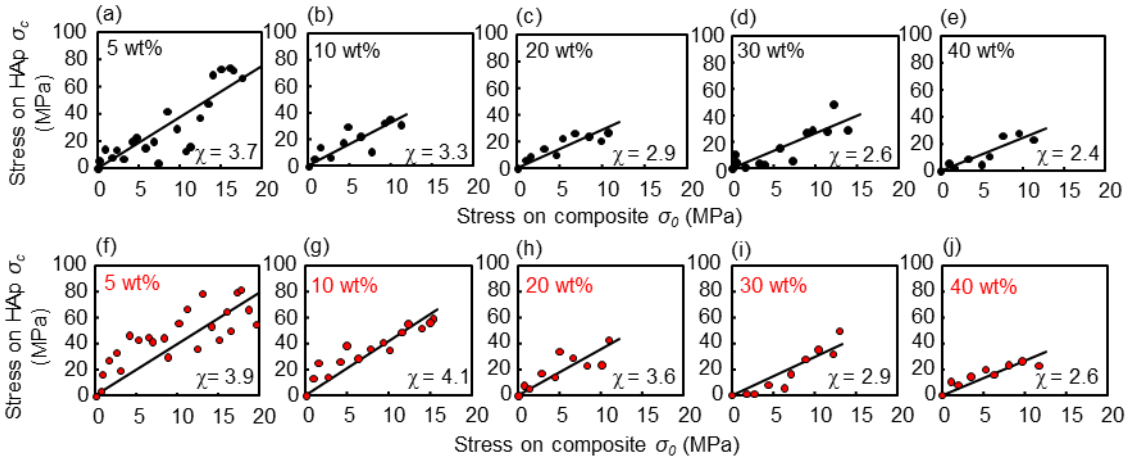

Fig. 2.10 Relationship between the stress applied on composites (σ_0) and the stress (σ_c) on the HAp crystallites, and their stress transfer coefficients χ for the PLLA/m-HAp (a) 5 (b) 10 (c) 20 (d) 30 (e) 40 and PLLA/n-HAp (f) 5 (g) 10 (h) 20 (i) 30 (j) 40.

In Figure 2.10, the relationship between stress σ_0 applied to the composites and stress σ_c transferred to the HAp fillers in PLLA/HAp composites with various HAp contents during the elastic deformation is shown. The inclination of the obtained approximate straight lines to the plots was corresponding to stress transfer coefficients χ. The obtained χ values were larger than 2 in all the composites. This indicates that, in both PLLA/m-HAp and PLLA/n-HAp composites, the applied stress was concentrated on HAp fillers, and the reinforcement effect appeared even in the composites including up to 40% of HAp weight fraction.

Figure 2.11 shows the dependence of the χ values on the filling ratios of HAp. The χ values decreased as the filler fraction increased in both PLLA/m-HAp and PLLA/n-HAp composites. Compared the χ values of composites with m-HAp, the PLLA/n-HAp composites exhibited larger χ values with each fraction ratio of HAp. This suggests that n-HAp fillers provide a superior reinforcement effect on the composites, compared to m-

HAp. The reason would be that the distance between the interfaces of fillers declined with the decrease of particle sizes.[24] Therefore, n-HAp presented effective reinforcement in PLLA/HAp composites rather than m-HAp. Actually, this superior reinforcement effect in PLLA/n-HAp provided larger Young's modulus than those of PLLA/m-HAp composites

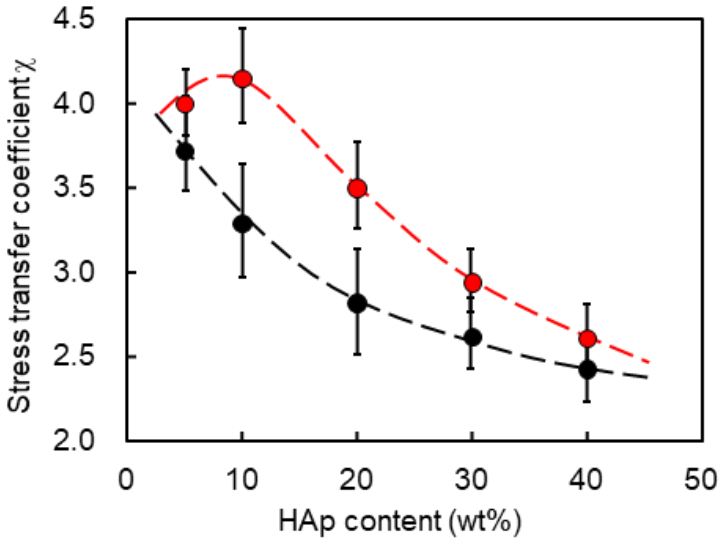

Fig. 2.11 Dependence of the stress transfer coefficient χ on HAp contents of (●) PLLA/m-HAp and (●) PLLA/n-HAp.

2.3.6. *In situ* stress transfer analyses during tensile deformation

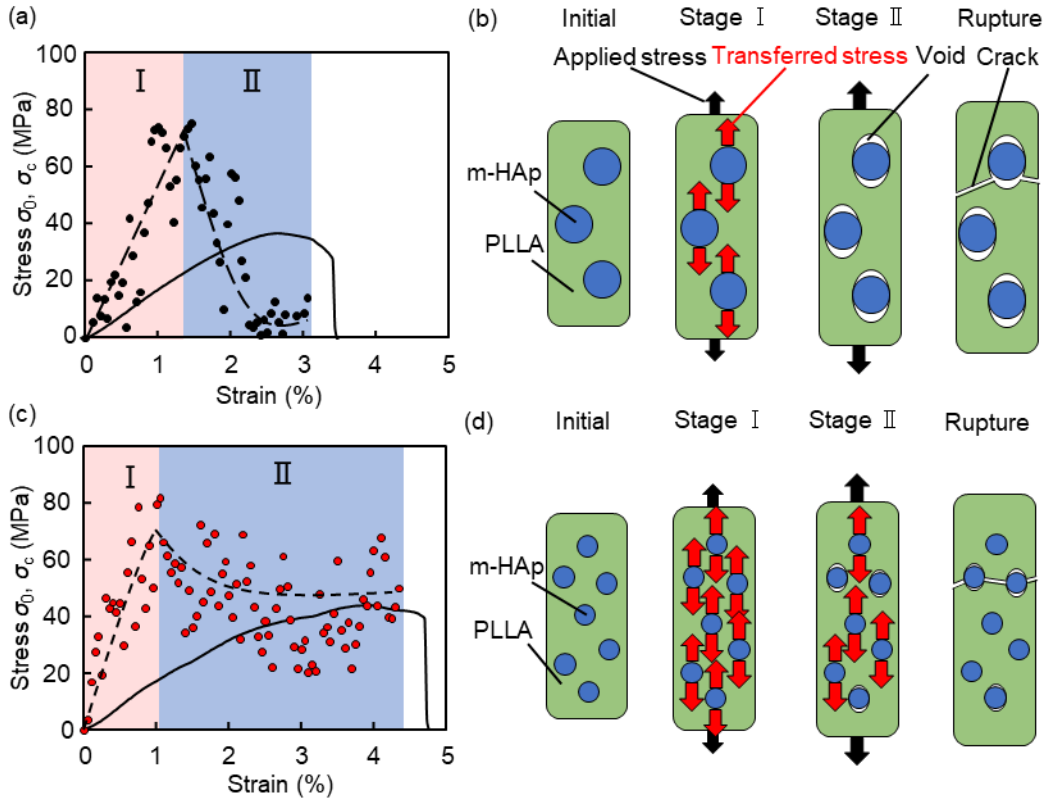

Fig. 2.12 (a) Relationship between σ_c, σ_0, and strain for PLLA/m-HAp 5. (b) Schematic of the stress transfer mechanism of PLLA/m-HAp 5 under deformation. (c) Relationship between σ_c, σ_0, and strain for PLLA/n-HAp 5. (d) Schematic of the stress transfer mechanism of PLLA/n-HAp 5 under deformation. In (a) and (c), circles are the stress σ_c transferred to the HAp fillers under the stress transfer measurement, the black solid line represents the stress σ_0 applied to the whole sample, and black dashed line represents the approximation of the transferred stress σ_c.

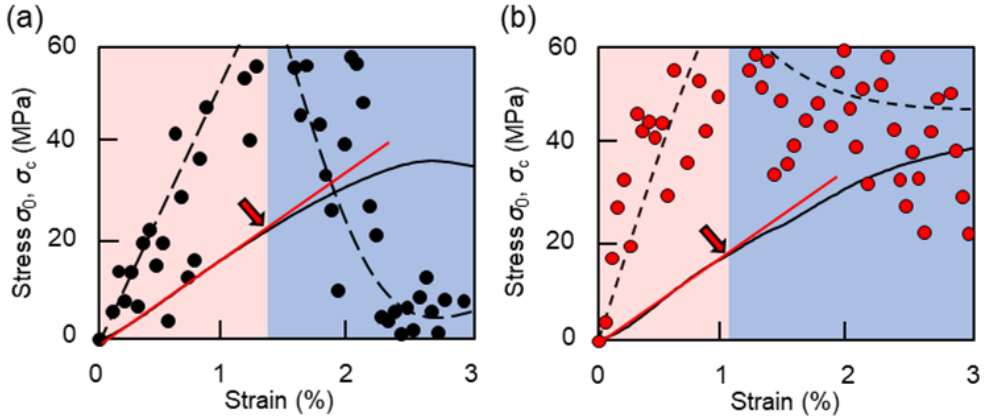

Fig. 2.13 The expanded views of stress-strain curves of (a) PLLA/m-HAp 5 and (b) PLLA/n-HAp 5 composites in the initial deformation region. The red arrow points out the yielding point of the PLLA/HAp

Figure 2.12 (a) shows the relationship between σ_c, σ_0, and strain for PLLA/m-HAp 5 by *in situ* 2D WAXD measurement during tensile tests. The transferred stress σ_c of m-HAp linearly increased with increasing applied strain in the elastic deformation region of the PLLA/m-HAp 5 composite. This elastic deformation region was categorized as stage I and was marked with red in Figure 2.12 (a). In stage I, it is revealed that the transferred stress σ_c was 3.7 times larger than the applied stress σ_0, corresponding to the stress transfer coefficient χ of PLLA/m-HAp 5 composites. After stage I, the σ_c was decreased, and the yielding of the composite was observed. Herein, the yielding was defined as the point where the applied stress was lower than an elastic deformation linear, as shown in Figure 2.13. The rapid decrease of σ_c indicated interfacial debonding between PLLA and m-HAp. We categorized this region as stage II, which was marked with blue in Figure 2.12 (a). This result aligned with the reports by Gent and Bai. [44,45] At the yielding points, the microcrack initiates at the interface of the filler and matrix in the composites. Then, the microcrack spreads quickly along the interface and finally achieves a debonding state. [46] Based on the result of σ_c in PLLA/m-HAp 5, interfacial debonding and microcracks would emerge at a strain of 1.3%. This was corresponding to the yielding point. The accumulation of the microcracks eventually led to the sample rupture at a strain of 3.4%. A schematic representation of this result is shown in Figure 2.12 (b).

Figure 2.14 (c) illustrates the dependence of σ_c and σ_0, on the strain for PLLA/n-HAp 5 composites. The behavior of σ_c in PLLA/n-HAp composite was similar to that in PLLA/m-HAp composites in stage I. The transferred stress σ_c increased linearly with the increasing applied stress σ_0 in stage I and the value of σ_c was 3.9 times larger than that of σ_0. However, in stage II of PLLA/n-HAp 5 composite, a gradual decrease of σ_c was observed and significant transferred stress σ_c persisted until rupture. This suggests that

during stage II, interfacial debonding between PLLA and n-HAp progressed slowly and gradually, and partial interface remained intact until the composite was ruptured. Just before the rupture, the stress σ_c on the n-HAp slightly increased. This reason might be the stress concentration at the crack tips. The deformation scheme of the result of PLLA/n-HAp 5 is shown in Figure 2.12 (d).

The difference in fracture behaviors between PLLA/m-HAp 5 and PLLA/n-HAp 5 composites can be attributed to critical particle size. When the particle radius is below a critical threshold, the interfacial adhesion strength surpasses the tensile strength of the matrix, thereby preventing interfacial debonding.[46] It has been reported the critical size of a sphere particle varies from tens to several hundreds of nanometers. In FE-SEM observations, most of the n-HAp fillers were within this critical size range, while the m-HAp fillers were larger. This observation would account for the divergent behaviors of the PLLA/m-HAp and PLLA/n-HAp composites during stage II. Since the intact interface in the PLLA/n-HAp composites remained intact, the formation of microcracks were reduced during this stage. It is known that mechanical fractures can be caused by the initiation and propagation of cracks.[45] As smaller cracks formed in PLLA/n-HAp 5 than in PLLA/m-HAp 5, the merge of these cracks and expansion into defects were delayed relatively. This would lead to the PLLA/n-HAp 5 composites' higher tensile strength σ_{max} value than PLLA/m-HAp 5, as shown in Figure 2.5. It is supported that the difference in filler size notably affects the fracture mode through interfacial debonding and mechanical properties of the composites.

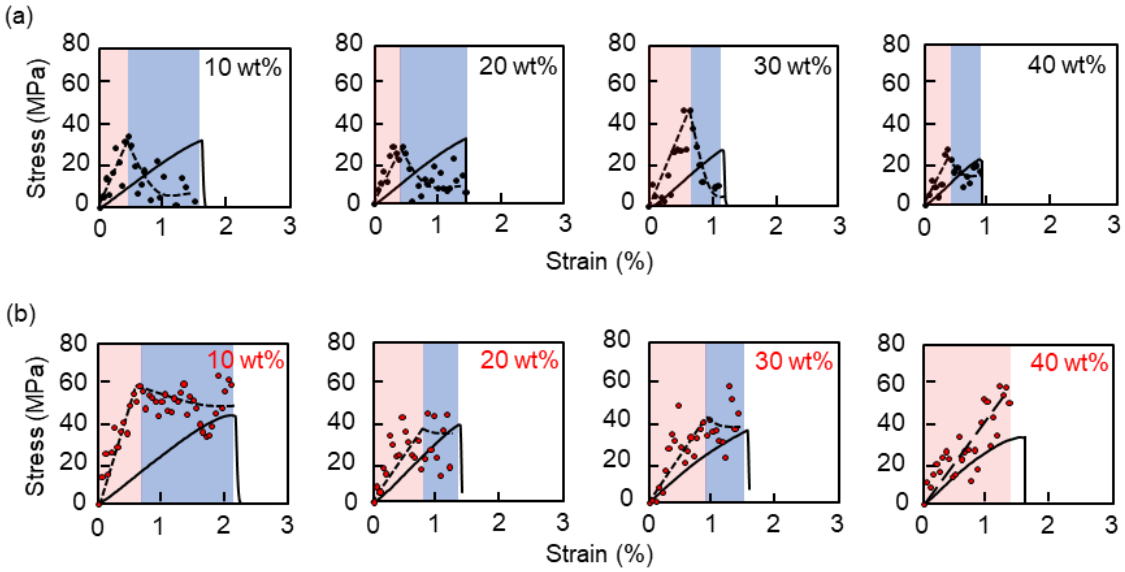

Fig. 2.14 Relationship between σ_c, σ_0, and strain for (a) PLLA/m-HAp 10, 20, 30 and 40, and (b) PLLA/n-HAp 10, 20, 30 and 40.

Figure 2.14 shows the relationship between σ_c, σ_0, and strain for (a) PLLA/m-HAp 10, 20, 30, and 40, and (b) PLLA/n-HAp 10, 20, 30, and 40. As shown in Figure 2.14 (a), linear increase and decrease of σ_c were observed in PLLA/m-HAp with different HAp contents during the stretching in stage I and stage II, respectively. However, the debonding of the PLLA/m-HAp interface initiated at a strain of approximately 0.5%, which were observed at lower strains than that of PLLA/m-HAp 5. Their transferred stress σ_c in all the PLLA/m-HAp composites rapidly decreased in stage II. In contrast, as shown in Figure 2.14 (b), considerable stress remained even in stage II in the PLLA/n-HAp composites. This indicated that partial interfaces in the PLLA/n-HAp composites maintained intact in stage II. Compared with m-HAp, n-HAp fillers would generate smaller voids by interface debonding. The smaller voids prevented to merge into defects, contributing to the higher tensile stress σ_{max}. These results suggested that the stress transfer analyses are promising method for understanding fracture mechanism in composite materials under deformation process.

2.4. Conclusions

Synchrotron radiation X-ray diffraction facilitates the quantification of stress transferred to the fillers in the PLLA/HAp composites. The stress transferred to HAp fillers in PLLA/HAp composites under tensile test was evaluated *in situ* by X-ray diffraction measurement under tensile tests. The stress on fillers was several times larger than the applied stress during the elastic deformation stage. This indicates that the stress was concentrated on the incorporated HAp fillers, leading to mechanical reinforcement in the composite. The stress transfer efficiency in the composites was evaluated with the stress transfer coefficients χ. The χ value of the composites ranged from 2.4 to 3.9, depending on the fillers size and filling ratios. The χ values were increased with the increase of HAp fillers' size and the reduction of the weight fraction of HAp. Furthermore, the interfacial states in the composites were investigated using stress transfer analyses. Variations in HAp filler size significantly impact the fracture behaviors at the composite interface, consequently altering the macroscopic mechanical properties of the composites. These behaviors were attributed to the effect of critical particle size. These results demonstrated that synchrotron X-ray diffraction is a powerful tool for monitoring the stress transfer phenomena as well as the interfacial states in composites under deformation.

2.5. References

1. *Poly(Lactic Acid)*. (Wiley, 2010). doi:10.1002/9780470649848

2. Tsuji, H. in *Poly(Lactic Acid)* 343–381 (Wiley, 2010). doi:10.1002/9780470649848.ch21

3. Mariano, M., Pilate, F., de Oliveira, F. B., Khelifa, F., Dubois, P., Raquez, J.-M. & Dufresne, A. Preparation of Cellulose Nanocrystal-Reinforced Poly(lactic acid) Nanocomposites through Noncovalent Modification with PLLA-Based Surfactants. *ACS Omega* 2, 2678–2688 (2017).

4. Kang, E. Y., Lih, E., Kim, I. H., Joung, Y. K. & Han, D. K. Effects of poly(L-lactide-ε-caprolactone) and magnesium hydroxide additives on physico-mechanical properties and degradation of poly(L-lactic acid). *Biomater Res* 20, 7 (2016).

5. Shen, H., Zhang, L., Liu, M. & Zhang, Z. Biomedical Applications of Graphene. *Theranostics* 2, 283–294 (2012).

6. Yang, K., Feng, L., Hong, H., Cai, W. & Liu, Z. Preparation and functionalization of graphene nanocomposites for biomedical applications. *Nat Protoc* 8, 2392–2403 (2013).

7. Marques, P. A. A. P., Gonçalves, G., Singh, M. K. & Grácio, J. Graphene Oxide and Hydroxyapatite as Fillers of Polylactic Acid Nanocomposites: Preparation and Characterization. *J Nanosci Nanotechnol* 12, 6686–6692 (2012).

8. Sydlik, S. A., Jhunjhunwala, S., Webber, M. J., Anderson, D. G. & Langer, R. *In Vivo* Compatibility of Graphene Oxide with Differing Oxidation States. *ACS Nano*

9, 3866–3874 (2015).

9. Mohd Pu'ad, N. A. S., Abdul Haq, R. H., Mohd Noh, H., Abdullah, H. Z., Idris, M. I. & Lee, T. C. Synthesis method of hydroxyapatite: A review. *Mater Today Proc* 29, 233–239 (2020).

10. Hassan, M. N., Mahmoud, M. M., El-Fattah, A. A. & Kandil, S. Microwave-assisted preparation of Nano-hydroxyapatite for bone substitutes. *Ceram Int* 42, 3725–3744 (2016).

11. Bordea, I. R., Candrea, S., Alexescu, G. T., Bran, S., Băciuț, M., Băciuț, G., Lucaciu, O., Dinu, C. M. & Todea, D. A. Nano-hydroxyapatite use in dentistry: a systematic review. *Drug Metab Rev* 52, 319–332 (2020).

12. Capuana, E., Lopresti, F., Ceraulo, M. & La Carrubba, V. Poly-l-Lactic Acid (PLLA)-Based Biomaterials for Regenerative Medicine: A Review on Processing and Applications. *Polymers (Basel)* 14, 1153 (2022).

13. Zhao, M. L., Sui, G., Deng, X. L., Lu, J. G., Ryu, S. K. & Yang, X. P. PLLA/HA Electrospin Hybrid Nanofiber Scaffolds: Morphology, In Vitro Degradation and Cell Culture Potential. *Adv Mat Res* 11–12, 243–246 (2006).

14. Kryszak, B., Biernat, M., Tymowicz-Grzyb, P., Junka, A., Brożyna, M., Worek, M., Dzienny, P., Antończak, A. & Szustakiewicz, K. The effect of extrusion and injection molding on physical, chemical, and biological properties of PLLA/HAp whiskers composites. *Polymer (Guildf)* 287, 126428 (2023).

15. Gay, S., Arostegui, S. & Lemaitre, J. Preparation and characterization of dense nanohydroxyapatite/PLLA composites. *Mater Sci Eng C* 29, 172–177 (2009).

16. Charles, L. F., Kramer, E. R., Shaw, M. T., Olson, J. R. & Wei, M. Self-reinforced composites of hydroxyapatite-coated PLLA fibers: Fabrication and mechanical characterization. *J Mech Behav Biomed Mater* 17, 269–277 (2013).

17. Stepak, B. D., Antończak, A. J. & Szustakiewicz, K. Optimization of femtosecond laser micromachining of polylactide and PLLA/HAp composite. in *Laser-based Micro- and Nanoprocessing XII* (eds. Klotzbach, U., Washio, K. & Kling, R.) 70 (SPIE, 2018). doi:10.1117/12.2296433

18. Khan, M. A., Hussain, Z., Liaqat, U., Liaqat, M. A. & Zahoor, M. Preparation of PBS/PLLA/HAP Composites by the Solution Casting Method: Mechanical Properties and Biocompatibility. *Nanomaterials* 10, 1778 (2020).

19. Peng, W., Zheng, W., Shi, K., Wang, W., Shao, Y. & Zhang, D. An *in vivo* evaluation of PLLA/PLLA-gHA nano-composite for internal fixation of mandibular bone fractures. *Biomed. Mater.* 10, 065007 (2015).

20. Koyanagi, J., Ogihara, S., Nakatani, H., Okabe, T. & Yoneyama, S. Mechanical properties of fiber/matrix interface in polymer matrix composites. *Adv. Compos. Mater.* 23, 551–570 (2014).

21. Duan, H., Wang, J. & Huang, Z. Micromechanics of composites with interface effects. *Acta Mechanica Sinica* 38, 222025 (2022).

22. Chung, D. D. L. Interface engineering for cement-matrix composites. *Compos. Interfaces* 8, 67–81 (2000).

23. Mukhopadhyay, S., Deopura, B. L. & Alagiruswamy, R. Interface Behavior in Polypropylene Composites. *J. Thermoplast. Compos. Mater.* 16, 479–495 (2003).

24. Xu, A.-R., Nishino, T. & Nakamae, K. Stress transmission in silica particulate epoxy composite by X-ray diffraction. *Polymer (Guildf)* 33, 5167–5172 (1992).

25. Nishino, T., Naito, H., Nakamura, K. & Nakamae, K. X-ray diffraction studies on the stress transfer of transversely loaded carbon fibre reinforced composite. *Compos Part A Appl Sci Manuf* 31, 1225–1230 (2000).

26. Nishino, T., Hirao, K. & Kotera, M. X-ray diffraction studies on stress transfer of kenaf reinforced poly(l-lactic acid) composite. *Compos Part A Appl Sci Manuf* 37, 2269–2273 (2006).

27. Morimune, S., Kotera, M. & Nishino, T. Stress Transfer of Poly (VinylAlcohol) / Montmorillonite Nano composite Using X-ray Diffraction. *Journal of The Adhesion Society of Japan* 46, 320–324 (2010).

28. Matsumoto, T., Mori, S., Ohashi, T., He, C. & Nishino, T. Stress-transfer analyses in cellulose nanofiber/montmorillonite nanocomposites with X-ray diffraction and chemical interaction between cellulose nanofiber and montmorillonite. *Cellulose* 29, 2949–2960 (2022).

29. Hatsui, T. & Graafsma, H. X-ray imaging detectors for synchrotron and XFEL sources. *IUCrJ* 2, 371–383 (2015).

30. Hashimoto, R., Igarashi, N., Kumai, R., Takagi, H., Kishimoto, S., Kudo, T. & Hatsui, T. in 263–266 (2018). doi:10.1007/978-981-13-1316-5_49

31. Hatsui, T. Developments of X-ray Imaging Detectors at SACLA/SPring-8: Current Status and Future Outlook. *Synchrotron Radiat News* 27, 20–23 (2014).

32. Tan, S. K. The determination of the elastic constants of apatites by thermal diffuse

X-ray scattering. *Diss. Abstr. Int., B, Sci. Eng.* 34, 2862 (1973).

33. Gupta, A., Prasad, A., Mulchandani, N., Shah, M., Ravi Sankar, M., Kumar, S. & Katiyar, V. Multifunctional Nanohydroxyapatite-Promoted Toughened High-Molecular-Weight Stereocomplex Poly(lactic acid)-Based Bionanocomposite for Both 3D-Printed Orthopedic Implants and High-Temperature Engineering Applications. *ACS Omega* 2, 4039–4052 (2017).

34. Venkatesan, J. & Kim, S.-K. Nano-Hydroxyapatite Composite Biomaterials for Bone Tissue Engineering—A Review. *J Biomed Nanotechnol* 10, 3124–3140 (2014).

35. Halpin, J. C. Stiffness and Expansion Estimates for Oriented Short Fiber Composites. *J Compos Mater* 3, 732–734 (1969).

36. Affdl, J. C. H. & Kardos, J. L. The Halpin-Tsai equations: A review. *Polym Eng Sci* 16, 344–352 (1976).

37. Guth, E. Theory of Filler Reinforcement. *J Appl Phys* 16, 20–25 (1945).

38. Kerner, E. H. The Elastic and Thermo-elastic Properties of Composite Media. *Proc. Phys. Soc. B* 69, 808–813 (1956).

39. Yiga, V. A., Lubwama, M. & Olupot, P. W. Thermal stability of NaOH modified rice husk fiber-reinforced polylactic acid composites: Effect of rice husks and clay loading. *Results in Materials* 18, 100398 (2023).

40. Han, S. O., Karevan, M., Sim, I. N., Bhuiyan, M. A., Jang, Y. H., Ghaffar, J. & Kalaitzidou, K. Understanding the Reinforcing Mechanisms in Kenaf Fiber/PLA and Kenaf Fiber/PP Composites: A Comparative Study. *Int J Polym Sci* 2012, 1–8

(2012).

41. Yu, T., Jiang, N. & Li, Y. Study on short ramie fiber/poly(lactic acid) composites compatibilized by maleic anhydride. *Compos Part A Appl Sci Manuf* 64, 139–146 (2014).

42. Hu, G., Cai, S., Zhou, Y., Zhang, N. & Ren, J. Enhanced mechanical and thermal properties of poly (lactic acid)/bamboo fiber composites via surface modification. *J Reinf Plast Comp* 37, 841–852 (2018).

43. Zhu, Z., Wu, H., Ye, C. & Fu, W. Enhancement on Mechanical and Thermal Properties of PLA Biocomposites Due to the Addition of Hybrid Sisal Fibers. *J. Nat. Fibers* 14, 875–886 (2017).

44. Gent, A. N. Detachment of an elastic matrix from a rigid spherical inclusion. *J Mater Sci* 15, 2884–2888 (1980).

45. Bai, S.-L., Wang, M. & Zhao, X.-F. Interfacial debonding behavior of a rigid particle-filled polymer composite. *Compos Interfaces* 10, 243–253 (2003).

46. Chen, J., Wang, G.-T., Yu, Z.-Z., Huang, Z. & Mai, Y.-W. Critical particle size for interfacial debonding in polymer/nanoparticle composites. *Compos Sci Technol* 70, 861–872 (2010).

CHAPTER III

Preparation of Isotactic Polypropylene/ Coffee Silverskin Composites

3.1 Introduction

Coffee is one of the most widely consumed beverages worldwide.[1] According to the Food and Agriculture Organization of the United Nations' research, global green coffee bean consumption of green coffee beans reached approximately 10 million tons in 2023.[2] Drinkable coffee is obtained from the raw coffee cherry through sorting, cleaning, pulping, fermenting, washing, drying, roasting, cooling, grinding, and brewing.[3] In the roasting process, roasted brown coffee beans and coffee silverskin (CS), are produced. The amounts of CS is corresponding to approximately 0.75wt% in a coffee cherry, or 4.2wt% in a green coffee bean.[4] After the roasting process of coffee, the obtained CS is always discarded as a waste. The utilization of the wasted CS contributes to the development of sustainable green materials and the reduction of wastes.[5,6] CS takes advantage of its low moisture content and non-perishable characteristics compared to other by-products of the coffee industry, such as coffee pulp and spent coffee grounds. These characteristics enhance the use of CS in the engineering applications. CS is employed as fillers in composites. Actually, considerable efforts have been devoted to the fabrication of CS-filled composites.[7,8] Sisti *et al*. investigated the UV durability of poly-*L*-lactide (PLLA)/CS and poly(butylene succinate) (PBS)/CS composites. The incorporation of CS fillers enhanced the stability of the composites against UV irradiation because of the antioxidative property of CS.[9] Ghazvini *et al.* investigated the effects of CS loading on the properties of PLLA/PBS/CS three-component composites. They reported that Young's modulus and hydrophilicity were increased significantly with the addition of CS fillers.[10] Sarashi *et al.* used CS to reinforce poly(butylene adipate-co-terephthalate)/poly(3-hydroxybutyrate-co-3-hydroxyvalerate) blend, improving the stiffness and tensile strength of the composites.[11] Hejna *et al.* fabricated high-density

polyethylene/CS composites and revealed the increase of the thermo-oxidative resistance of the composites with CS.[12] Zarrinbakhsh *et al*. prepared the PP/CS composites filled with 25wt% of CS. The increase in their tensile, bending modulus, and impact-toughness were observed.[13] In these studies, it has been reported that CS behaved as a nuclear agent and enhanced the crystallization of different polymer matrices. However, the weight fractions of CS in all these composites were restricted to 30wt% to exhibit efficient mechanical reinforcement due to their insufficient interfacial interaction between CS and polymer matrices. In their reports, there is a room to improve the interfacial interaction between the CS and polymer matrix for more excellent mechanical properties of the composites.

CS is lignocellulose with high hydrophilicity, composed of 30wt% lignin, 24wt% cellulose, 17wt% hemicellulose, 19wt% protein, 3wt% fat, and 7wt% ash.[7] This hydrophilic property of CS provided inferior interaction with the hydrophobic polymer matrix and aggregation of CS filler in the composites, resulting in low mechanical modulus and strength. Several approaches have been suggested to increase interfacial interaction between CS fillers and polymer matrices, including the surface modification of the CS fillers and the post-functionalization of the polymer matrices. Dominisi *et al*. modified the CS surface by esterification with palmitoyl chloride. They combined CS fillers with bio-based polyethylene, and the resulting composites' tensile strength was increased with the treatment compared with untreated composites.[14] Ochoa *et al.* investigated the effects of the NaOH-treated CS on the properties of polyester-resin based composites. The tensile strength of the composites with NaOH-treated CS was increased by 36%, compared to the untreated composites.[15] Moreover, adding compatibilizers is also a practical approach to increasing the filler and matrix affinity.[16] Herein, we

focused on PP/CS composites using m-PP as a compatibilizer to increase the interfacial interaction between the CS filler and the PP matrix. Maleic anhydride-modified polypropylene (m-PP) is one of the most significant PP-based commercial compatibilizers, owing to its unique combination of the low cost, high reactivity of the succinic anhydride moieties, and excellent processability.[17] In the m-PP, the hydrophilic maleic anhydride groups were grafted on the hydrophobic PP backbone, leading to the amphiphilicity of this modified polymer. The m-PP was widely accepted for fabricating composites with PP and natural fillers.[18,19]

In this study, the PP/CS composites and PP/CS composites with a trace amount of m-PP added (noted as m-PP/CS) were fabricated using melt-kneading and hot-press. The effects of the addition of m-PP and the ratios of CS fillers on the mechanical and thermal properties of PP/CS and m-PP/CS composites were investigated. The relationships between these composites' morphologies and mechanical properties were also clarified with X-ray computed tomography and X-ray diffraction.

3.2. Experimental

3.2.1. Materials

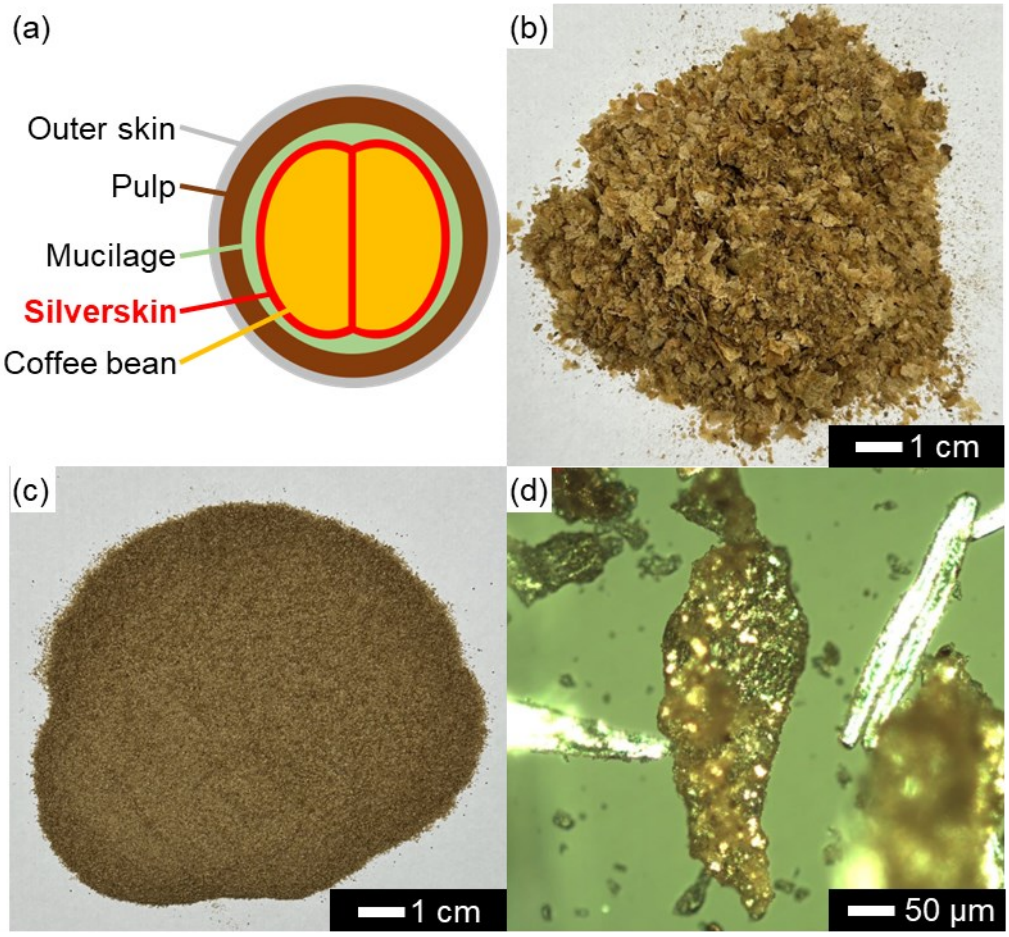

Fig. 3.1 (a) Structure of the coffee cherry. Optical images of (b) CS flakes and (c) CS powder after sieving. (d) Optical microscopic image of CS powder after sieving.

PP (J105G) was purchased from the Prime Polymer Co., Ltd.. m-PP (UMEX 1010) with a modification rate of 3.7 mol% and weight averaged molecular weight M_w of 30k was kindly supplied by Sanyo Chemical Industries Ltd. CS flakes were obtained after the roasting process of coffee beans. CS serves as the thin skin covering the surface of the coffee bean in the coffee cherry, as shown in Figure 3.1 (a).

3.2.2. Sample preparation

3 g of CS flakes were crushed with a rotary mill (GS-4671, TWINBIRD, Japan) at 28000 rpm for 70 seconds and then sieved through a 300 μm sieve to obtain CS powder. Figure 1 shows the optical images of (b) CS flakes and (c) CS powder after sieving and (d) microscopic image of CS powder after sieving. In Figure 3.1 (d), the CS filler with approximate dimensions of 300 μm in length and 100 μm in width was observed. The observation was conducted using a polarized light microscope (Nikon Corp., ECLIPSE LV100N POL) with a 40x objective lens (Nikon Corp., Plan Fluor 40x). CS powder was dried at 100 ℃ for 6 h before the melt-kneading. PP, m-PP, and CS were placed in a twin-screw kneader (Labo Plastomill 50C150, Toyo Seiki Seisaku-sho Ltd, Tokyo, Japan) for melt-kneading. The total weight of PP and CS was 30 g, and the CS loadings were 20, 40, 60, 70, and 80wt% to the total weight. The amount of m-PP was set to 0.05 times the weight of CS filler. The PP, m-PP, and CS were preheated at 180 °C for 3 min, the kneading was performed for 5 min at 180 ℃ with a rotational rate of 100 rpm. The obtained mixture was subsequently hot-pressed at 180 ℃, 1 MPa, using a hot-pressing machine (Gonno Hydraulic Machinery Mfg. Co., Ltd.), followed by quenching into the ice water to fabricate the m-PP/CS composites. The m-PP/CS composites contained PP, CS, and m-PP. In contrast, the PP/CS composites and PP film without m-PP were also prepared as references. The slow-cooling PP films were prepared without the quenching process. The constitution of the m-PP/CS and the PP/CS composites are shown in Table 3.1. Before the following measurement, the samples were dried under a vacuum at 40 ℃ for 24 h. The thickness of the prepared samples was around 200 μm.

Table. 3.1 Constitution of PP, PP/CS, and m-PP/CS composites.

Sample	PP content	CS content	m-PP content
	%	%	phr
PP	100	0	0.0
PP/CS 20	80	20	0.0
PP/CS 40	60	40	0.0
PP/CS 60	40	60	0.0
PP/CS 70	30	70	0.0
PP/CS 80	20	80	0.0
m-PP/CS 20	80	20	1.0
m-PP/CS 40	60	40	2.0
m-PP/CS 60	40	60	3.0
m-PP/CS 70	30	70	3.5
m-PP/CS 80	20	80	4.0

3.2.3. Thermogravimetry (TG)

Thermal degradation behaviors of PP, PP/CS, m-PP/CS, and CS were evaluated using a thermogravimetry (Thermo plus EVO II TG8121, Rigaku Co., Japan) with 5 mg of sample weight. The thermogravimetric measurements were performed under a nitrogen atmosphere at a heating rate of 10 °C/min from 100 °C to 500 °C using Al pans. The thermal decomposition temperatures (T_{d5}) of the samples were obtained from their thermograms. T_{d5} was defined as a temperature of 5% thermal weight loss. The TG measurements were performed using more than 3 individual samples. The actual CS contents in composites were calculated from the residual weight fraction of at 500 °C in

TG curves using eq. 1.

$$W_{Cact} = W_C/W_F \qquad (1)$$

where the W_{Cact} was the actual CS contents in the composites and the W_C and W_F were the weight residual fraction of the composites and CS fillers at 500 °C obtained from the TG curves, respectively.

3.2.4. Differential scanning calorimetry (DSC)

The crystallization behaviors of PP, PP/CS, and m-PP/CS composites were examined using a differential scanning calorimeter (Rigaku Co., DSC 8230) with 5 mg of sample weight in Al pans. The DSC measurements were performed under a nitrogen atmosphere. The samples were heated from 25 °C to 200 °C at a rate of 10 °C/min, held at 200 °C for 5 min, and subsequently cooled to 25 °C at a rate of 10 °C/min to measure the crystallization temperatures and behaviors of the samples during the cooling process. The crystallization temperature was defined as the peak top of the exothermic peak during cooling.

3.2.5. Tensile test

The mechanical properties of PP, PP/CS, and m-PP/CS composites were measured with a tensile tester (Autograph, AGS-1kND, Shimadzu Co. Ltd.) with 1.0 mm/min of cross-head speed. The samples were trimmed into rectangles with 30 mm of length, 5 mm of width, and 0.2 mm of thickness. The initial length of the sample was 20 mm, and the tensile rate was 1.0 mm/min. The tensile tests were performed using more than 8 individual samples and their mechanical parameters were calculated as the averages of

the obtained values. The cross-section areas of the samples were measured from the width and thickness of the samples.

3.2.6. Thermomechanical analysis (TMA)

The linear thermal expansion behaviors of the PP, PP/CS, and m-PP/CS composites were performed using a Thermo Plus EVOII TMA8310 (Rigaku Co.) under a nitrogen gas atmosphere. The nitrogen flow rate was 70 mL/min, the heating rate was 10 °C/min, and the scanning range was from 30 °C to 100 °C. The samples were trimmed into rectangles with 20 mm of length and 2 mm of width. The initial length was 20 mm, and the loading tensile stress was 0.1 MPa. The dimensional stabilities were evaluated from the thermal expansion behaviors of the samples, and linear thermal expansion coefficients (α) were calculated from the thermal expansion ratios of the composites from 30 to 100 °C.

3.2.7. X-ray computed tomography (X-ray CT)

The structure and dispersity of CS fillers in both PP/CS 60 and m-PP/CS 60 composites were examined by X-ray CT measurements with a nano3DX instrument (Rigaku Co.). The X-ray beam was generated at 40 kV and 30 mA, with a wavelength of 1.5418 Å (CuKα). A CCD camera with a resolution of 0.27 μm/pixel and a field of view of 0.6 mm × 0.9 mm was used. The PP/CS and m-PP/CS composite samples were trimmed into a thickness of 200 μm. The exposure time was 10 seconds per image, binning was set to 2, the sample was rotated 180°, and 500 CT images were captured per measurement. The structures of the composites in both the in-plane and thickness directions were analyzed using the sliced tomographic images.

3.2.8. Measurements of X-ray diffraction profiles

X-ray diffraction profiles of PP, PP/CS, m-PP/CS, and CS powder were measured using an X-ray diffractometer (SmartLab 3kW, Rigaku Corporation). An X-ray beam of CuKα tube with 1.5418Å of the wavelength was generated with a tube voltage of 40 kV and tube current of 30 mA. The scanning speed was 50°/min, the sampling step was 0.004°, and the scanning range of 2θ was from 5 to 80°.

3.2.9. Measurements of X-ray diffraction photographs

The orientation of CS fillers in PP/CS and m-PP/CS composites with varying CS contents were investigated with the measurements of 2D X-ray diffraction patterns. The measurements were performed at SPring-8 BL03XU. The photographs of slow-cooling PP films were also measured for reference. The synchrotron radiation's vertical and horizontal beam size was 50 μm and 150 μm, respectively, and the X-ray wavelength was 0.06 nm with 20.7 KeV of photon energy. The diffraction photographs were recorded with a PILATUS3 1M detector with a pixel size of 172 μm×172 μm and a detection area of 16.9 mm × 17.9 mm. The camera length was 265 mm. An aluminum attenuator with a thickness of 200 μm was chosen to control the intensity of the incident beam. The exposure time was 0.8 sec for each sample, and the silicon powder was used as a standard. The degree of orientation π of CS fillers in the composites was calculated from the equation $\pi = (180°\text{-}H)/180°$ with the 004 reflection of cellulose I_β of CS fillers. H is a half-width of the intensity distribution curve for 004 reflection along the Debye-Scherrer ring.

3.3. Results and Discussion

3.3.1. Optical images

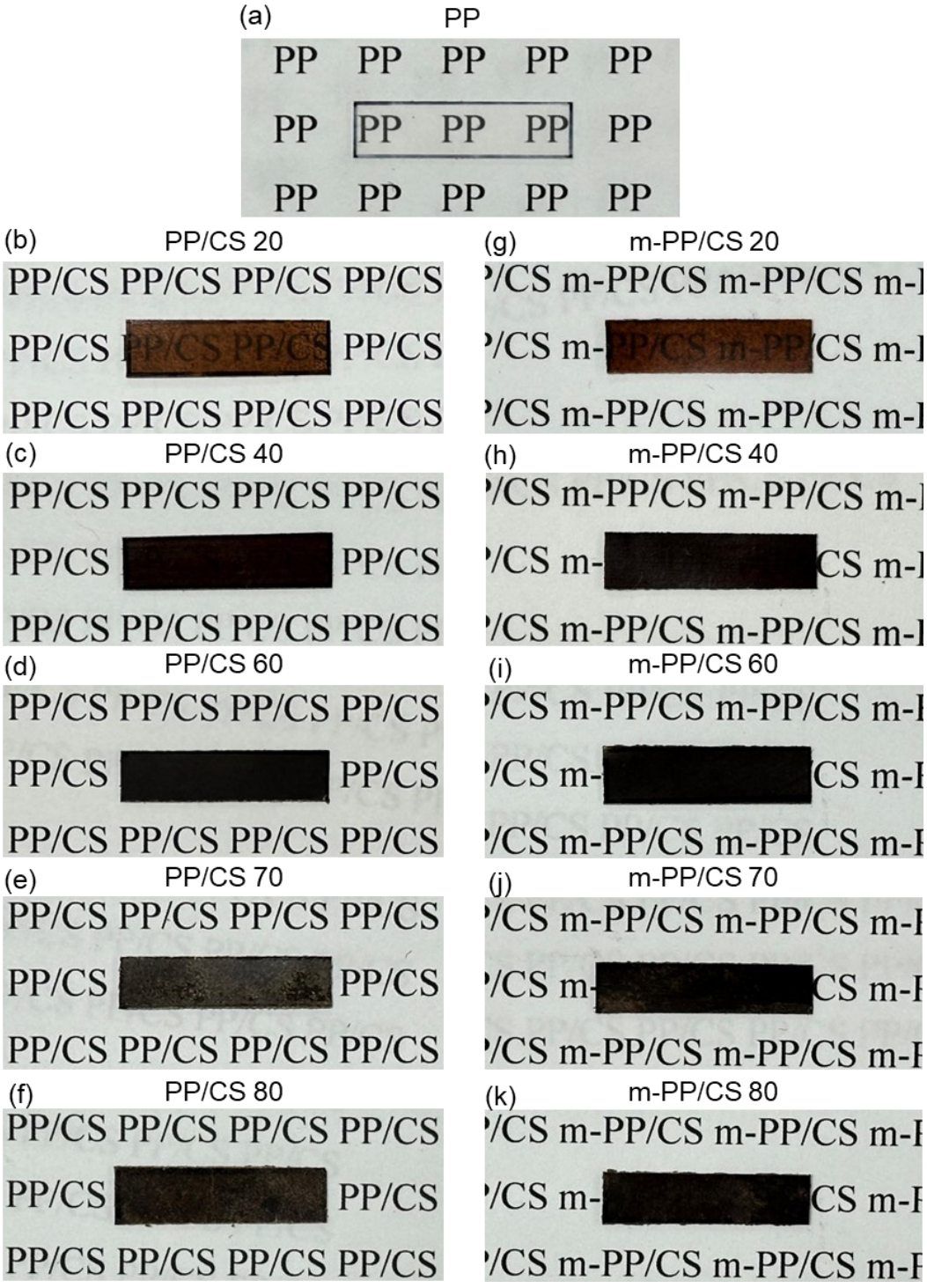

Fig. 3.2 Optical images of PP, PP/CS, and m-PP composites with various CS contents. The sizes of the samples in the images were 20 mm in length and 5 mm in width.

Figure 3.2 shows the optical images of PP, PP/CS, and m-PP/CS composites with CS contents of 20, 40, 60, 70, and 80wt%. The neat PP film was transparent, and the smooth surface was observed as shown in Figure 3.2 (a). In Figure 3.2 (b), the brownish translucent PP/CS 20 composite was observed. When the CS contents exceeded 40wt%, the PP/CS composites became opaque as shown in Figures 3.2 (c), (d), and (f). Moreover, PP/CS 70 and 80 showed the rough surfaces in Figures 3.2 (d) and (f). This would be attributed to the excessive addition and aggregation of CS fillers. For the m-PP/CS composites with m-PP contained, similar phenomena to the PP/CS composites such as the translucent m-PP/CS 20 and the opaque m-PP/CS 40, 60, 70, and 80 were observed, as shown in Figures 3.2 (g), (h), (i), (j), and (k). However, in the m-PP/CS composites with high CS contents (70 and 80wt%), smooth surfaces were observed. This reason would be the improved interfacial interaction between the PP matrix and CS fillers.

3.3.2. Thermal properties

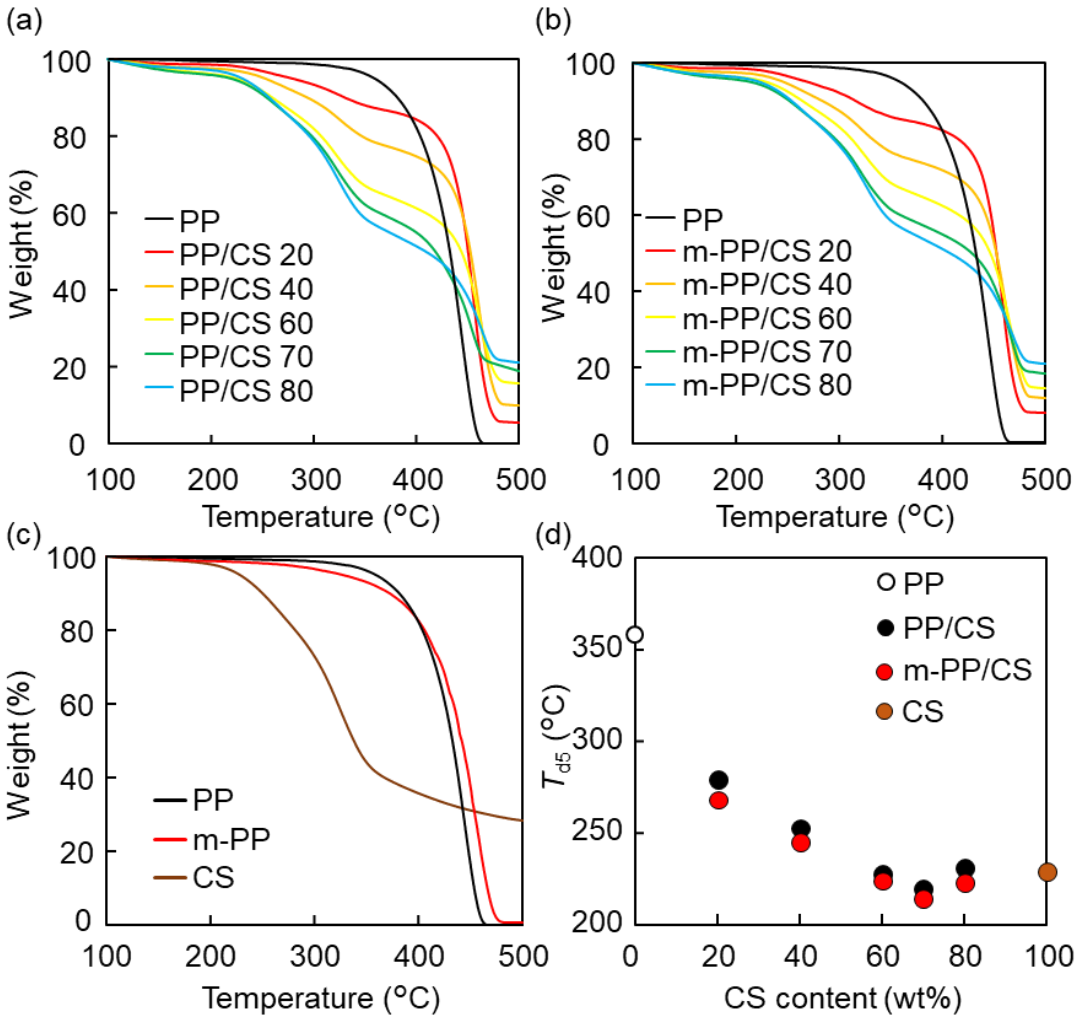

Fig. 3.3 TG curves of (a) PP and PP/CS composites, (b) PP and m-PP/CS composites, (c) PP, m-PP and CS powder. (d) T_{d5} of PP, PP/CS, m-PP/CS, and CS powder after sieving.

Figure 3.3 shows the thermogravimetric analysis (TG) curves of (a) PP, PP/CS composites, (b) PP, m-PP/CS composites with various CS contents, and (c) PP, m-PP, and CS powder. The thermal decomposition behaviors of the composites corresponded to the sums of those of PP and CS. In addition, the residual weights of both PP/CS and m-PP/CS composites at 500 °C were larger as the weight fractions of CS in their composites were increased. The PP and m-PP were degraded abruptly and completely decomposed at

500 °C, whereas the CS powder retained 28wt% as residues. In the TG curve of CS powder, its thermal decomposition behavior was divided into two patterns. In the first decomposition behavior from 200 °C to 340 °C, the thermal degradation of the CS progressed fast, and the large weight loss was observed. The first decomposition would be attributed to the rapid ones of hemicellulose and cellulose in CS.[20] The second one occurred above 340 °C. The second weight loss would be attributed to the decomposition of the lignin and proteins in CS powder.[21] These results indicate that the thermal stability of CS resembles those of the conventional lignocelluloses, which decomposition temperature is observed at approximately 215 ± 10 °C.[22] Figure 3.3 (d) shows the correlation between T_{d5} of PP, composites, and their CS contents. A significant decrease in T_{d5} was observed with the increasing CS contents from 0wt% to 80wt%. The reason for these decreases was the incorporation of thermally unstable CS fillers. In the composites with 60wt%, 70wt%, and 80wt% of CS contents, the T_{d5} of the composites was much lower than that of PP and approached that of CS. In addition, the T_{d5} of m-PP/CS composites was slightly lower than those of PP/CS, which would result from the m-PP added with lower $T_{d5.}$ In m-PP/CS 60 composites, T_{d5} was decreased by 130.2 °C, compared to that of PP. Table 3.2 shows T_{d5}, residual weights, and fraction ratios of PP/CS and m-PP/CS composites with varying CS contents. The actual CS contents in the composites were calculated from the residual weight at 500 °C under N_2 gas. The actual CS contents calculated from the residual weight almost corresponded to those in the preparation recipe.

Table. 3.2 Decomposition temperature T_{d5}, residual weights, theoretical CS contents, and actual CS contents of CS in PP, m-PP, CS, PP/CS, and m-PP/CS composites with various CS loading.

Sample	T_{d5}	Residual weight	Theoretical CS content	Actual CS content[a]
	°C	%	wt%	wt%
PP	359	<1	0	0
m-PP	327	<1	0	0
CS	228	28	100	100
PP/CS 20	279	6	20	19
PP/CS 40	252	10	40	35
PP/CS 60	228	16	60	55
PP/CS 70	219	19	70	67
PP/CS 80	230	21	80	74
m-PP/CS 20	269	7	20	25
m-PP/CS 40	245	11	39	41
m-PP/CS 60	224	15	58	55
m-PP/CS 70	213	18	68	65
m-PP/CS 80	222	20	77	73

[a] calculated from the residual weight of the composites using the residual weight fraction of CS filler.

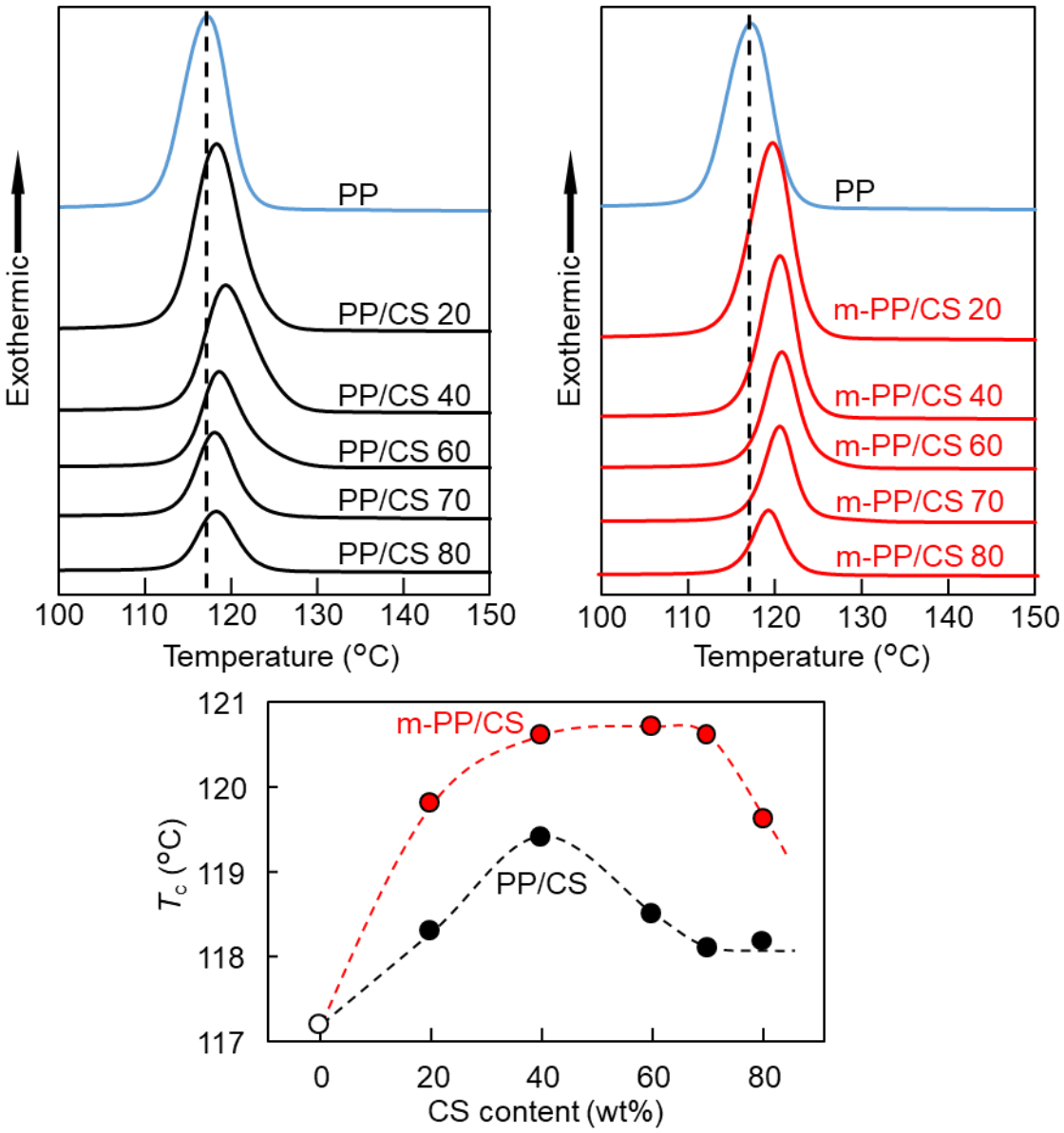

Fig. 3.4 DSC cooling curves of (a) PP and PP/CS composites, (b) PP, and m-PP/CS composites. (c) Dependence of crystallization temperature on the CS contents of PP, PP/CS, m-PP/CS composites.

Figure 3.4 shows the DSC curves in cooling process of (a) PP, PP/CS composites and (b) m-PP/CS composites. In the DSC curves of PP and composites, the exothermic crystallization peaks were observed at around 119 °C. In Figure 3.4 (a), the exothermic peak of PP shifted to the higher temperature side with the increase of CS fraction,

indicating that CS acted as a nucleating agent, and promoted the crystallization of PP during the cooling process. This behavior of CS filler as a nucleating agent has been reported in other composites.[11,12,21,23,24] The formation of crystal nucleation occurred at the PP/CS interface. The smaller PP crystallites were grown around CS fillers during crystallization. In the composites with 70 and 80wt% of CS contents, the exothermic peak shifted to the lower temperature side relative to those with 40 and 60wt% of CS, suggesting the decrease of CS's nucleating effect. This reason may be that the PP matrix was posed in the narrow region between CS fillers in the composites with the excessive CS addition, which restricted the mobility of PP chains in the matrix and hindered the crystallization.[25–28] This suppressed crystallization was observed as the shift of the exothermic peak to the lower temperature side in the composites with 70 and 80wt% of CS contents. The crystallization behaviors in m-PP/CS composites were corresponded to those of PP/CS composites. The higher crystallization temperatures T_c were observed in the m-PP/CS composites with larger amounts of CS, following that the crystallization temperature of that with 80wt% of CS content was decreased. In the m-PP/CS composites, loading excessive CS fillers also obstructed the growth of crystalline regions, leading to the decrease of nucleating effects. Figure 3.4 (c) shows the correlation between CS contents and the T_c of PP/CS, and m-PP/CS composites. All the m-PP/CS composites exhibited higher T_c than the PP/CS composites. The addition of m-PP as a compatibilizer would improve the interaction between the CS filler and the PP matrix, allowing the enhancements of the nucleation around CS fillers.[29]

3.3.3. Mechanical properties

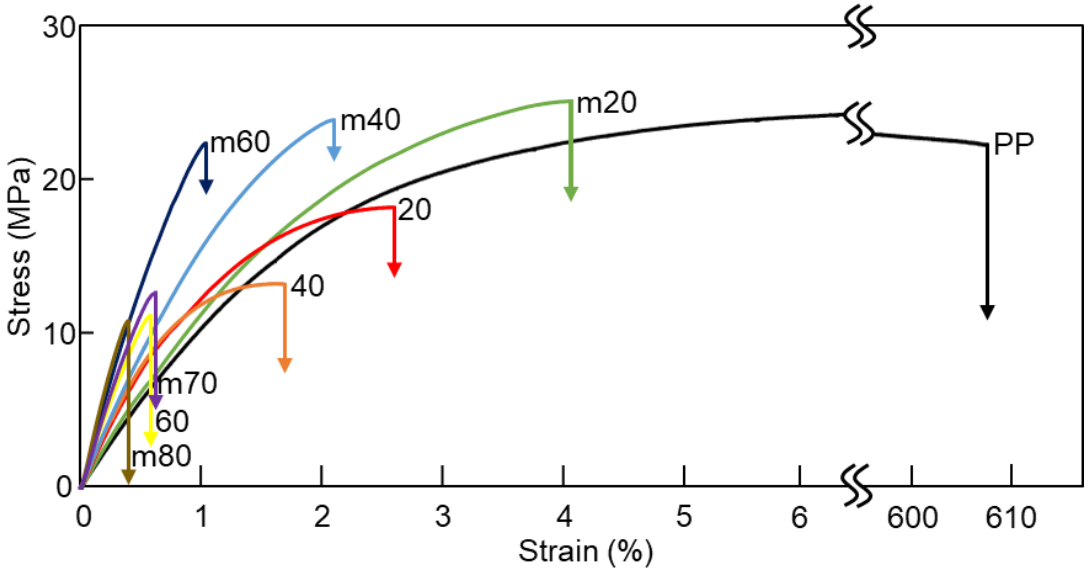

Fig. 3.5 Stress-strain curves of PP, PP/CS, and m-PP/CS composites with various CS contents. The texts near the curves represent the sample name. For example, m20 represents m-PP/CS 20, and 20 represents PP/CS 20 composites.

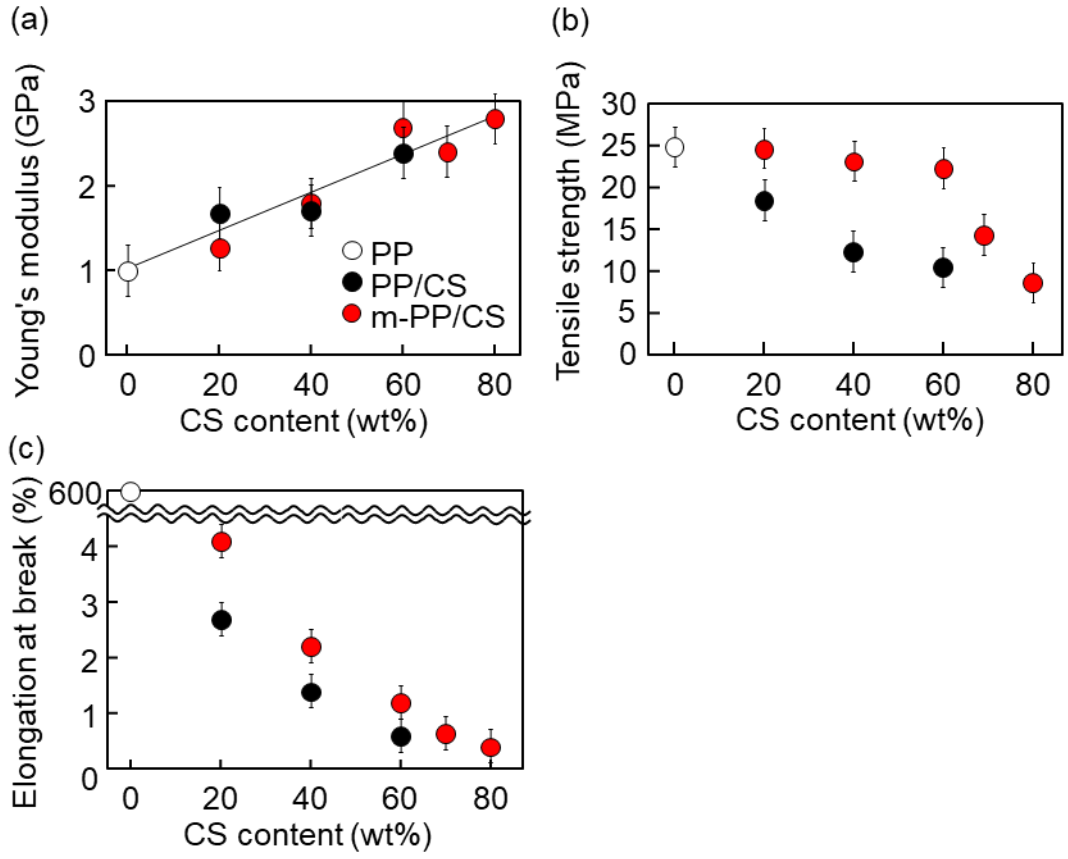

Fig. 3.6 Dependence of Young's modulus, tensile strength, and elongation at break on CS contents of PP, PP/CS, and m-PP/CS composites with various CS contents.

At high CS loading (70 and 80wt%), the PP/CS composites without m-PP showed rough surfaces and became excessively brittle, making the tensile test a challenge. This indicated the adverse interfacial interaction between the hydrophilic CS and hydrophobic PP. Conversely, for the m-PP/CS composites containing m-PP, those with 70 and 80wt% CS contents exhibited sufficient strength for tensile testing.

Figure 3.5 shows the stress-strain curves of PP, PP/CS, and m-PP/CS composites, and Figure 3.6 summarizes the dependence of mechanical parameters on the CS contents in PP, PP/CS, and m-PP/CS composites obtained from their stress-strain curves (see also Table 3.3). In both the composites with and without the compatibilizer addition, their Young's modulus were increased with the increase of CS filler. These were attributed to the enhancement of crystallization of the PP matrix and reinforcement effects of CS fillers. The tensile strength of PP/CS composites were decreased with the larger amounts of CS fillers, while those of m-PP/CS composites with less than 60wt% of CS fillers maintained larger values but the abrupt decrease in the composites with larger CS amounts was observed. In addition, m-PP increased the tensile strength of the m-PP/CS composites, compared with those of PP/CS composites. These increase in their tensile strength was attributed to the increase of the interfacial interaction between the CS fillers and the PP matrix, through the amphiphilic property of m-PP. Moreover, both the elongation at break of PP/CS and m-PP/CS composites were declined as the CS contents were increased. However, the elongation at break of m-PP/CS composites were larger than those of PP/CS composites. This reason would be also the enhancement of the interfacial interaction with the m-PP compatibilizer. It was worth noting that Young's modulus of m-PP/CS 60 composite was increased by 162%, with only 10% of reduction in tensile strength, compared with those of neat PP. Furthermore, the tensile strength of m-PP/CS 60 was

117% larger than that of PP/CS 60 composite without m-PP. These results reveal that the m-PP is an effective compatibilizer in the fabrication of PP/CS composites including even larger amount of CS fillers to improve mechanical properties.

Table. 3.3 Mechanical properties of neat PP, PP/CS, and m-PP/CS composites with various CS contents.

Sample	Young's modulus	Tensile strength	Elongation at break
	GPa	MPa	%
PP	1.0±0.1	24.9±1.0	604.1 ± 24.2
PP/CS 20	1.6±0.2	18.8±1.2	2.7 ± 0.4
PP/CS 40	1.6±0.1	12.3±2.4	1.4 ± 0.3
PP/CS 60	2.3±0.3	10.3±2.4	0.6 ± 0.2
PP/CS 70			
PP/CS 80			
m-PP/CS 20	1.3±0.2	24.7±2.2	4.1 ± 0.4
m-PP/CS 40	1.8±0.1	23.2±1.5	2.2 ± 0.3
m-PP/CS 60	2.7±0.4	22.4±5.3	1.2 ± 0.3
m-PP/CS 70	2.5±0.3	14.9±3.2	0.6 ± 0.2
m-PP/CS 80	2.8±0.6	8.7±3.2	0.4 ± 0.2

3.3.3. Linear coefficients of thermal expansion

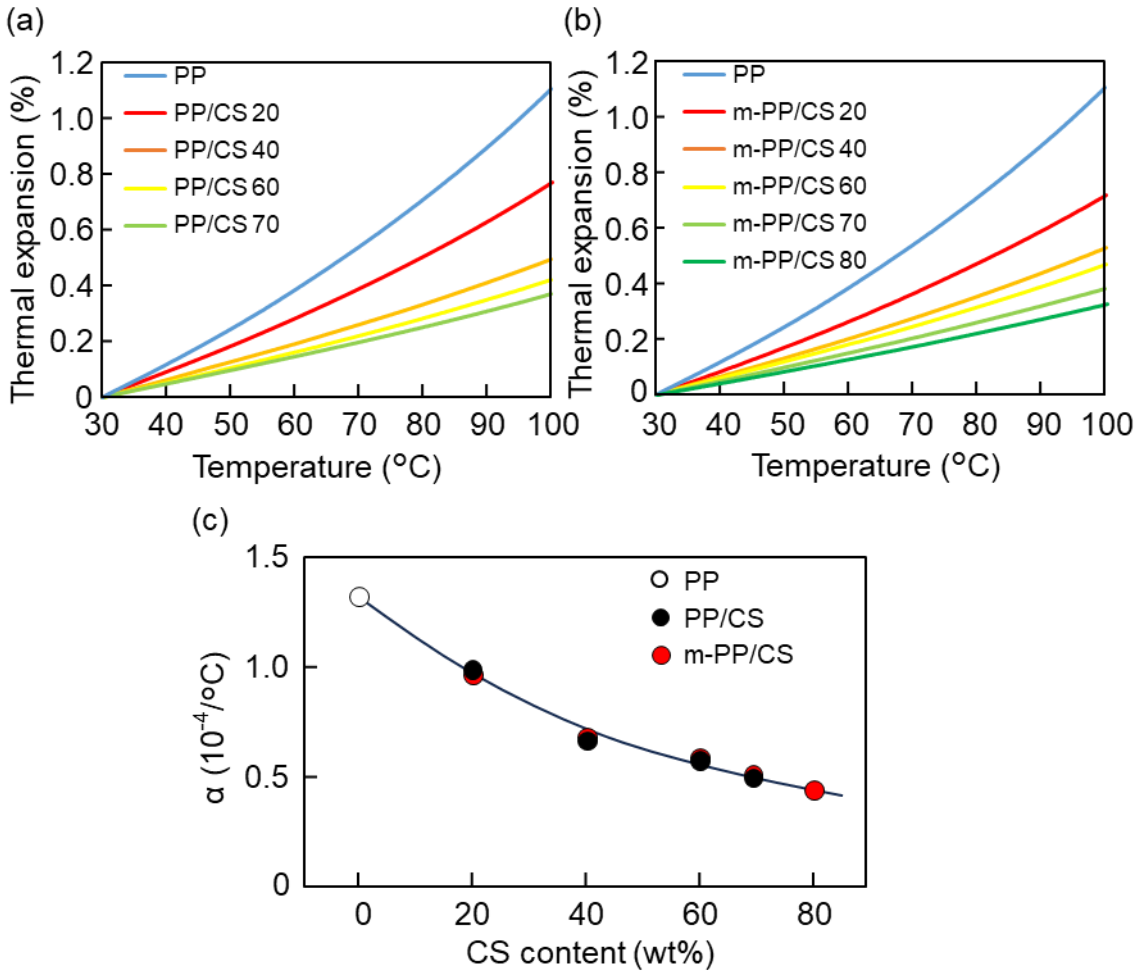

Fig. 3.7 Thermal expansion behaviors of (a) PP and PP/CS composites with various CS contents and (b) PP and m-PP/CS composites with various CS contents. (c) Linear coefficients of thermal expansion (α) of PP, PP/CS, and m-PP/CS composites with various CS contents.

Similar to the tensile test, the PP/CS composites without m-PP became brittle at a high CS content of 80wt%, making TMA measurement challenging. In contrast, the m-PP/CS composites containing m-PP exhibited sufficient strength for measurement even at 80wt% of CS content.

Figures 3.7 (a) and (b) show the thermal expansion behaviors of PP, PP/CS, and m-PP/CS composites. The incorporation of CS fillers suppressed the thermal expansion of

the PP matrix in the composites because the cellulose, hemicellulose, and lignin in the CS fillers possessed extremely small thermal expansion coefficients. Between −30 and 30 °C, the thermal expansion coefficients for various celluloses and hemicelluloses ranged from 5.1 to 6.0×10^{-4} ml./g./°C, and for lignin, the coefficient was about 10×10^{-5} ml./g./°C based on the works of Ramiah *et al.*. [30] Hirano *et al.* reported the anisotropic linear thermal expansion behavior of transparent cellulose nanopaper using TMA measurement with compression mode. The linear coefficient of thermal expansion (α) value of the cellulose nanopaper in the out-of-plane direction was measured to be 0.460×10^{-4}/°C within the temperature range of 25–100°C, which is approximately five times higher than its in-plane α value of 0.08×10^{-4}/°C with the same temperature range.[31] In Figure 3.7 (c), the relationship between the α and CS contents is shown (see also in Table 3.4), and α of composites was decreased sharply with the increase of CS contents. The PP/CS and m-PP/CS with the same CS contents show similar α, indicating that the addition of m-PP affected composites' thermal expansion behaviors very slightly. For the m-PP/CS 60 composite, α value was decreased by 55% compared to PP. Besides, m-PP/CS 80 composite with the highest CS contents possessed the lowest value, which was 67% lower than neat PP.

Table. 3.4 Linear coefficients of thermal expansion (α) of PP, PP/CS, and m-PP/CS composites with various CS contents.

Sample	α
	10^{-4}/°C
PP	1.323
PP/CS 20	0.997
PP/CS 40	0.679
PP/CS 60	0.556
PP/CS 70	0.502
PP/CS 80	
m-PP/CS 20	0.969
m-PP/CS 40	0.686
m-PP/CS 60	0.593
m-PP/CS 70	0.523
m-PP/CS 80	0.442

3.3.5. X-ray CT images

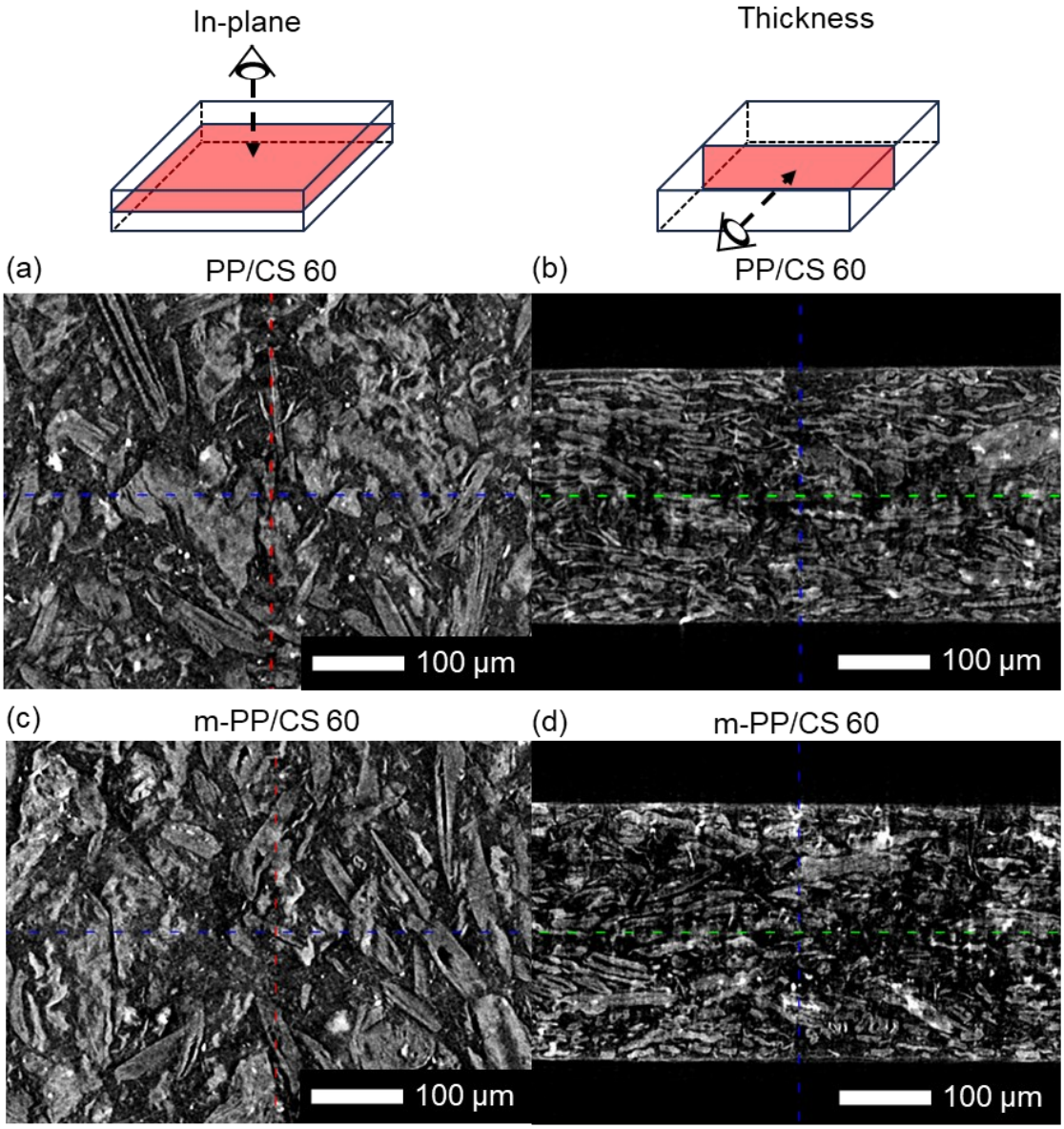

Fig. 3.8 X-ray CT cross-sectional images of PP/CS 60 composite with (a) in-plane and (b) thickness direction. X-ray CT cross-sectional images of m-PP/CS 60 composite with (c) in-plane and (d) thickness direction.

Figure 3.8 shows the cross-sectional images of PP/CS 60 and m-PP/CS 60 composites with in-plane and thickness direction by X-ray CT measurement. In the images, the brighter areas with higher density correspond to CS fillers, while the darker areas with

lower density represent the PP matrix. In Figures 3.8 (a), (b), (c), (d), the plate-like CS fillers were observed in the composites. The sizes of the CS fillers were 100 μm in length, 20 μm in width, and 5 μm in thickness, approximately. Furthermore, CS was distributed homogeneously in both PP/CS 60 and m-PP/CS 60 composites by melt-kneading. No agglomeration of CS fillers in the PP/CS 60 and m-PP/CS 60 composites was observed. The direct reason for the increase of 117% in the tensile strength of m-PP/CS 60 composites compared to the PP/CS 60 would be the improvement of the interfacial interaction with the addition of m-PP, but not the difference in their morphology. Additionally, in Figure 3.8 (b), the CS fillers in both PP/CS and m-PP/CS composites were oriented along the in-plane direction for the hot-pressing process. This orientation of CS fillers along the surface of the composites would lead to a further increase of their Young's modulus, relative to that of neat PP.

3.3.5. X-ray diffraction profiles

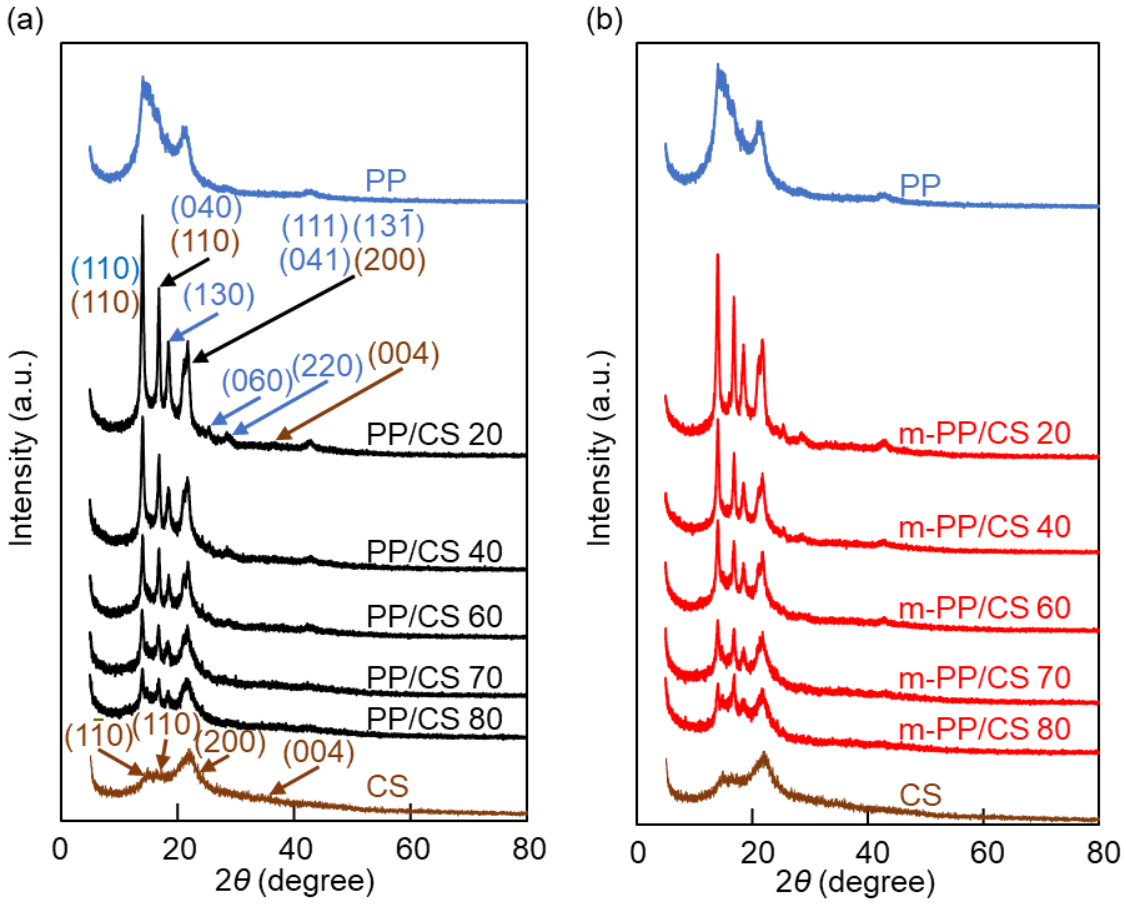

Fig. 3.9 (a) XRD profiles of (a) PP, CS powder, and PP/CS composites with various CS contents and (b) PP, CS powder, and m-PP/CS composites with various CS contents. The blue, brown, and black arrows indicate the diffraction peaks assigned to PP α-form, cellulose Iβ-form in CS, and their overlap, respectively.

Figure 3.9 shows the XRD profiles of (a) PP, CS powder, and PP/CS composites with different CS contents and (b) PP, CS powder, and m-PP/CS composites with various CS contents. In the XRD profiles of PP after quenching, the reflections of the smectic phase and weak diffraction peaks of the PP α-form were observed.[32,33] In the X-ray diffraction profiles of CS powder, the diffraction peak were observed at 14.7°, 16.1°, 22.5°, and 35.0°, which were assigned to $1\bar{1}0$, 110, 200, and 004 planes of cellulose Iβ-

form, respectively.[34] The crystallinity of cellulose I_β-form of CS was calculated as 31% from the X-ray diffraction profile of CS powder using Segal's method.[35] In the profiles of PP/CS and m-PP/CS composites with various CS contents, the strong peaks of 110, 040, 130, 111, 041, and 220 planes of the PP α-form were observed[33], suggesting that CS enhanced the crystallization of PP as a nucleating agent in the composites during the quenching process. These results were consistent with ones of DSC.[36] Moreover, this crystallization of the PP matrix in the composites would be the reason for the increase in their Young's modulus. Unfortunately, because the diffraction peaks of PP and CS completely overlapped, the quantitative assessment of the crystallinity of the PP matrix in their composites has been inaccessible from the X-ray diffraction profiles.

3.3.5. X-ray diffraction photographs

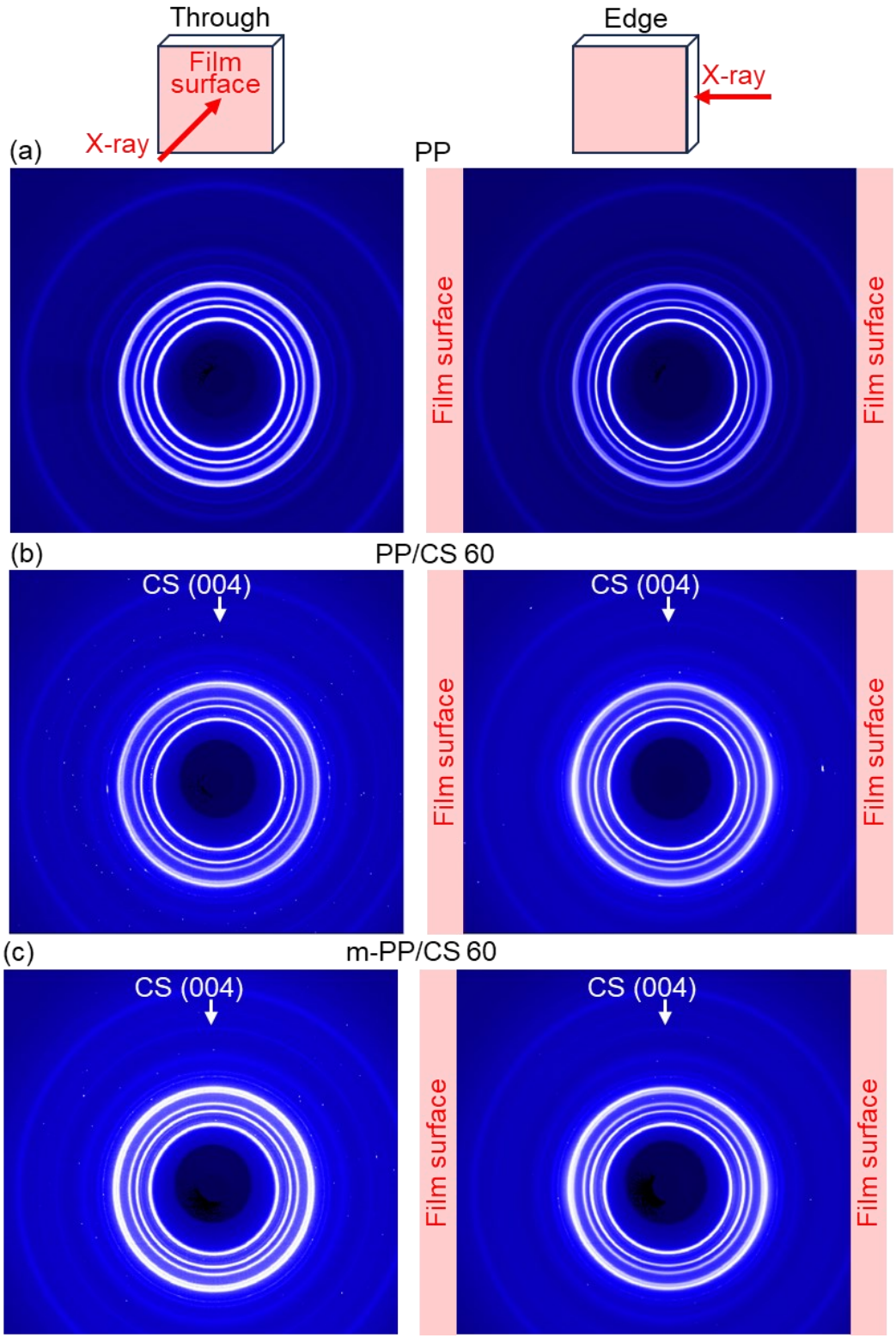

Fig. 3.10 X-ray diffraction photographs of (a) slow-cooling PP film, (b) PP/CS 60, and (c) m-PP/CS 60 composites with synchrotron radiation irradiated from through and edge directions.

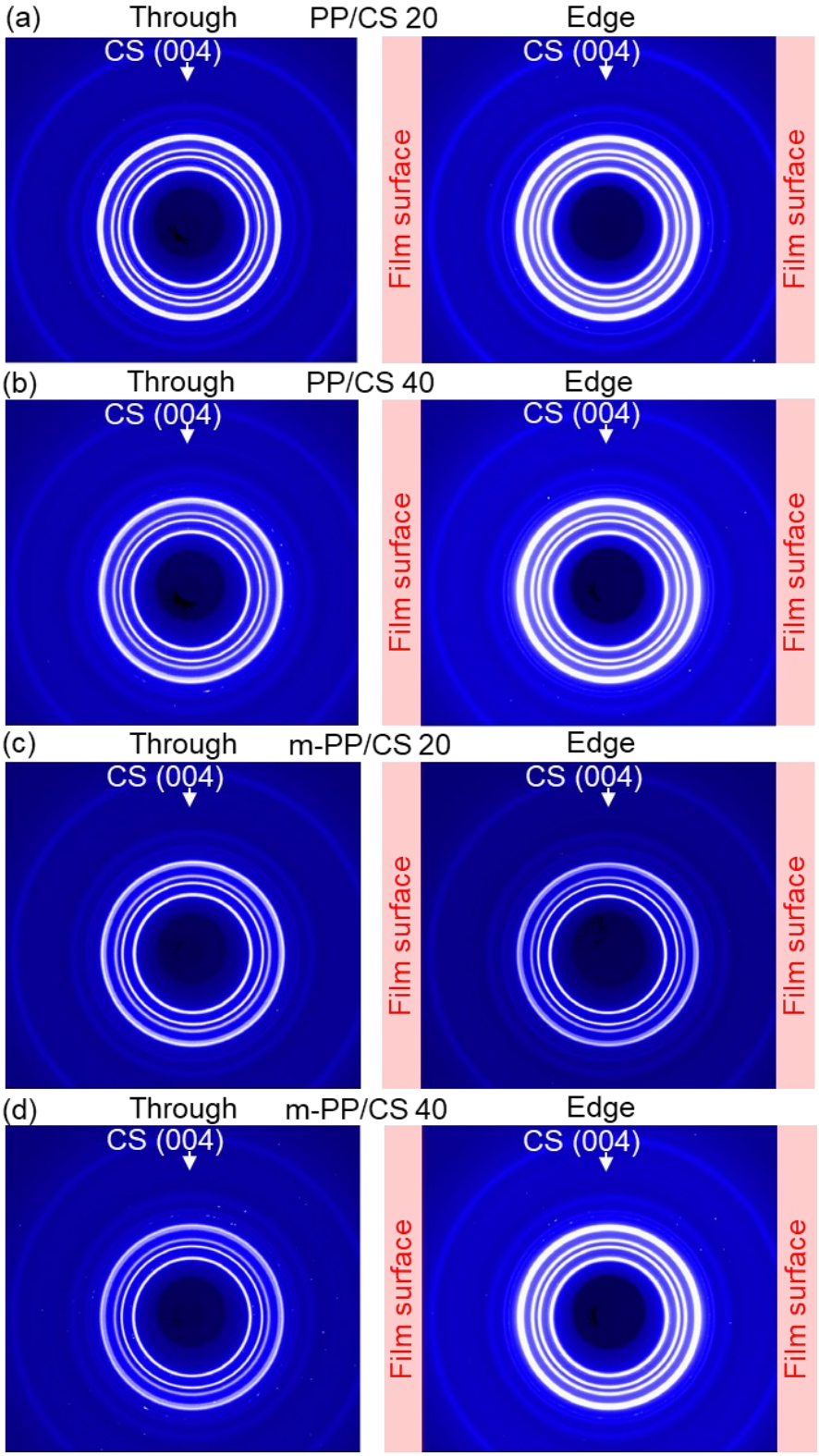

Fig. 3.11 X-ray diffraction photographs of (a) PP/CS 20, (b) PP/CS 40, (c) m-PP/CS 20, and (d) m-PP/CS 40 composites with synchrotron radiation irradiated from through and edge directions.

Figure 3.10 shows the X-ray diffraction photographs of (a) crystallized PP, (b) PP/CS 60, and (c) m-PP/CS 60 composites irradiated from through and edge directions. The crystallized PP sample was prepared as a reference by slowly cooling to r.t. as a reference. In Figure 3.10 (a), the Debye-Scherrer rings of the PP α-form were observed in both the through and edge direction photographs, suggesting that PP crystallites were oriented randomly.[37,38] In Figures 3.10 (b) and (c), the 004 reflection of the cellulose I_β-form of CS fillers was observed.[39] In the through-direction photographs of PP/CS 60 and m-PP/CS 60, the 004 reflection appeared as the Debye-Scherrer rings, whereas their 004 reflection intensities focused on the meridional direction in the edge-direction photographs. This indicated that the c-axis (chain direction) of cellulose I_β in CS was aligned in the parallel direction to the surface of the PP/CS 60 and m-PP/CS 60 composites by hot-pressing compression. According to the result of X-ray CT, the plate-like CS fillers were also oriented in the parallel direction to the composites' surface, suggesting the c-axis of cellulose was laid parallel to the surface of the CS filler and composites. Similar behaviors to PP/CS 60 and m-PP/CS 60 composites were observed in PP/CS 20, 40 and m-PP/CS 20, 40 composites as shown in Figure 3.11 (a), (b), (c), and (d). Table 3.5 shows the degree of orientation (π) of CS fillers in PP/CS and m-PP/CS composites with various CS contents. The π values were increased with the increase of CS contents. In the hot-pressing process of the composites, the plate-like CS fillers would contact each other and be packed in the in-plane direction because the large amounts of the CS fillers were loaded, as shown in Figure 3.12. This is the reason for the larger π values. Besides, PP/CS and m-PP/CS composites with the same fraction of CS fillers exhibited similar π values, indicating that the effects of m-PP addition on the orientation of CS fillers were negligible.

Table. 3.5 Degree of orientation (π) of CS fillers in PP/CS and m-PP/CS composites measured from the 004 reflection in edge-direction X-ray diffraction photographs.

Sample	π
PP/CS 20	0.53
PP/CS 40	0.58
PP/CS 60	0.70
m-PP/CS 20	0.48
m-PP/CS 40	0.59
m-PP/CS 60	0.71

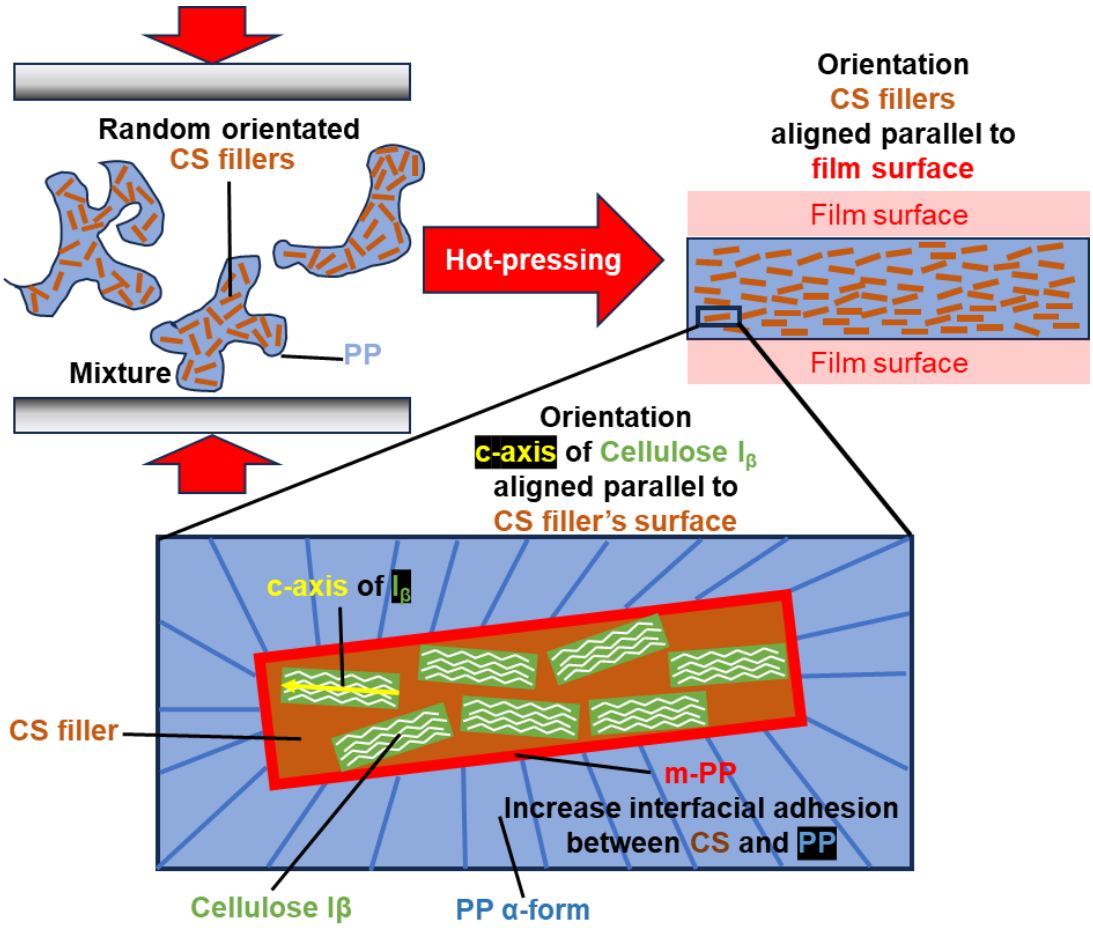

Fig. 3.12 Schematic model of the microstructure of m-PP/CS 60 composites with superior properties.

3.4 Conclusions

In this chapter, the author performed an investigation on the structure and mechanical properties of the composites with PP and CS. CS behaved as a bio-based polymer filler in the PP matrix, and m-PP was added as a compatibilizer. The composites with and without m-PP contained were prepared using melt-kneading and hot-pressing. The properties and morphology of composites were investigated. Young's modulus increased sharply in PP/CS composites without m-PP, when the tensile strength and elongation at break decreased. With the addition of amphipathic m-PP, the tensile strength and elongation at break of the m-PP/CS composites were improved compared to the PP/CS composites, which would be attributed to the enhanced interfacial interaction between the PP matrix and CS fillers. The balanced mechanical properties of m-PP/CS 60 composites with 60wt% CS loading were achieved, in which Young's modulus was increased by 162% compared with PP. According to the results of X-ray CT images and X-ray diffraction photographs, this great increase in Young's modulus would be attributed to the crystallization of the PP matrix and alignment of CS fillers parallel to the surface of composites. Since no significant difference between PP/CS and m-PP/CS composites' morphology was observed, the increase in tensile strength and elongation at break would be attributed to the enhanced interfacial interaction that resulted from the m-PP addition. Besides, the thermal expansion of the PP was suppressed by the CS fillers, and the linear thermal expansion coefficient (α) of the m-PP/CS 60 composites was decreased by 55% compared to PP, which resulted from the dimension stability of cellulose and hemicellulose in CS. The author believe that the orientation/alignment and interfacial interaction control of bio-based PP/CS composites investigated in this research will contribute to the further development of the future application of CS-filled composites.

3.5 Reference

[1] P. Lashermes, A.C. Andrade, H. Etienne, Genomics of Coffee One of the World's Largest Traded Commodities, in: Genomics of Tropical Crop Plants, Springer New York, New York, NY, 2008: pp. 203–226. https://doi.org/10.1007/978-0-387-71219-2_9.

[2] United States Department of Agriculture Foreign Agricultural Service, Coffee: World Markets and Trade (2024), (n.d.).

[3] L.F. Ballesteros, J.A. Teixeira, S.I. Mussatto, Chemical, Functional, and Structural Properties of Spent Coffee Grounds and Coffee Silverskin, Food Bioproc Tech 7 (2014) 3493–3503. https://doi.org/10.1007/s11947-014-1349-z.

[4] P. Esquivel, V.M. Jiménez, Functional properties of coffee and coffee by-products, Food Research International 46 (2012) 488–495. https://doi.org/10.1016/j.foodres.2011.05.028.

[5] L. Blinová, M. Sirotiak, A. Bartošová, M. Soldán, Review: Utilization of Waste From Coffee Production, Research Papers Faculty of Materials Science and Technology Slovak University of Technology 25 (2017) 91–101. https://doi.org/10.1515/rput-2017-0011.

[6] F. Behrouzian, A.M. Amini, A. Alghooneh, S.M.A. Razavi, Characterization of dietary fiber from coffee silverskin: An optimization study using response surface methodology, Bioactive Carbohydrates and Dietary Fibre 8 (2016) 58–64. https://doi.org/10.1016/j.bcdf.2016.11.004.

[7] Y. Narita, K. Inouye, Review on utilization and composition of coffee silverskin,

Food Research International 61 (2014) 16–22. https://doi.org/10.1016/j.foodres.2014.01.023.

[8] S. Bianchi, M. Vannini, L. Sisti, P. Marchese, N. Mallegni, Ó. Rodríguez, S. Kohnen, J. Tchoumtchoua, P. Cinelli, A. Celli, Valorization of coffee silverskin by cascade extraction of valuable biomolecules: preparation of eco-friendly composites as the ultimate step, Biofuels, Bioproducts and Biorefining 18 (2024) 524–542. https://doi.org/10.1002/bbb.2587.

[9] L. Sisti, G. Totaro, A. Rosato, N. Bozzi Cionci, D. Di Gioia, L. Barbieri, A. Saccani, Durability of biopolymeric composites formulated with fillers from a by-product of coffee roasting, Polym Compos 43 (2022) 1485–1493. https://doi.org/10.1002/pc.26468.

[10] A.K.A. Ghazvini, G. Ormondroyd, S. Curling, A. Saccani, L. Sisti, An investigation on the possible use of coffee silverskin in <scp>PLA</scp> / <scp>PBS</scp> composites, J Appl Polym Sci 139 (2022). https://doi.org/10.1002/app.52264.

[11] F. Sarasini, J. Tirillò, A. Zuorro, G. Maffei, R. Lavecchia, D. Puglia, F. Dominici, F. Luzi, T. Valente, L. Torre, Recycling coffee silverskin in sustainable composites based on a poly(butylene adipate-co-terephthalate)/poly(3-hydroxybutyrate-co-3-hydroxyvalerate) matrix, Ind Crops Prod 118 (2018) 311–320. https://doi.org/10.1016/j.indcrop.2018.03.070.

[12] A. Hejna, M. Barczewski, P. Kosmela, O. Mysiukiewicz, A. Kuzmin, Coffee Silverskin as a Multifunctional Waste Filler for High-Density Polyethylene Green

Composites, Journal of Composites Science 5 (2021) 44. https://doi.org/10.3390/jcs5020044.

[13] N. Zarrinbakhsh, T. Wang, A. Rodriguez-Uribe, M. Misra, A.K. Mohanty, Characterization of Wastes and Coproducts from the Coffee Industry for Composite Material Production, Bioresources 11 (2016). https://doi.org/10.15376/biores.11.3.7637-7653.

[14] F. Dominici, D. García García, V. Fombuena, F. Luzi, D. Puglia, L. Torre, R. Balart, Bio-Polyethylene-Based Composites Reinforced with Alkali and Palmitoyl Chloride-Treated Coffee Silverskin, Molecules 24 (2019) 3113. https://doi.org/10.3390/molecules24173113.

[15] D.R.H. Ochoa, J.A. Rojas-Vargas, Y. Costa, Characterization of NaOH-treated Colombian silverskin coffee fiber as a composite reinforcement, Bioresources 12 (2017) 8803–8812. https://doi.org/10.15376/biores.12.4.8803-8812.

[16] A. Taguet, P. Cassagnau, J.-M. Lopez-Cuesta, Structuration, selective dispersion and compatibilizing effect of (nano)fillers in polymer blends, Prog Polym Sci 39 (2014) 1526–1563. https://doi.org/10.1016/j.progpolymsci.2014.04.002.

[17] B.C. Trivedi, B.M. Culbertson, Maleic Anhydride, Springer US, Boston, MA, 1982. https://doi.org/10.1007/978-1-4757-0940-7.

[18] T.A. Bullions, R.A. Gillespie, J. Price-O'Brien, A.C. Loos, The effect of maleic anhydride modified polypropylene on the mechanical properties of feather fiber, kraft pulp, polypropylene composites, J Appl Polym Sci 92 (2004) 3771–3783. https://doi.org/10.1002/app.20369.

[19] K. Murayama, S. Suzuki, Y. Kojima, H. Kobori, H. Ito, S. Ogoe, M. Okamoto, The Effects of Different Types of Maleic Anhydride-Modified Polypropylene on the Physical and Mechanical Properties of Polypropylene-based Wood/Plastic Composites, Journal of Wood Chemistry and Technology 38 (2018) 224–232. https://doi.org/10.1080/02773813.2018.1432655.

[20] H. Yang, R. Yan, H. Chen, D.H. Lee, C. Zheng, Characteristics of hemicellulose, cellulose and lignin pyrolysis, Fuel 86 (2007) 1781–1788. https://doi.org/10.1016/j.fuel.2006.12.013.

[21] K.S. Kumar, S. Gairola, I. Singh, Waste Coffee Silverskin as a potential filler in sustainable composites: Mechanical, thermal, and microstructural analysis, Ind Crops Prod 210 (2024) 118088. https://doi.org/10.1016/j.indcrop.2024.118088.

[22] F. Yao, Q. Wu, Y. Lei, W. Guo, Y. Xu, Thermal decomposition kinetics of natural fibers: Activation energy with dynamic thermogravimetric analysis, Polym Degrad Stab 93 (2008) 90–98. https://doi.org/10.1016/j.polymdegradstab.2007.10.012.

[23] Y. Narita, K. Inouye, Review on utilization and composition of coffee silverskin, Food Research International 61 (2014) 16–22. https://doi.org/10.1016/j.foodres.2014.01.023.

[24] A.-I. Petaloti, D.S. Achilias, The Development of Sustainable Biocomposite Materials Based on Poly(lactic acid) and Silverskin, a Coffee Industry By-Product, for Food Packaging Applications, Sustainability 16 (2024) 5075. https://doi.org/10.3390/su16125075.

[25] Y. Shang, The melt memory effects in polymer crystallization, Journal of Polymer

Science 62 (2024) 2340–2354. https://doi.org/10.1002/pol.20230882.

[26] M. Zhang, B.-H. Guo, J. Xu, A Review on Polymer Crystallization Theories, Crystals (Basel) 7 (2016) 4. https://doi.org/10.3390/cryst7010004.

[27] A. Pawlak, Crystallization of Polymers with a Reduced Density of Entanglements, Crystals (Basel) 14 (2024) 385. https://doi.org/10.3390/cryst14040385.

[28] S. Gagliardi, V. Arrighi, R. Ferguson, M.T.F. Telling, Restricted dynamics in polymer-filler systems, Physica B Condens Matter 301 (2001) 110–114. https://doi.org/10.1016/S0921-4526(01)00520-8.

[29] P. Russo, V. Venezia, F. Tescione, J. Avossa, G. Luciani, B. Silvestri, A. Costantini, Improving Interaction at Polymer–Filler Interface: The Efficacy of Wrinkle Texture, Nanomaterials 10 (2020) 208. https://doi.org/10.3390/nano10020208.

[30] M. V. Ramiah, D.A.I. Goring, The thermal expansion of cellulose, hemicellulose, and lignin, Journal of Polymer Science Part C: Polymer Symposia 11 (1965) 27–48. https://doi.org/10.1002/polc.5070110105.

[31] T. Hirano, K. Mitsuzawa, S. Ishioka, K. Daicho, H. Soeta, M. Zhao, M. Takeda, Y. Takai, S. Fujisawa, T. Saito, Anisotropic Thermal Expansion of Transparent Cellulose Nanopapers, Front Chem 8 (2020). https://doi.org/10.3389/fchem.2020.00068.

[32] L. Li, W.H. de Jeu, Shear-Induced Smectic Ordering in the Melt of Isotactic Polypropylene, Phys Rev Lett 92 (2004) 075506. https://doi.org/10.1103/PhysRevLett.92.075506.

[33] S. Brückner, S. V. Meille, V. Petraccone, B. Pirozzi, Polymorphism in isotactic

polypropylene, Prog Polym Sci 16 (1991) 361–404. https://doi.org/10.1016/0079-6700(91)90023-E.

[34] M. Wada, R. Hori, U.-J. Kim, S. Sasaki, X-ray diffraction study on the thermal expansion behavior of cellulose Iβ and its high-temperature phase, Polym Degrad Stab 95 (2010) 1330–1334. https://doi.org/10.1016/j.polymdegradstab.2010.01.034.

[35] L. Segal, J.J. Creely, A.E. Martin, C.M. Conrad, An Empirical Method for Estimating the Degree of Crystallinity of Native Cellulose Using the X-Ray Diffractometer, Textile Research Journal 29 (1959) 786–794. https://doi.org/10.1177/004051755902901003.

[36] B. Lotz, A New ε Crystal Modification Found in Stereodefective Isotactic Polypropylene Samples, Macromolecules 47 (2014) 7612–7624. https://doi.org/10.1021/ma5009868.

[37] E.M. Benetti, V. Causin, C. Marega, A. Marigo, G. Ferrara, A. Ferraro, M. Consalvi, F. Fantinel, Morphological and structural characterization of polypropylene based nanocomposites, Polymer (Guildf) 46 (2005) 8275–8285. https://doi.org/10.1016/j.polymer.2005.06.056.

[38] A.J. Lovinger, J.O. Chua, C.C. Gryte, Studies on the α and β forms of isotactic polypropylene by crystallization in a temperature gradient, Journal of Polymer Science: Polymer Physics Edition 15 (1977) 641–656. https://doi.org/10.1002/pol.1977.180150405.

[39] X. Ju, M. Bowden, E.E. Brown, X. Zhang, An improved X-ray diffraction method

for cellulose crystallinity measurement, Carbohydr Polym 123 (2015) 476–481. https://doi.org/10.1016/j.carbpol.2014.12.071.

CONCLUSIONS

In this thesis, structure and mechanical properties of bio-based polymers and their composites were investigated

To prevent environmental damage caused by mass-produced plastic products, biodegradable bio-based polymers are expected to be used as next-generation disposable materials as alternative oil-based polymers. Bio-based polymers from biomass such as trees, grain, and grass are synthesized. Bio-based polymers are paid attention to materials as eco-friendly without exhaustion. In addition, biodegradable bio-based polymers could be permanently recyclable and will be a good way to conserve energy. To meet the growing demand for an application, combining the bio-based polymer with other materials to fabricate the composite is an effective approach. The glorious development of the bio-based polymer has been achieved. Among all kinds of bio-based polymers and their composites, polyamide 4 (PA4), poly(*L*-lactic acid)/hydroxyapatite (PLLA/HAp) composites, and isotactic polypropylene/coffee silverskin were adopted.

For using polymers, it is necessary to control the polymer properties such as mechanical, thermal properties or surface interface for the needs. Among polymer structure, crystalline regions are most important factor. These crystalline regions contribute to the polymer properties directly. Therefore, it is most important to investigate the exact crystal structure and properties. In this thesis, the crystal modulus was used for investigating the crystal properties. For example, crystal modulus in the direction parallel (E_l) and perpendicular (E_t) to the chain axis give information about skeletal conformation, deformation mechanism, maximum modulus and intermolecular interaction, anisotropies of polymers, respectively. Also, in order to exclude the thermal factor in the polymers, crystal modulus was measured at cryogenic temperature, and investigated the temperature

dependence of polymers from cryogenic temperature to high temperature.

In **Chapter 1**, crystal modulus of PA4 was investigated. Highly oriented PA4 fibers were prepared by dry-spinning and drawing. The crystal modulus E_l was measured by X-ray diffraction under loading tensile stress. The of E_l values as 67 GPa are obtained from 004 and 119 GPa from 0010 reflection, respectively. This difference was attributed to the decrease of crystallite size when the stress was applied to the fibers proved through Hosemann's method and Wallner's method with calculation of structure factor and Laue factor. When the applied stress increased from 0 to 270 MPa, the number of unit cells along the chain direction in a crystallite were declined from 7.5 to 5.8. It was revealed that lower E_l value of 004 reflection resulted from the apparently higher peak shifts with load than actual influenced by the Laue factor. When corrected this fact, the E_l of 0010 reflection was considered as the most reliable value of α-form PA4, 119 GPa. This value is lower than the E_l of PA610, PA66 and PA6 but higher than that of PA46 and PA12. The E_l of PA4 is significantly lower than the calculated values, which will be attributed to a 1.9% contraction of the PA4 chains from the fully extended planar zigzag conformation.

In **Chapter 2**, Synchrotron radiation X-ray diffraction facilitates the quantification of stress transferred to the fillers in the PLLA/HAp composites. The stress transferred to HAp fillers in PLLA/HAp composites under tensile test was evaluated *in situ* by X-ray diffraction measurement under tensile tests. The stress on fillers was several times larger than the applied stress during the elastic deformation stage. This indicates that the stress was concentrated on the incorporated HAp fillers, leading to mechanical reinforcement in the composite. The stress transfer efficiency in the composites was evaluated with the stress transfer coefficients χ. The χ value of the composites ranged from 2.4 to 3.9,

depending on the fillers size and filling ratios. The χ values were increased with the increase of HAp fillers' size and the reduction of the weight fraction of HAp. Furthermore, the interfacial states in the composites were investigated using stress transfer analyses. Variations in HAp filler size significantly impact the fracture behaviors at the composite interface, consequently altering the macroscopic mechanical properties of the composites. These behaviors were attributed to the effect of critical particle size. These results demonstrated that synchrotron X-ray diffraction is a powerful tool for monitoring the stress transfer phenomena as well as the interfacial states in composites under deformation.

In **Chapter 3**, In this chapter, CS was applied as a bio-based polymer filler for the PP matrix, and the effects of m-PP as a compatibilizer was also discussed. The m-PP/CS composites with m-PP contained were prepared using melt-kneading and hot-pressing. The properties and morphology of composites were investigated. Young's modulus was increased sharply in PP/CS composites without m-PP, when the tensile strength and elongation at break were decreased. With the addition of amphipathic m-PP, the decrease in tensile strength was improved. The balanced mechanical properties of m-PP/CS composites with CS loading of 60wt% were achieved, in which Young's modulus was increased by 170% compared with neat PP. This great increase in Young's modulus would be attributed to the crystallization of the PP matrix and orientation of CS fillers, according to the result of XRD and X-ray CT. The linear thermal expansion of the PP was suppressed by the CS fillers, and the linear thermal expansion coefficient (α) of the m-PP/CS 60 composites was decreased by 55% compared to neat PP, which resulted from the dimension stability of cellulose and hemicellulose in CS.

In summary, the relationship between structure and mechanical properties of bio-based polymer and their composites were described. Based on the information of this thesis, their development as practical materials could be expected.